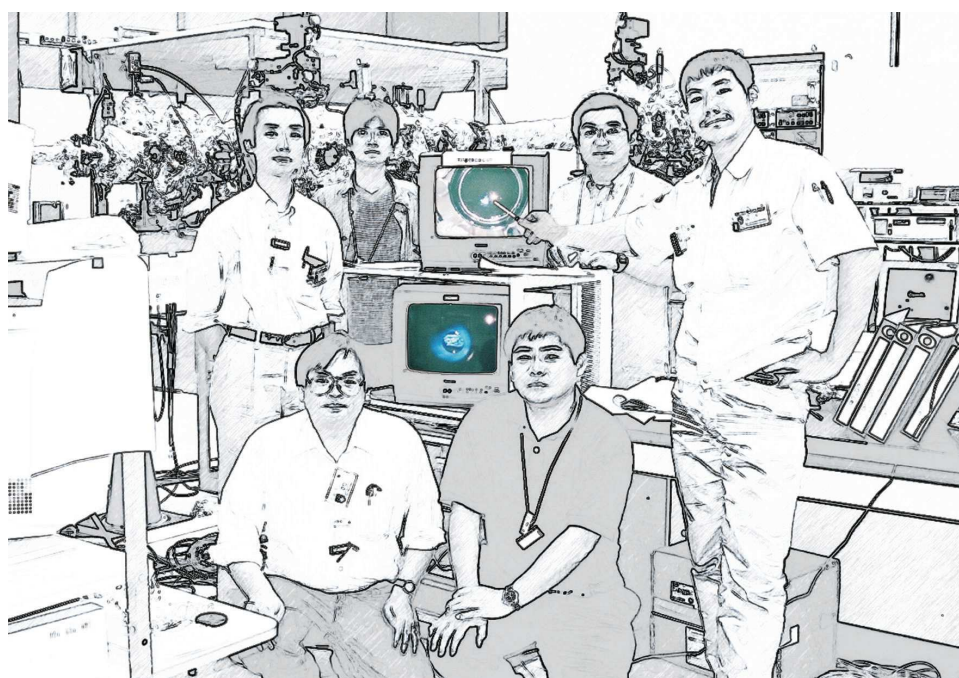


第2部 2014年度成果報告

Part II Activity Reports in 2014



The first light from NewSUBARU.

Continuous Generation of Laser Plasma X-Ray Using Solid Rare Gas Targets

Sho Amano
LASTI/ UH

Abstract

To generate continuously repetitive X-ray pulses from laser-produced plasmas, a translating substrate system with a cryostat that can continuously supply solid rare gas targets for 1~ 10 Hz laser pulses has been developed. The system successfully supplied solid Ar, Kr and Xe targets continuously, and stable output powers were achieved continuously from the plasma emissions. The X-ray powers were estimated to be 19 mW at 3.2 nm, 33 mW at 10.0 nm and 66 mW at 10.8 nm, with 10% bandwidths, from the Ar, Kr and Xe solid targets, respectively, with a laser power of 1 W.

Introduction

Laser plasma radiation from high density, high temperature plasma which is achieved by illuminating a target with high-peak-power laser irradiation, constitutes an attractive, high brightness point source for producing X-ray radiation. There have been many studies on application of laser plasma X-ray sources such as X-ray microscopes, EUV lithography and micro processing. To apply these studies in industry, a plasma source, which can generate continuous repetitive pulses, not a single shot, is required. Therefore, we have been studying it using a plasma target of solid rare gas [1-3]. The rare gas is considered to be an ideal deposition-free target because of an inert gas, and its chemically inactive debris will vaporize instantly, rather than be deposited on mirrors near the plasma. This is an advantage in a continuous operation. We had also decided to use a cryogenic solid target to provide higher conversion efficiency and higher brightness because of its higher solid density. Additionally, a smaller gas load for evacuation by the exhaust pump system was also expected in the solid state when compared with gas and liquid jets. To continuously supply the solid rare gas target, we originally developed a translating target system. Using this system, we succeeded in supplying Ar, Kr and Xe solid targets continuously and demonstrated continuous generation of laser plasma emission up to a repetition rate of 10Hz, produced by a commercial Nd:YAG Q-switched rod laser. In this paper, we report the developed target system and characteristics of the plasma X-ray emissions from the solid Ar, Kr and Xe targets supplied by it.

Experiments and Results

Figure 1 shows a side view of the developed target system [4]. A copper substrate was attached to the tip of a cryostat head with a He gas closed loop, thereby chilling the substrate surface. The lowest temperature at the substrate surface was measured to be 15 K. The target gas is blown on the surface and condensed to

form a solid layer. The substrate that was coated with the solid target layer translates up and down, in only one dimension, so that a fresh target surface is supplied continuously for every laser shot. The translation speed is tunable in the 0–12 mm/s range over a translation range of 60 mm. Apart from the area around the laser focus point, a container wall and two wipers surround the substrate surface. The wipers adjust the solid layer thickness to 500 nm and to assist with recovering of the laser craters on the target. We found 500 nm to be a sufficient thickness to prevent a 1 J laser shot damaging the substrate surface. In this experiment, Ar, Kr and Xe were used as target gases.

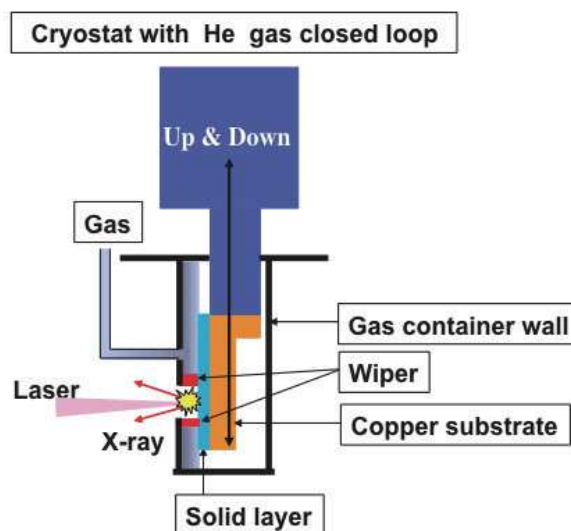


Fig.1. Illustration of the target system (side view).

Figure 2 shows the experimental set-up of the laser plasma source, composed of a target supply system and a driving laser. The target system was installed in

a vacuum chamber. A conventional Q-switched Nd:YAG rod laser (Spectra-Physics, PRO-230) was used as a driver and could deliver pulses at a wavelength of 1 μ m (1064 nm) with a pulse width of 10 ns. The maximum pulse energy and repetition rate are 1 J and 10 Hz, respectively. The pulses were expanded using a beam-expander, passed through the window and were focused perpendicularly on the target by a lens with a focal length of 500 mm, so that a plasma was produced and X-ray radiation was emitted. The generated X-ray pulses were monitored using an X-ray diode; XRD (SXUV-100 Mo/Si).

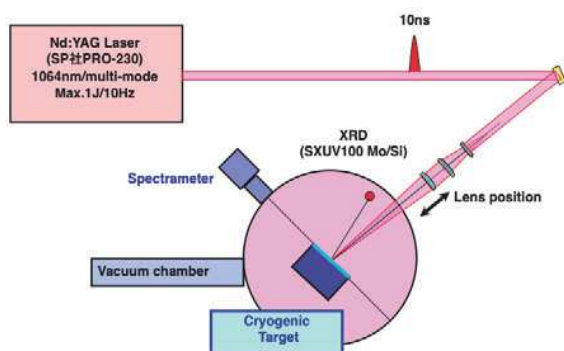


Fig.2. Experimental set-up (top view).

Results & Discussion

To operate the laser plasma source continuously to generate repetitive pulses, we studied optimum parameters of a translation speed and a gas flow rate for a laser frequency. Under the optimum conditions, the source was tested. For example, the laser pulses with energies of 1 J at 1 Hz, or 0.1 J at 10 Hz, were focused on the Ar target surface. The results of the continuously generated repetitive X-ray pulses monitored using an XRD, are shown in Fig. 3. This shows stable output power without any influence from the turning of the target up and down, even for round trips of 9–10 times in both the 1 Hz and 10 Hz cases. This indicates that a freshly recovered target surface was supplied continuously for each laser shot, as designed; we therefore succeeded in the demonstration of the design rule. We also similarly achieved the generation of continuous repetitive X-ray pulses from the Kr and Xe targets, again corresponding to the design rule.

The observed spectral peaks for the Ar, Kr and Xe targets are at 3.2, 10.0 and 10.8 nm [5]. When the targets were irradiated with 1 J energy pulses at 1 Hz, the spatially integrated average powers with the 10% bandwidth were roughly estimated to be 19 mW at 3.2 nm, 33 mW at 10.0 nm and 66 mW at 10.8 nm, for the Ar, Kr and Xe solid targets, respectively.

The laser plasma X-ray source emitting continuously will be useful for numerous applications, including soft X-ray microscopy, microprocessing, and surface modification. Especially, the solid Ar

target emits the soft X-ray in “water window” between 2.3 nm and 4.4 nm used for microscopy applications, and we are now characterizing the emission in “water window” range.

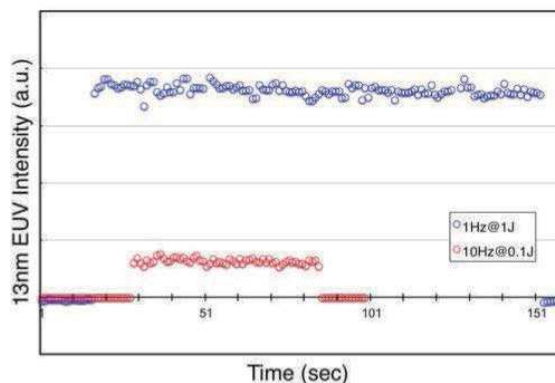


Fig.3. Soft X-ray intensity from the Ar target.

Acknowledgments

This work was supported by JSPS KAKENHI (Grant No. 23654204 & 26390113) and Hyogo Science and Technology Association (Grant No.26049).

References

- [1] S. Amano, *Recent Advances in Nanofabrication techniques and Applications* (InTech, Croatia, 2011), Chap. 18.
- [2] S. Amano et al., *Appl. Phys. B* **101**, 213 (2010).
- [3] S. Amano et al., *Appl. Phys. B* **108**, 743 (2012).
- [4] S. Amano, *Rev. Sci. Instrum.* **85**, 063104 (2014).
- [5] A. Shimoura et al., *Rev. Laser Eng.* **27**, 787(1999).

Improvement of BL05A Performance

T. Hasegawa^{1,4}, S. Fukushima^{2,4}, T. Kotaka³ and K. Kanda⁴

1 Synchrotron Analysis L.L.C., 3-2-24 Wadamia-dori, Hyogo-ku, Kobe-shi, Hyogo 652-0863 Japan

2 National Institute for Materials Science, 1-2-1 Sengen, Tsukuba-shi, Ibaraki 305-0047 Japan

3 New SUBARU, 1-1-2, Koto, Kamigori-cho, Ako-gun, Hyogo 678-1205 Japan

4 LASTI, University of Hyogo, 3-1-2 Koto Kamigori-cho, Ako-gun, Hyogo 678-1205 Japan

Abstract

The performance of BL05A has been improved for X-ray absorption fine structure (XAFS) measurements in the soft X-ray region to satisfy user's demands. A newly developed XAFS measurement system under atmospheric pressure was applied to obtain sulfur *K*-edge XANES spectra of solution and powder of sodium thiosulfate. In addition, the photon intensity in the magnesium *K* absorption edge region has been improved by replacing the beryllium filter (45 μm thickness) with existing one (25 μm thickness).

Introduction

BL05 is constructed on the basis of strong demand of industrial users for X-ray absorption fine structure (XAFS) spectroscopy. This beamline consists of two branch lines, one is a double crystal monochromator (DCM) beamline (BL05A) for the use in the higher-energy region (1300-4000 eV) and the other is a varied line spacing plane grating (VLSPG) monochromator beamline (BL05B) for the use in the lower-energy region (50-1300 eV) [1, 2]. These branches can be operated simultaneously. BL05 is managed and maintained by the Synchrotron Analysis L.L.C. (SALLC), which is composed of the industrial companies, in cooperation with the staffs of the Laboratory of Advanced Science and Technology for Industry in University of Hyogo. We planned for improvement of the performance in BL05A to corresponding to the user's demands. In this paper, we describe two improvements in XAFS measurements in the soft X-ray region, development for atmospheric pressure measurement system and beryllium filter.

1. Development for atmospheric pressure measurement system

A liquid sample and a wet sample couldn't be measured so far at BL05, because samples must be introduced into the high-vacuum chamber. So we equipped a sample chamber for atmospheric pressure measurement, which can be filled with He gas. A beryllium window (45 μm thickness) brazed high-vacuum gate valve was used to separate the atmospheric pressure in sample chamber and a high vacuum of beamline. Additionally, we succeeded in measurement of liquid samples in the atmospheric pressure by having developed a liquid cell. In Fig.1, the measured sulfur *K*-edge XANES spectra of 0.5M solution and powder of sodium thiosulfate are shown. S *K*-edge XANES spectra were collected

with a DCM, with 0.2 eV intervals and 1 seconds for each data point. The DCM used Ge (111) monochromator crystals. The liquid sample was mounted to the holder, which were sealed with a polyethylene sheet. In the liquid sample, the peaks caused by two different sulfur species were observed, which were existed in the powder sample.

2. Improvement of a beryllium filter

In BL05A, beryllium filter is installed to separate the ultra-high vacuum in the front-end from the high vacuum in the beamline, which located in the reflected beam after the M0 mirror. To improve the transmission factor of X-rays at the low energy, 1300 eV region (magnesium *K* absorption edge), a new beryllium filter was designed as thin as possible than previous one (45

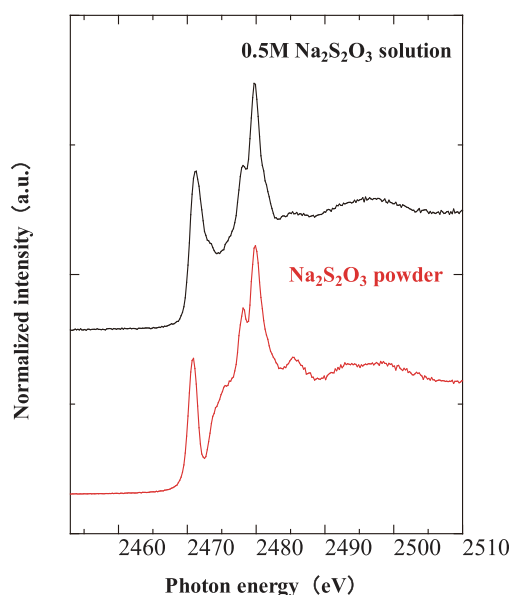


Fig.1 S *K*-edge XANES spectra of sodium thiosulfate (solution and powder).

μm thickness). We succeeded to make the filter with 25 μm thickness by supporting with multiple struts which were functioning as a reinforcing material (Fig.2). In Fig.3, the measured magnesium *K*-edge XANES spectra of several magnesium compounds using the new filter are shown. High-quality XANES spectra at the magnesium *K*-edge region were obtained due to improvement of the photon intensity.

Acknowledgement

The authors thank Dr. Tetsuro Mochizuki, fellow of TOYAMA Co., Ltd. for his support of design and fabrication of beryllium filter.

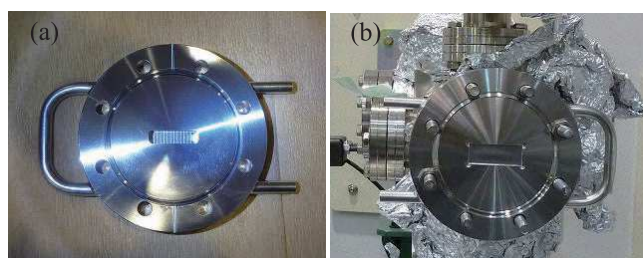


Fig.2 A new beryllium filter, (a) ultra-high vacuum side and (b) high vacuum side.

Reference

- [1] T. Hasegawa *et al.*, *Advances in X-ray Chem. Anal. Jpn.*, **41**, pp.99-106 (2010) [in Japanese].
- [2] K. Kanda *et al.*, *J. Phys.: Conf. Ser.*, **425**, 132005/1-4 (2013).

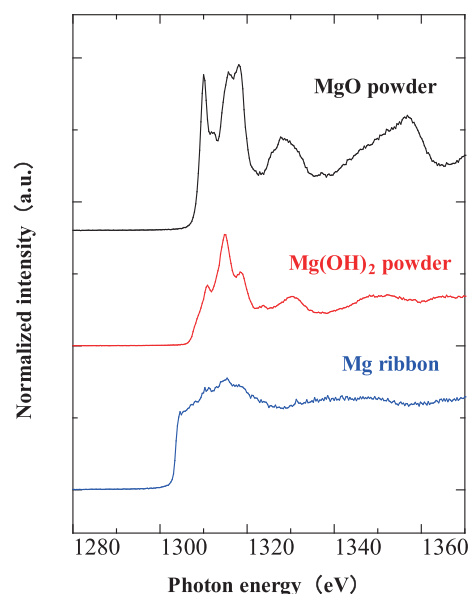


Fig.3 Mg *K*-edge XANES spectra of magnesium compounds.

Development of the simulation program, working on Excel, of C-K edge NEXAFS spectra of the DLC film for estimation of $sp^2/(sp^2+sp^3)$ ratio

H.Takamatsu¹, M.Endo¹, K.Kanda¹

¹LASTI, University of Hyogo, 3-1-2 Koto, Kamigori, Ako, Hyogo 678-1205 Japan

Abstract

Diamond-like carbon(DLC) films are used in various industrial fields. It's necessary to determine the characteristic of DLC film that we estimate $sp^2/(sp^2+sp^3)$ ratio of carbon atoms in the DLC film, which is obtained from the analysis of C-K edge NEXAFS spectra. But it needs exclusive analysis software and takes considerable time. We developed the simulation program that enables more accurate and effortless analysis than that in the past.

1. Introduction

The DLC film is well known for its various superior properties like high hardness, wear resistance, chemical inertness, and low friction coefficients [1]. It's used in various situations such as automobile parts, electronic components, medical instrument, the space industry, etc, and the development study for further performance enhancements is conducted by many researchers every day now.

The DLC film consists of sp^2 hybridized carbon and sp^3 hybridized carbon, and the hardness and density depend on the composition ratio of both. For example, the DLC film with a high content of sp^3 hybridized carbon shows high hardness and density. Therefore, it's very important to determine the characteristic of the DLC film that we clarify the content of sp^2 and sp^3 in the DLC film [2]. We can estimate the sp^2 ratio as $sp^2/(sp^2+sp^3)$ from spectra provided from C-K edge near-edge X-ray absorption fine structure (NEXAFS) [3]. This estimation has been essential the peak separation of spectra, and it usually has been fitted using date-analysis software. In this study, we developed the analysis simulation program of C-K edge NEXAFS spectra, working on Excel, and it can estimate $sp^2/(sp^2+sp^3)$ ratio with high accuracy.

2. C-K edge NEXAFS spectrum of the DLC film

The ratio of $sp^2/(sp^2+sp^3)$ which is important factor to determine the characteristic of the DLC films is estimated from the result of NEXAFS spectroscopy measured at magic angle (54.7°), as described above. The NEXAFS spectrum of the DLC film consists of three main pieces. Fig.1 shows a C-K edge NEXAFS spectrum of the general DLC film.

The first sharp peak, which appears around 285 eV, is due to π^* antibonding orbitals principally originating from C=C bonds, and this peak reflects sp^2 hybridized carbon. The next broad peak over

290 eV consists of the sites due to the C $1s \rightarrow \sigma^*$ resonance and the direct ionization.

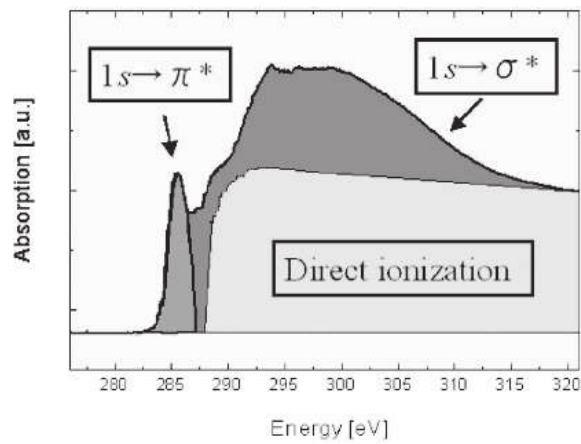


Fig.1. NEXAFS spectrum of DLC.

3. How to estimate $sp^2/(sp^2+sp^3)$ ratio

The $sp^2/(sp^2+sp^3)$ ratio is estimated from NEXAFS spectra of the highly ordered pyrolytic graphite (HOPG) as a standard sample and a target sample. At first I find the areas, which spectrum of HOPG, of C $1s \rightarrow \pi^*$ peak as $I_{\pi \text{ HOPG}}$ and the overall absorption intensity as $I_{\text{all HOPG}}$ to 330 eV and calculate the ratio of $I_{\pi \text{ HOPG}} / I_{\text{all HOPG}}$. In the same way, I find the areas, which spectrum of a target sample, of C $1s \rightarrow \pi^*$ peak as I_{π} and the overall absorption intensity as I_{all} and calculate the ratio of I_{π} / I_{all} . The $sp^2/(sp^2+sp^3)$ ratio is estimated in the next expression for the reason that the sp^2 composition in the HOPG is 100% [4].

$$\frac{sp^2}{sp^2+sp^3} = \frac{I_{\pi}/I_{\text{all}}}{I_{\pi \text{ HOPG}}/I_{\text{all HOPG}}} \quad (1)$$

4. Details of the simulation program

This simulation program has four main features:

error function (erf), working on Excel, automation and the programming language.

This program can use an erf to fit the edge jump at the ionization potential besides Gaussian functions for fittings of resonant peaks [3]. An example of the fitting for the HOPG is given in Fig. 2. The erf function enables to estimate peak intensity of σ^* area. Therefore, this simulation program is efficient to analyze of the DLC films with hetero elements which have new peaks at σ^* area.

The second feature is working on Excel which is the spreadsheet that Microsoft sells. Using Excel, we don't need to buy exclusive analysis software, and this program is reasonable because Excel is installed in many of computers.

The third of the four is automation. In this program, the peak fitting process is completed automatically using the solver function of Excel. In this way, we can reduce much time to spend it for a fitting; moreover, the result by the automatic fitting is more precise than result by manual fitting. In addition, the baseline revision and the normalization is also carried out automatically. Owing to this feature, our stress caused from the fitting will be lightened.

The Last is the programming language. This program is easy to add new function systems consciously because it's combined VBA (Visual Basic for Applications) and calculation on the cells.

comes easy.

References

- [1] A.Grill, Diamond Relat. Mater., 8 (1999) 428.
- [2] K. Kanda, J. Appl. Phys., 41, pp. 4295-4298 (2002)
- [3] C. Lenardi, J. Appl. Phys., 85, pp. 7159-7167 (1999)
- [4] A. Saikubo, Diamond Relat. Mater., 17 (2008) 1743

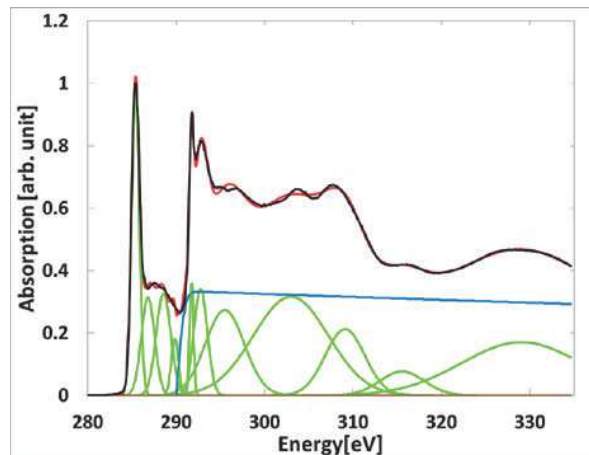


Fig.2. Fit of the sample HOPG. The black line is a measured result, the red line is the resulting fitted curve and the blue and green lines are the individual components of the deconvolution.

5. conclusion

Because this program can support a fitting of σ^* peak, detailed analysis is enabled conventionally about the DLC films with hetero elements and materials except DLC. Moreover, working on versatile Excel, we can expect that data analysis be-

Volume change of Si-containing hydrogenated DLC films by the soft X-ray irradiation

Shotaro TANAKA, Ryo IMAI, Makoto OKADA, Shinji MATSUI and Kazuhiro KANDA
LASTI, University of Hyogo, 3-1-2 Koto, Kamigori, Ako, Hyogo 678-1205 Japan

Abstract

The volume change of Si-containing Diamond-like carbon (Si-DLC) films by the exposure to synchrotron radiation (SR) in the soft X-ray region was studied with Stylus profiler. We found that volume of Si-DLC films were changed, while component elements were not change. Dose dependence of volume change is similar to none doped hydrogenated DLC (H-DLC) films. It was considered Si-DLC films were changed by that of the same mechanism of H-DLC films by the irradiation of the soft X-ray.

Introduction

Diamond-like carbon (DLC) films have various useful properties such as high hardness, a low friction coefficient, high abrasion quality, a gas barrier, chemical inertness and surface lubrication. Because of these characteristics, DLC films were utilized as coating materials on automobile parts, hard disks, artificial blood vessels, edge tools and food containers. In addition, DLC films are expected to be used in outer space as a lubrication substitution for oil, which cannot be used in space because it disappears in vacuums [1, 2].

It has been reported that H-DLC films were caused desorption of hydrogen due to soft X-ray exposure [3]. The several properties of DLC films doped hetero elements such as Si, Ti and W were improved. We found out that Si doped DLC films can be suppressed desorption of hydrogen. But $sp^2/(sp^2+sp^3)$ ratio of C atom that was measured by near edge X-ray absorption fine structure (NEXAFS) spectra was increased. Clarification of the effect of soft X-ray exposure on DLC films is important to ensure that DLC films can be used in outer space safely.

In this study, we investigated bulk properties of Si-DLC films by soft X-ray exposure. Specifically the steps between irradiation parts to unirradiation parts were measured with Stylus profiler, and their volume change was estimated by that steps.

Experiments

200-nm-thick Si-DLC films were deposited on

Si wafers by using a plasma-enhanced CVD method. The hydrogen content of Si-DLC films was estimated to be ≈ 40 at.% and the silicon content of Si-DLC films was estimated to be ≈ 20 at.% by using the combination of Rutherford backscattering spectrometry (RBS) and elastic recoil detection analysis (ERDA) techniques.

The SR irradiation of the Si-DLC films was carried out at BL06 of the NewSUBARU synchrotron facility. The SR at the BL06 irradiation chamber had a continuous spectrum from IR to soft X-rays, lower than 1000 eV. This include 300 eV, which is the ionization energy of a carbon K shell. As a result, the K shell electrons of the C atoms could be excited by SR at BL06. During this experiment, the electron energy of NewSUBARU storage ring was 1.5 GeV. The BL06 sample stage was room temperature and the pressure in the chamber was the order of 10^{-5} Pa. An SR dose [mA·h] was derived from the product of the ring current [mA] and exposure time [h]. When sample was irradiated, Au mesh was put on Si-DLC films. This mesh could be separated irradiation zone and unirradiation zone on one Si-DLC film.

The steps between irradiation part and unirradiation part on Si-DLC films by soft X-ray exposure were measured by Stylus profiler (Dektak-6M). The vertical resolution was 1 nm. When step was measured, scanning distance was

400 μm and scanning speed was 20 point/sec. The step was measured 5 places per 1 sample.

Result and discussion

Figure 1 shows surface of Si-DLC after soft X-ray exposure. The dose was 3000 $\text{mA}\cdot\text{h}$. It shows the pattern following Au mesh. This result can be understood that the step was appeared due to changing of volume by the soft X-ray exposure.

Figure 2 shows dependence of soft X-ray irradiation of volume change. The dose range of 0-200 $\text{mA}\cdot\text{h}$, step cannot be measured because volume change was smaller than 20 nm, which was resolution limit of Stylus profiler, but the step became ≈ 25 nm at 200 $\text{mA}\cdot\text{h}$. This is considered the step was drastically increase in the dose range of 0-200 $\text{mA}\cdot\text{h}$. Above 200 $\text{mA}\cdot\text{h}$, the step was slowly increase and consequently became ≈ 70 nm. Above ≈ 2000 $\text{mA}\cdot\text{h}$, the step remained approximately constant at ≈ 70 nm. In other words, the volume was decreases one-third by soft X-ray exposure.

This dose dependence is similar to that of none doped H-DLC films. This means that volume decreasing of Si-DLC films and H-DLC films is caused by the same process. This mechanism can be explained that the C – H bond decouples and the C = C bond couples. As a result, the density of Si-DLC films increase and the volume decrease. The result of volume change conforms to the result of $sp^2/(sp^2+sp^3)$ ratio.

Conclusion

Soft X-ray irradiation effect on Si-containing Diamond-like carbon films was investigated by the measurement of the volume change using Stylus profiler. The step between irradiation zone and unirradiation zone was increasing by soft X-ray exposure. The range of 0-200 $\text{mA}\cdot\text{h}$, the step was drastically increased. This result is similar to that of none doped H-DLC films. The step was reached 70 nm at last. The volume of Si-DLC films were decreased to one-third.

Reference

- [1] C. Donnet *et al.*, Surf. Coat. Technol. 120 (1999)548.
- [2] C. Donnet *et al.*, Tribology of Diamond-like

Carbon, Springer, 2008.

- [3] R. Imai *et al.* Diamond. Relat. Matel. 44(2014)8-10.

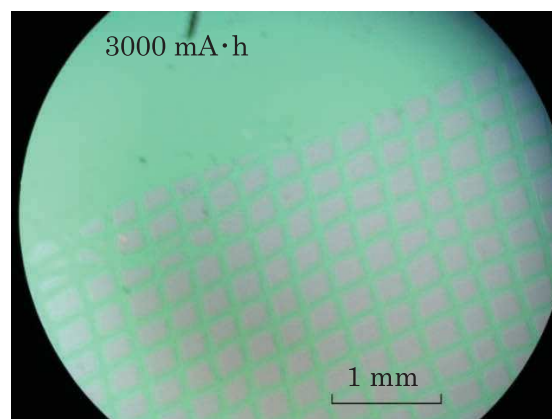


Figure 1. Surface of Si-DLC film after soft X-ray exposure. Used optical microscope.

The dose was 3000 $\text{mA}\cdot\text{h}$

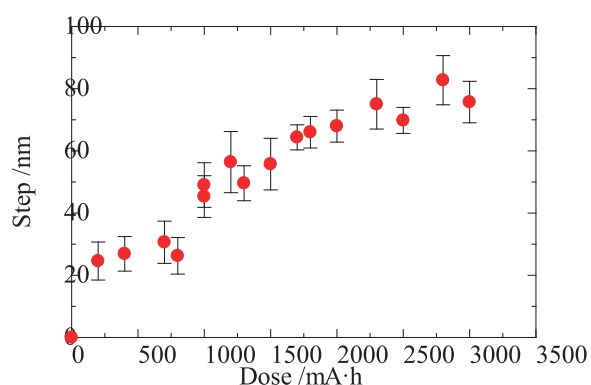


Figure 2. Dependence of soft X-ray irradiation of volume change.

Refractive-index modifications in Silica-Based Films by Undulator Radiation

K. Moriwaki, G. Kimura, Graduate School of Eng., Kobe Univ.,
K. Kanda, and S. Matsui, LASTI/Univ. Hyogo

Abstract

Undulator radiation (UR) by the NewSUBARU (BL7A) is used for silica-based films modifications as applications of optical devices like waveguides. The modification parts are mainly separated in two layers of the shallow and strong one and the relatively deep and moderate one. The thin layers with less than 5 nm thickness from the surface show strong reduction and high refractive index changes on the order of 10^{-2} depending on the UR energy. Relatively deep refractive-index-change is on the order of 10^{-3} , and is characterized by optical absorption measurements which is showing some kinds of defects as causes of the index changes. Defects are also found in the samples irradiated by UR with multilayer filter (a peak energy of 80 eV), although the surface reduction layer is not found in the samples.

Introduction

Synchrotron radiation (SR) and undulator radiation (UR) are used for radiation-induced refractive index changes in silica-based glass for optical devices^{1,2)} like optical waveguides. It is useful to induce large refractive-index changes more effectively using SR or UR without a spectrometer in the future. UR would be a very useful tool for the materials modifications, because it can select a useful wavelength, having very high intensity. In this report, modification effects are investigated in silica-based glasses irradiated by UR.

Experiments and Results

Thermally grown SiO_2 films on Si substrates and fused quartz substrates were used for UR irradiation as shown in Fig.1. UR with the 1st peak energy ranging from 20 to 110 eV is used.

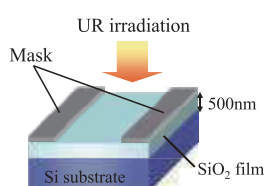


Fig.1 Schematic illustration for an UR-Irradiated sample.

Irradiated samples were characterized by XPS (X-ray Photoelectron Spectroscopy), optical absorption spectroscopy, and refractive index measurements.

Figure 2 shows refractive index changes for UR-irradiated SiO_2 films and their 20nm-etched ones with a reference line showing the initial refractive-index²⁾. XPS measurements revealed that the high refractive index samples by irradiating UR with less than 50 eV energy show

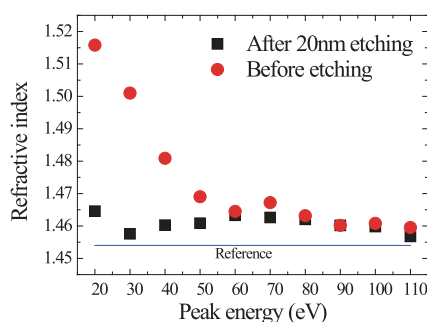


Fig.2 Refractive index changes for UR-irradiated samples and their 20nm-etched ones as a function of UR energy. The samples were thermally-grown SiO_2 films²⁾.

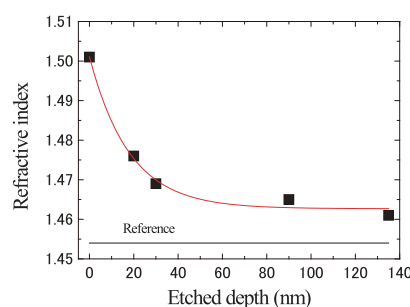


Fig.3 Refractive index change for UR-irradiated samples after step-by-step etching. The UR energy was 20eV and the sample was thermally-grown SiO_2 films.

strong reduction whose thickness was very shallow (around 5nm)²⁾. It is clear that the high index changes in Fig.2 is caused by the strong reduction layer, because the refractive index changes are decreased after the shallow etching. Figure 3 shows that the high refractive-index changes are in a layer of less than 30nm by measuring them after

step-by-step etchings. It is important that the refractive index remains high enough (10^{-3}) for an application to optical devices, after removing the high index layer. The surface reduction layer is a novel phenomenon and is very interesting, which would be useful in future applications. For an application in the near future, however, it is more important to investigate the relatively deep modification layer.

Figure 4 shows optical absorption results after UR irradiation with energies of 40, 50 and 60eV. Dotted lines of 210 and 260 nm in Fig.4 are those of defects which are E' center and NBOHC (non-bridging oxygen hole center), respectively. Figure 4 also shows increased absorbance as a whole compared to the reference of the initial value, originated from other various defects which might be a cause of the refractive index changes.

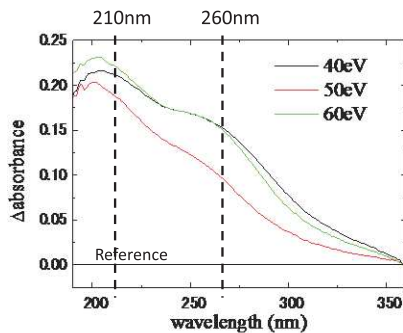


Fig.4 Optical absorbance spectra for samples after UR irradiation with energy of 40, 50 and 60eV. The samples were fused quartz substrates.

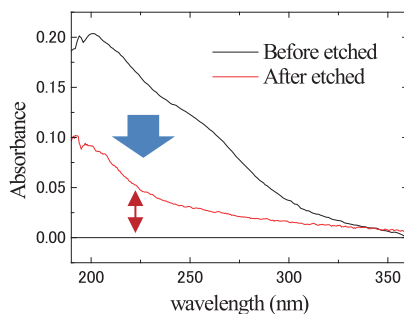


Fig.5 Optical absorbance spectra for samples after UR irradiation with energy of 50eV before and after etching the surface layer. The sample was fused quartz substrates.

Figure 5 shows that the optical absorbance increase remains high after removal of the surface reduction layer. This corresponds to the refractive index measurement results (Fig.3) which show refractive index values remain high after removal of the surface layer. This suggests strongly that those kinds of defects are the cause of the refractive index

increases, although more detailed investigations are needed.

UR spectra contains several peaks of higher order ones as well as the first order one. It is desirable to suppress higher order peaks, maintaining high intensities by the first order peak. Preliminary results using UR using multilayer filter were obtained as shown in Fig.6 and Fig.7. Defects were found in the irradiated sample (Fig.6), but the surface reduction layer was not found (Fig.7). Further measurements are also needed for this US irradiations.

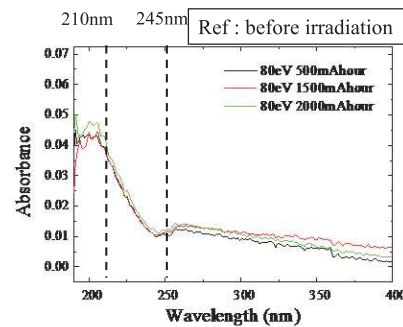


Fig.6 Optical absorbance spectra for samples after UR irradiation with a multilayer filter in fused quartz substrates.

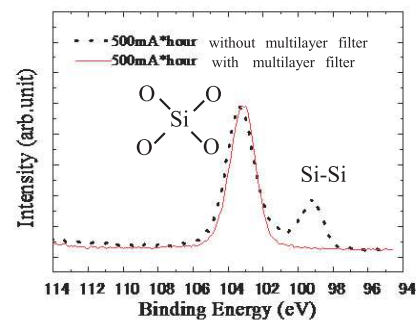


Fig.7 XPS spectra of Si 2p peaks for UR irradiated samples with an energy of 80eV with and without a multilayer filter. Two peaks are those of SiO₂ and Si-Si bond.

Conclusions

UR is found to be a useful modification tool for silica-based glass as optical material. Further investigations are needed to elucidate detailed mechanisms and the most effective conditions

References

- [1] K.Moriwaki et al., LASTI Annual Report vol.14 (2012).
- [2] K.Moriwaki et al., LASTI Annual Report vol.15 (2013).

New Designed Monochromator Controlled by Integrated Computing on BL07A

Masato Okui^{1,2}, Naoki Yato², Akinobu Watanabe², Junichi Saitoh², Naoko Sawada²,
Sei Fukushima^{1,3} and Kazuhiro Kanda¹

¹LASTI, University of Hyogo, ²Kohzu Precision Co., Ltd., ³NIMS

E-mail: okui@kohzu.co.jp

Abstract

The new monochromator installed on BL07A, MKZ-7NS, is a suitable monochromator to a mainly industrial use in medium-scale synchrotron radiation facilities like New SUBARU. This monochromator was designed as a common package as satisfied with general specification required for any synchrotron radiation facilities. The important feature of this is, even if omitting one of two slave axes that move the second crystal along optical axis by using optical surface widely of the second crystal, the beam offset can be fixed precisely. This design caused to reduce the convolution of mechanical errors. And it made size of machine of the monochromator compact so that the vacuum chamber was able to make smaller.

1. Introduction

The upgrade project of BL07A began on 2013. In this project, a new double crystal monochromator MKZ-7NS controlled by integrated computing was installed on this beamline. Now a day, industrial use in medium-scale synchrotron radiation facilities tends to increase so that easy maintenance shall be required to a monochromator used for both industrial and academic use. And, this should be considered for design and produce of next generation monochromator.

In the following, the authors will present about the feature of new monochromator MKZ-7NS installed on BL07A and discuss the flexibility to be able to install to other beamlines.

2. Design concept

Fig. 1 shows a photograph of MKZ-7NS.



Fig.1 Photograph of MKZ-7NS

Numbers of axes in vacuum were decreased than the previous monochromator controlled by integrated computing by contriving about the optical geometry. Y2 axis that is moved along the optical axis was also omitted. A slave axis synchronized with main axis for emitting to fixed exit position is only Z2 axis. Fig 2 shows the inside view of the vacuum chamber.



Fig. 2 Inside of MKZ-7NS vacuum chamber

X axis used for switching of monochromatic crystals is outside of the vacuum chamber. Numbers of axes inside of the vacuum chamber are decreased to 5. MKZ-7NS was designed in consideration of application to mainly industrial use in medium-scale synchrotron facilities like New SUNARU. The design concept is unitizing

each package of the needed specifications of double crystal monochromator used in medium-scale synchrotron.

Motor controllers, motor drivers and control software application are included in these packages. This monochromator has flexibility to be able to suit the other beamlines easily not only our beamline by changing controlled parameters on the software application.

Useable energy range in this beamline is from 50eV to 800eV [1]. Because of this, 3 multilayer mirrors are used as monochromatic devices in MKZ-7NS. Table 1 shows used multilayer mirrors in MKZ-7NS. However, as described above, this monochromator is designed to place high importance on flexibility.

Table 1 Multilayer mirrors of MKZ-7NS

Energy Range (eV)	Material	Spacing
50-95	Mo/Si	20nm
90-194	Mo/B ₄ C	11nm
190-800	Ni/C	5nm

This monochromator is also available in the other only beamlines using Si111 as monochromatic crystal, by changing some setting parameters. Offset between the incident beam and the exit beam is able to change any given value from 20mm to 30mm.

Many components of this monochromator are not positional stages designed for exclusive use, but they are the mass-produced standard positional stages using often in factory automation. Because of the above, this manufacturing cost would be decreased than the previous one. Furthermore, spare parts can be supplied soon by selecting the mass-produced standard positional stage as components. As the result, it can be expected that maintainability of monochromator shall be improved drastically. Outline drawing of MKZ-7NS is shown as Fig. 3

3. Ray trace

The ray trace when the beam offset is 20mm and the ray trace when the offset is 30mm are shown in Fig.4 and Fig.5, respectively.

The optical geometry using long the optical axis direction of the second monochromatic crystals was adopted in MKZ-7NS, as shown in FIGURE 3.

Because of this geometry, the slave axis controlled by integrated control to main axis is only Z2 axis. Z2 axis is used for adjusting to height of the second crystal. As the result, Y2 axis moving the second monochromatic crystal along the optical axis could be removed. This optical design will be available when monochromatic crystal along Y direction will be enough long.

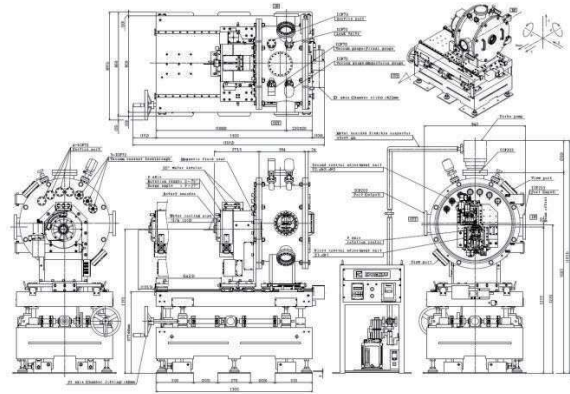


Fig.3 Outline drawing of MKZ-7NS

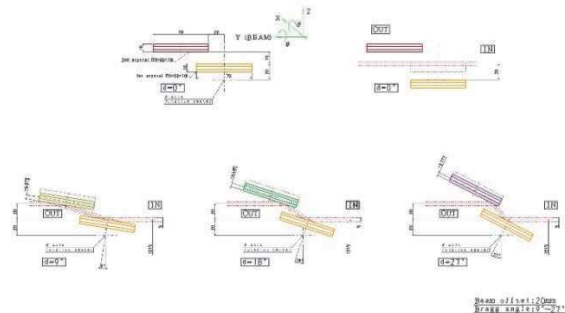


Fig.4 Ray trace when beam offset is 20mm

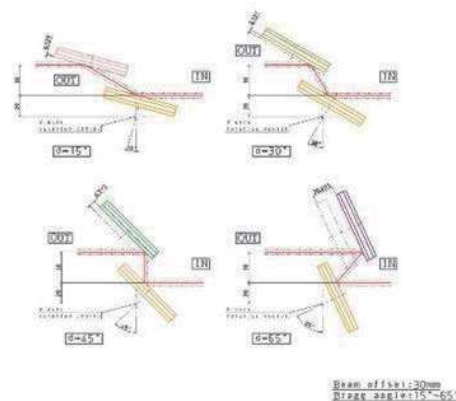


Fig.5 Ray trace when beam offset is 30mm

Z2 position of the slave axis synchronized to

main axis is the following equation, where D_{off} is the beam offset of monochromatic crystals and θ is Bragg angle.

$$Z2=(D_{\text{off}}\sin\theta/\sin2\theta)-15$$

Positional equation of the slave axis is simplified than the previous this type monochromator controlled integrated computing, because numbers of slave axis are decrease.

Parallelism of two monochromatic crystals is within 5arcsec in the range from 9deg to 28deg.

4. Discussion

It is suggested that trend of studies using synchrotron radiation would be changing from phase doing mainly fundamental study to phase of application of industrial use, gradually. The specifications needed as monochromator used as industrial use shall be different from specifications needed as monochromator used as fundamental sciences.

Monochromator used for industrial application would need usability that anyone can use easily and such easy maintainability that operation rate is enhanced.

Y2 axis inside of vacuum chamber could be omitted by shifting the incident point of the second monochromatic crystal from the center by using all length along the optical axis of the second crystal. As the result, the slave axis integrated by computing to main axis is only single Z2 axis. Since numbers of slave axes are single axis, computing to synchronize to main axis is simple. The authors consider that this simplification would contribute control integrated computing prospectively using electronic cam.

The numbers of axes inside the vacuum chamber was able to decrease because X axis was put outside of the vacuum chamber. In addition, by omitting Y2 axis inside the vacuum chamber it was smaller than the previous monochromator. This leads to increase degree of vacuum.

It was able to decrease manufacturing cost substantially by adopting mass-produced standard positional stage as each axes inside the vacuum chamber.

The useable range of Bragg angle can be from 9deg to 65deg when the offset of monochromatic crystals is 30mm, if the length of second monochromatic crystal is able to make long.

References

- [1] K.Kanda *et al.* Nucl.Inst. & Meth. In Phys. Res. A, **467-468**, 500-503 (2001)

Installation and Adjustment of Ultra-soft X-ray Fluorescence Spectrometer on BL07A

Sei Fukushima^{1,2}, Hiroki Takamatsu¹, Shotaro Tanaka¹, Kazuhiro Kanda¹

1: LASTI, Univ. Hyogo, 2: NIMS

Abstract

In order to meet a demand from the development of the advanced material technology, the study about ultra-soft X-ray fluorescence spectroscopy was intended to start. So, new designed equipment for this study was installed and has been adjusted at the end position of BL07A. The grating spectrometer was designed in order to have the high-efficiency by means of removing mechanical moving part. Now, the adjustment and testing of this equipment has been continued.

Introduction

Recent advance of modern materials requests more advanced manners of material analysis. For example, though the importance of ultra-light elements, such as Li, Be etc., has been increased in the field of energy materials or electronic materials, it is hard to analysis the chemical state of such elements, still now.

For analyzing the chemical state or the electronic structure of valence band, one of the most popular method is XAFS (X-ray absorption fine structure) measurement, and NewSUBARU has been already executed and obtained many remarkable results in the field of ultra-light elements, in BL09 for example [1]. One of the disadvantage points of XAFS measurement is the necessity of sweep the energy of incident X-ray. As known well, the efficiency of excitation for core level of such ultra-light element is very low, thus highly condensed monochromatized X-ray beam with high photon flux should be necessary for measurement.

In contrast, both the energy sweep and highly monochromatization for incident X-rays are not necessary for obtaining fluorescent X-rays (characteristic X-rays) from the samples. Thus, there is a practical meaning on examining the possibility of application of fluorescent X-rays.

Instead of the X-rays for excitation, electron beam is also available for obtaining characteristic X-rays, and this manner is already widely used as the EPMA (electron probe micro analyzer) analysis. This manner is also efficient for

the ultra-light elements, and, some of these members have already fabricated EPMA system for the chemical state analysis of ultra-light elements [2].

In this report, the status of the installation and the adjustment of new designed experimental equipment with ultra-soft X-ray fluorescence grating spectrometer on BL07A is presented.

Design and overview of equipment

The experimental equipment is consisted with two parts. One is the spectrometer for ultra-soft X-rays, and other is sample chamber with a mirror system for removing high energy X-rays.

The spectrometer on this equipment [2] was adopted the one which had been fabricated for the electron excitation system for the measurement of ultra-soft X-rays of about 33 to 470eV.

The features of this spectrometer are as follows; One of the important features is two types of flat field spherical VLS (varied line spacing) gratings designed with equal focal curves are the dispersion components. This grating spectrometer was designed as the energy resolution could be achieved more than $\sim 100 (E/\Delta E)$ with the incident slit width of $50\mu\text{m}$ in all of energy region. Using these gratings, the design of the compact spectrometer with high-resolution power could be realized.

The second feature is the poly-capillary set as the objective lens. Using this component, the wide uptake solid angle of the X-rays from the sample surface was realized so that the efficiency of

Table 1

The specification of the grating spectrometer.

grating	flat field spherical VLS (varied line spacing) type Radius of curvature : 6005mm brazing angle: $1.7 \pm 0.3^\circ$ the incidence angle : 87.19° the incidence focal length : 240mm the injection focal length : 300mm size: 52×32 mm	
	grating 1	grating 2
	the dispersion range : 33eV~140eV the number of the central fissure line: 300 l/m	the dispersion range : 106eV ~470eV the number of the central fissure line: 1090 l/m
poly-capillary	collective solid angle : 0.072Sr. input focal distance from enclosure front : 19.75mm enclosure end to output focal point : 215mm	
CCD camera	Roper SC-1300B back side illuminated type, the Peltier cooling system the saturation charge capacity : 1.8×10^5 e/pixel energy range: 1.3eV ~ 9keV number of pixel : 1340×1300 pixel size : $20\mu\text{m} \times 20\mu\text{m}$ detection area size : $26.8\text{mm} \times 26\text{mm}$	
slit	1mm ϕ , 50 $\mu\text{m} \times 2\text{mm}$, 10 $\mu\text{m} \times 2\text{mm}$, 2mm ϕ (full open)	

spectrometer was also increased. This poly-capillary was produced as the X-ray condenser for 1.5 keV X-rays, and the collection efficiency of this parts was estimated at about 200 times by the electron excitation system.

Another important feature is the backside-illumination type CCD camera as the detector. The CCD camera had no moving parts mechanically for detecting X-rays dispersed through the grating. Thus both slit and slit scan system are not required, and this is a significant advantage of the high-efficiency design.

The specifications of the main components of the spectrometer are listed in Table 1. In addition, a schematic illustration of this spectrometer is shown in Fig.1. The design and fabrication of this spectrometer was executed by JEOL ltd.



Fig.2

(a) The overview of the equipment before installation.

(b) The grating spectrometer after installation.

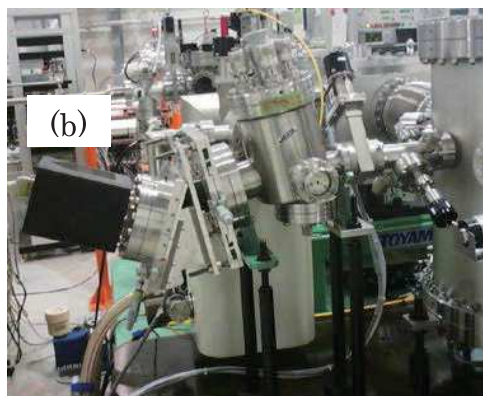
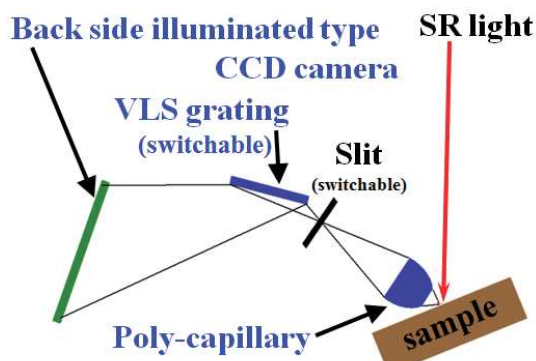


Fig.1

The schematic illustration of this spectrometer.



This experimental equipment was installed at the end of BL07A. The overview without spectrometer is shown in Fig.2(a). As already mentioned, this equipment has the sample chamber and a mirror system for removing high energy X-rays. This equipment was designed and fabricated by TOYAMA Co. Ltd.

The X-ray detector of the spectrometer mounted on this equipment is CCD camera, and this kind of detector has no function of energy analysis. Thus, CCD system cannot remove the higher order X-rays from the grating. Due to this point, the measured spectrum receives a lot of the overlapped peaks of higher order X-rays originated from the high energy X-rays. The surface of mirror was coated with metallic Cr of which cut-off energy was around 500 eV. And, it is expected that the overlapped peak of oxygen or fluorine will be weakened or removed using this mirror when one wish to measure the characteristic X-rays below 500 eV.

Present state and future

During 2014FY, the installation of this

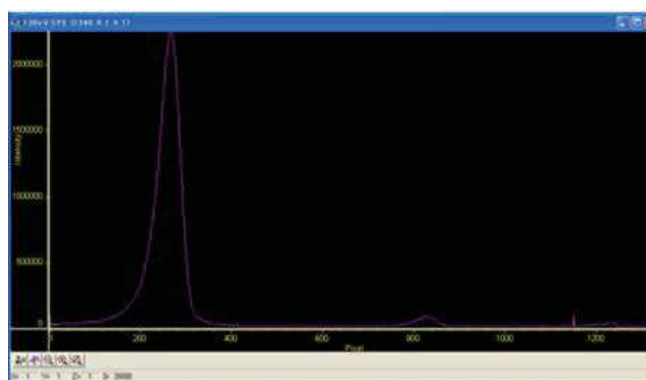
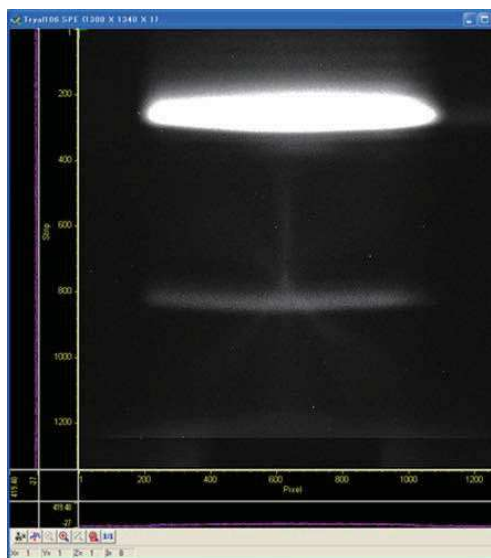


Fig.3 The example of measurement data for adjustment.
 (a) The dispersion image from grating on CCD camera.
 (b) The spectrum obtained from (a). The strong peak is scattered incident SR light (130eV), and the small peak at around the center is 2nd order light from the beamline monochromator. (b)

equipment was finished, and the adjustment of the grating spectrometer has been continued. One of the difficulties of the adjustment is : (a) as the stray light on visible region. In Fig.3, the example of the adjustment data is shown. Fig.3(a) is the dispersed X-rays image from the grating projected to the reception plane of the CCD camera. From this image, taking the sum of signal strengths of the each line of pixels perpendicular to the dispersion direction, the spectrum can be obtained as shown in Fig.3(b).

After the adjustment will finish, the examination of measurement condition of

the fluorescent X-rays will be started.

Acknowledgement

The authors thank gratefully Dr. Kazunori Tsukamoto and Dr. Toyohiko Tazawa, JEOL Ltd., for their so much cooperation, and also thank Mr. Hirotsugu Hara and Dr. Kazuki Akiyama, TOYAMA Co. Ltd., for design and fabrication of the experimental equipment.

References

- [1] M. Niibe et al. *J. Phys.: Conf. Series*, **425** 132008 (2013).
- [2] S. Fukushima et al. *Microchim. Acta* **161** pp.399-404 (2007).

Photon energy dependence of soft X-ray crystallization of $\text{Si}_{1-x}\text{Ge}_x$ films

Akira Heya¹, Fumito Kusakabe¹, Shota Hirano¹, Naoto Matsuo¹, Kazuhiro Kanda²

¹ University of Hyogo, 2167 Shosha, Himeji, Hyogo 671-2280, Japan
Phone: +81-79-267-4909 E-mail: heyaa@eng.u-hyogo.ac.jp

² LASTI, University of Hyogo, 3-1-2 Koto, Kamigori, Hyogo 678-1205, Japan

Abstract

Amorphous silicon germanium ($\text{a-Si}_{1-x}\text{Ge}_x$) films were crystallized by irradiation with soft X-rays of various photon energies. The crystallization upon soft X-ray irradiation is related to Ge concentration, photon energy, and photon-flux density. The Ge atom was the trigger for the crystallization of the SiGe film because the atomic migration of Ge atoms was enhanced by electron excitation during soft X-ray irradiation, compared with Si atoms. In the $\text{Si}_{0.5}\text{Ge}_{0.5}$ film, the ratio of peaks attributable to the crystal phases to those attributable to the amorphous phases of Si-Si, Si-Ge and Ge-Ge bonds changed with irradiated photon energy. This is explained by the relationship between the orbital energies of Si 2p and Ge 3d and the photon energy of irradiated soft X-rays, because the electron excitation probability was determined by this relationship.

Introduction

Low-temperature crystallization of amorphous semiconductor materials is important for realizing high-quality solar cells because the carrier lifetime of a crystallized semiconductor is longer than that of an amorphous semiconductor [1]. SiGe has a lower band gap and a higher optical absorption coefficient [2] than Si. In addition, the band gap and absorption coefficient of the SiGe film can be varied by adjusting the Ge concentration [3]. To realize high-efficiency solar cells, it is important to develop a method of low-temperature crystallization and to control the structural properties.

We proposed a low-temperature crystallization method that uses soft X-ray irradiation from the synchrotron radiation facility NewSUBARU [4, 5] and a laser plasma X-ray (LPX) source [6-9].

The present crystallization technique is expected to be applied to the fabrication of solar cells with high conversion efficiency [10]. However, the details of the relationship between the photon energy of soft X-rays and the crystallization of $\text{Si}_{1-x}\text{Ge}_x$ films are not clear. In this paper, we report detailed studies on the photon energy dependence of $\text{Si}_{1-x}\text{Ge}_x$ films crystallized by soft X-ray irradiation to understand the crystallization mechanism. In addition, the interaction between photons and electrons at the core level is discussed using the Fermi golden rule [11].

Experimental

Amorphous $\text{Si}_{1-x}\text{Ge}_x$ ($\text{a-Si}_{1-x}\text{Ge}_x$) films with various Ge concentrations ($X = 0.2, 0.4, 0.5, 0.6$,

and 0.8) were deposited on quartz substrates at room temperature by molecular beam deposition using Knudsen cells [12]. The base pressure was 9×10^{-7} Pa. The deposition rate and film thickness were 0.02 nm/s and 50 nm, respectively.

The irradiation of soft X-rays was carried out at BL07A of NewSUBARU [13]. The light source of BL07A was a 2.28 m undulator. The storage-ring energy was 1 GeV. The beam size measured with a fluorescent plate on the sample surface was $7.5 \times 7.5 \text{ mm}^2$. The photon energies were 50, 80, 100, 115, and 130 eV. These photon energies correspond to the core levels of Ge 3d (29.8 eV), Ge 3p (124.9 eV), and Si 2p (99.8 eV) [14]. The storage-ring currents were 75, 100, 125, 150, and 220 mA. The dose was fixed at 50 mA h.

The sample temperature during soft X-ray irradiation was monitored with a pyrometer using an emissivity of 0.8 [5]. The film properties were evaluated by Raman scattering measurement. Raman spectroscopy was carried out at room temperature using the 514.5 nm line from an Ar-ion laser. The ratio of the crystalline and amorphous phases (crystalline fraction) was evaluated using the peaks due to Si-Si, Si-Ge, and Ge-Ge bonds.

The percent of electron excitation probability at the irradiated photon energy was calculated by assuming an excitation lifetime of 1 ns at core levels of Ge 3d, Ge 3p, and Si 2p.

Results and discussion

The saturated sample temperatures, crystalline fractions, and crystallization areas of $\text{Si}_{1-x}\text{Ge}_x$ films irradiated under various conditions as a function of

Ge concentration are shown in Fig. 1. As the Ge concentration increased, the crystalline fraction and crystallization area increased. It is found that crystallization can occur under the conditions of high Ge concentration and high photon flux (high storage-ring current).

Plots of the crystalline fraction of soft-X-ray-irradiated $\text{Si}_{0.5}\text{Ge}_{0.5}$ films as a function of photon energy and the number of photons are shown in Figs. 2 and 3, respectively. The crystallization upon the soft X-ray irradiation occurs at photon densities between the low and high threshold values. At the photon-flux density of 1.3×10^{14} photons/s, the crystalline fraction of the SiGe film increases as the irradiated photon energy approaches the energy of the Ge 3d level. When the irradiated photon energy is close to the core level, the electron excitation from that energy level is enhanced, according to the Fermi golden rule.

The saturated sample temperatures of the $\text{Si}_{0.5}\text{Ge}_{0.5}$ film irradiated under various conditions

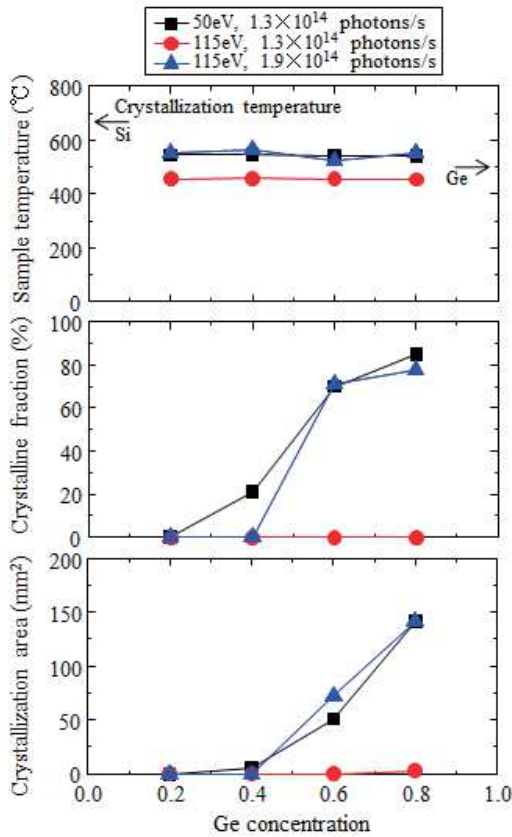


Fig. 1. Saturated sample temperatures, crystalline fractions, and crystallization areas of $\text{Si}_{1-x}\text{Ge}_x$ ($x = 0.2, 0.4, 0.6, 0.8$) films irradiated under various conditions as a function of Ge concentration. The crystallization temperatures of Si and Ge films for thermal annealing are indicated by arrows in the top figure.

are shown as a function of photon energy in Fig. 4. The saturated sample temperature depends on the irradiated photon energy. It seems that the temperature increased as the irradiated photon energy approached the energy of Ge 3d or Ge 3p. The crystallized samples are indicated by the solid plots obtained using data from the Raman spectra. It is known that the $\text{Si}_{0.5}\text{Ge}_{0.5}$ film is crystallized

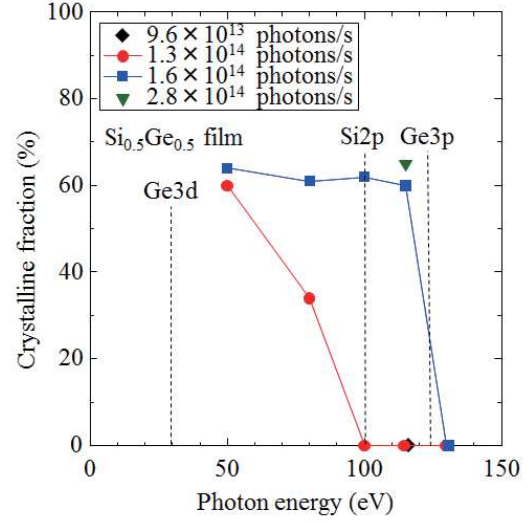


Fig. 2. Crystalline fraction of soft-X-ray-irradiated $\text{Si}_{0.5}\text{Ge}_{0.5}$ film as a function of photon energy. These crystalline fractions show the average crystalline fractions estimated from each peak attributable to Si-Si, Si-Ge, and Ge-Ge bonds.

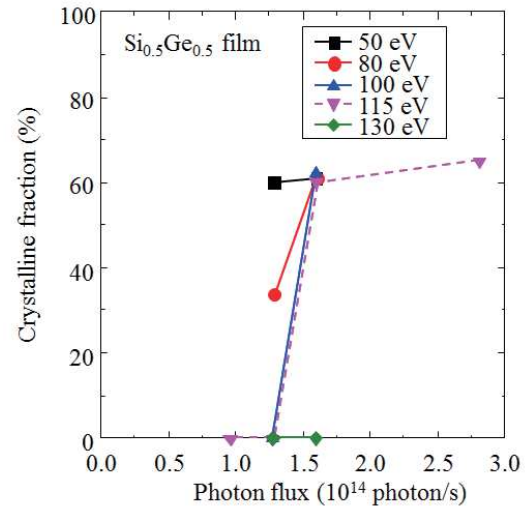


Fig. 3. Crystalline fraction of soft-X-ray-irradiated $\text{Si}_{0.5}\text{Ge}_{0.5}$ film as a function of photon flux. These crystalline fractions show the average crystalline fractions estimated from each peak attributable to Si-Si, Si-Ge, and Ge-Ge bonds.

above 620 °C [15]. It is shown that the critical temperature for crystallization is reduced to 465 °C by soft X-ray irradiation, similarly to a-Si and a-Ge films. Under the conditions of 130 eV and 125 mA, the sample temperature during soft X-ray irradiation was 525 °C and crystallization did not occur in spite of the high temperature, unlike in the case of 100 eV and 125 mA. It is found that the crystallization of the $\text{Si}_{0.5}\text{Ge}_{0.5}$ film depended on not only sample temperature but also photon energy.

To clarify the interaction between the irradiated photon energy and the electron at the core energy level, the Raman spectra of $\text{Si}_{0.5}\text{Ge}_{0.5}$ films irradiated at the storage-ring current of 125 mA and various photon energies were evaluated in detail. The crystalline fractions estimated from the peaks for each bond (Si-Si, Si-Ge, and Ge-Ge bonds) as a function of photon energy are shown in Fig. 5. The average crystalline fraction did not depend on photon energy. As the photon energy increased, the crystalline fraction estimated from the peak attributable to the Si-Si bond increased from 55 to 72%. On the other hand, the crystalline fractions for the peak attributable to the Ge-Ge bond increased as the photon energy approached the energy of the Ge 3d or Ge 3p orbital. In addition, the photon energy dependence of the crystalline fraction of the Si-Ge bond showed the same tendency as that of the Si-Si bond. It is reconstruction related to the Ge-Ge bond is achieved. The dependence of the crystalline fraction related to each bond on photon energy can be explained by the concept of the electron excitation of core orbital/atom movement (EEAM).

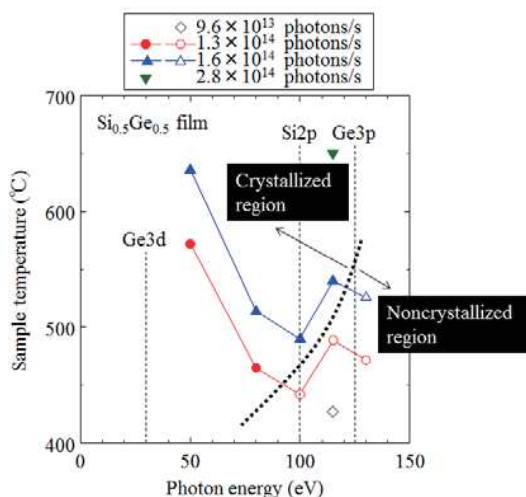


Fig. 4. Saturated sample temperatures and crystalline fractions of $\text{Si}_{0.5}\text{Ge}_{0.5}$ film irradiated under various conditions as a function of photon energy. The energy levels of Ge 3d, Ge 3p, and Si 2p are shown as dashed lines.

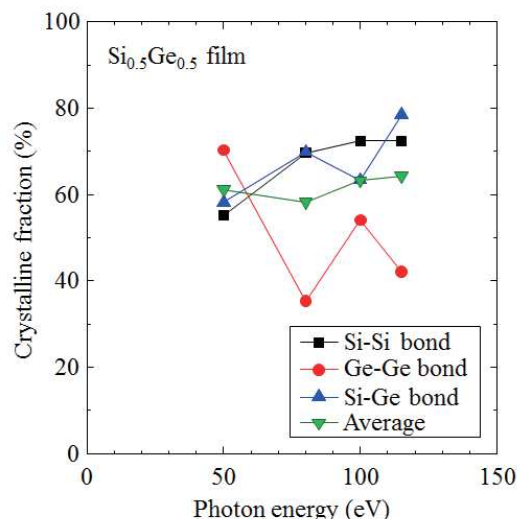


Fig. 5. Crystalline fractions estimated from peaks attributable to each bond (Si-Si, Si-Ge, and Ge-Ge bonds) of $\text{Si}_{0.5}\text{Ge}_{0.5}$ films as a function of photon energy. The storage-ring current was 125 mA.

considered that the crystallization upon soft X-ray irradiation is enhanced by electron excitation from each core energy. When the electrons in the Ge 3d or 3p orbital level are excited, the Ge atoms are preferentially ionized and moved. Therefore, the

Figure 6 shows the probabilities of electron excitation from Ge 3d, Ge 3p, and Si 2p at various photon energies. In this case, the lifetime of the excited state was assumed to be 1 ns. These probabilities were estimated using the Fermi golden rule and normalized by the value at 50 eV. The photon energy dependence of the probability of electron excitation from Si 2p was almost the same as the tendency of the crystalline fraction estimated from the peak of the Si-Si bond. On the other hand, the tendency of the crystalline fraction estimated from the peak of the Ge-Ge bond can be explain

ed by the photon energy dependence of the probability of electron excitation from Ge 3d or Ge 3p. It is considered that the crystallization upon soft X-ray irradiation is related to the electron excitation from the energy level of the core electron.

In the case of SiGe films, the electron excitation from Si or Ge occurs selectively because the excitation probabilities of Si and Ge differ at various photon energies. Therefore, each bond of Si-Si, Si-Ge, and Ge-Ge was preferentially reconstructed by the relationship between the photon energy of irradiated soft X-rays and the energy level of the Si or Ge core electron. The crystalline fractions estimated from each bond

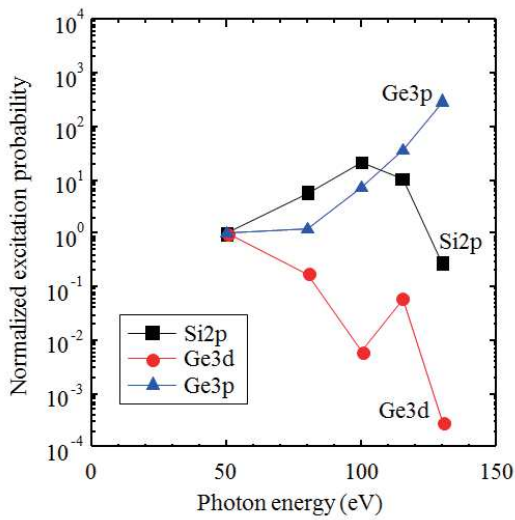


Fig. 6. Normalized probabilities of electron excitation from energy levels of Ge 3d, Ge 3p, and Si 2p at various photon energies. These probabilities were estimated using the Fermi golden rule and normalized by the value at 50 eV. The lifetime of the excited state was assumed to be 1 ns.

(Si-Si, Si-Ge, and Ge-Ge bonds) exhibit the photon energy dependence shown in Fig. 6. It is expected that fine tuning of the energy band gap in SiGe film for high-efficiency solar cells will be realized by controlling the photon energy. This is an advantage in the crystallization of SiGe films by soft X-ray irradiation.

Conclusions

The effects of the Ge concentration and irradiated photon energy on the crystallization of $\text{Si}_{1-x}\text{Ge}_x$ films by soft X-ray irradiation were investigated in order to produce high-efficiency solar cells. Crystallization by soft X-ray irradiation was related to the Ge concentration, photon energy, and photon-flux density, which means that the crystallization can be controlled by the irradiated photon energy. We believe that selective crystallization through soft X-ray irradiation at various photon energies can be applied to the fabrication of solar cells with the best optical absorption property, because the ratio of the amorphous phase to the polycrystalline phase can be controlled by the irradiated photon energy.

Acknowledgments

The authors are grateful to Associate Professor T. Sadoh and Professor M. Miyao of Kyushu University for SiGe film deposition. The authors would like to thank Professor S. Miyamoto and

Professor T. Mochizuki of LASTI, University of Hyogo for suggesting soft X-ray irradiation.

References

- [1] J. Wong, J. L. Huang, B. Eggleston, M. A. Green, O. Kunz, R. Evans, M. Keevers, and R. J. Egan, *J. Appl. Phys.* **107**, 123705 (2010).
- [2] Y. Hishikawa, N. Nakamura, S. Tsuda, S. Nakano, Y. Kishi, and Y. Kuwano, *Jpn. J. Appl. Phys.* **30**, 1008 (1991).
- [3] T. Matsui, M. Kondo, K. Ogita, T. Ozawa, and M. Isomura, *Appl. Phys. Lett.* **89**, 142115 (2006).
- [4] N. Matsuo, T. Mochizuki, S. Miyamoto, K. Kanda, N. Tanaka, and N. Kawamoto, *Dig. AM-LCD*, 2005, p. 293.
- [5] A. Heya, K. Kanda, K. Toko, T. Sadoh, S. Amano, N. Matsuo, S. Miyamoto, M. Miyao, and T. Mochizuki, *Thin Solid Films* **534**, 334 (2013).
- [6] N. Matsuo, K. Uejyukkoku, A. Heya, S. Amano, Y. Takanashi, S. Miyamoto, and T. Mochizuki, *Jpn. J. Appl. Phys.* **46**, 1061 (2007).
- [7] N. Matsuo and A. Heya, *Oyo Buturi* **82**, 390 (2013) [in Japanese].
- [8] A. Heya, Y. Takanashi, S. Amano, N. Matsuo, S. Miyamoto, and T. Mochizuki, *Jpn. J. Appl. Phys.* **48**, 050208 (2009).
- [9] N. Matsuo, N. Isoda, A. Heya, S. Amano, S. Miyamoto, T. Mochizuki, and N. Kawamoto, *Mater. Trans.* **51**, 1490 (2010).
- [10] A. Heya, N. Matsuo, M. Takahashi, K. Ito, and K. Kanda, *Appl. Phys. Express* **6**, 065501 (2013).
- [11] B. K. Ridley, *Quantum Processes in Semiconductors* (Oxford University Press, Oxford, U. K., 1999) 4th ed., 377.
- [12] H. Kanno, K. Toko, T. Sadoh and M. Miyao, *Appl. Phys. Lett.* **89**, 182120 (2006).
- [13] K. Kanda, Y. Haruyama, M. Fujisawa and S. Matsui, *Nucl. Instrum. Methods Phys. Res., Sect. A* **467-468**, 500 (2001).
- [14] M. Cardona and L. Ley ed., *Photoemission in Solid 1: General Principles* (Springer, Heidelberg, 1978).
- [15] E. P. Donovan, F. Spaepen, D. Turnbull, J. M. Poate, and D. C. Jacobson, *J. Appl. Phys.* **57**, 1795 (1985).
- [16] S. Hayashi, M. Fujii, T. Takanabe, and K. Yamamoto, *Jpn. J. Appl. Phys.* **27**, L1165 (1988).

Electronic structure of fluorinated self-assembled monolayer by photoelectron spectroscopy in the valence band region

Yuichi Haruyama and Shinji Matsui

Laboratory of Advanced Science and Technology for Industry, University of Hyogo

II

Abstract

The electronic structure of the fluorinated self-assembled monolayer (F-SAM) was investigated by using the photoelectron spectroscopy in the valence band region. The photon energy dependence of the photoelectron spectra in the valence band region of the F-SAM was measured from 50 to 420 eV and the orbital components of the photoelectron spectra were clarified. By measuring the photoelectron spectra in the valence band region of four types of F-SAMs with different chain lengths, we obtained the evolution of the electronic structures in the F-SAM. In addition, the energy level of the F-SAM molecule obtained by ab initio molecular orbital calculation in a previous study was compared with the photoelectron spectrum in the valence band region.

Introduction

Since the surfaces modified by the fluorinated self-assembled monolayer (F-SAM) have interesting properties such as hydrophobicity, antiadherence, and lubrication, the study of the F-SAM has attracted much attention for both fundamental research and industrial application. It is expected that the excellent hydrophobic property of the F-SAM has a potential application to automobile glass and house materials with self-cleaning effect. Recently, in the field of nanoimprint lithography, the F-SAM has been applied as an antisticking layer of a nanoimprint mold [1]. The surface properties of the F-SAM formed by various methods have been extensively investigated by many techniques so far. However, the electronic structure in the valence band region of the F-SAMs is not fully clarified experimentally. Therefore, we have performed photoelectron spectroscopy experiments in the valence band region of the F-SAMs.

Experiments and Results

Four types of F-SAMs were prepared from a precursor $[\text{CF}_3(\text{CF}_2)_n(\text{CH}_2)_2\text{Si}(\text{OCH}_3)_3]$; $n=0, 3, 5,$ and 7 as denoted FAS-3, 9, 13, and 17, respectively. Schematic diagrams of four types of F-SAMs are shown in Fig. 1. All photoelectron measurements were performed on a BL7B end station at the NewSUBARU facility. The synchrotron radiation with $h\nu$ between 50 and 420 eV was used. The total energy resolutions were 0.1–0.4 eV, depending on $h\nu$ of 50–420 eV. The photoelectron spectra were recorded at the emission angles of $\theta = 30$ and 90° to the sample surface.

Figure 2(a) shows the photoelectron spectra of the valence band region in FAS-13 as a function of $h\nu$. Six peaks at 26, 15, 12, 10, 8, and 4 eV were observed at $h\nu = 50$ eV. In

addition to these peaks, a peak at 34 eV was observed at more than $h\nu = 70$ eV. With increasing $h\nu$ from 70 to 420 eV, the intensities of three peaks at 34, 26, and 4 eV increased gradually. As for the intensity of the peak at 12 eV, it increased gradually at more than $h\nu = 180$ eV, although it decreased once at $h\nu = 130$ eV. At more than $h\nu = 240$ eV, the intensity of the peak at 12 eV became larger than that at 10 eV. In Fig. 2(b), a photoelectron spectrum in the Si substrate before preparing F-SAM is plotted for comparison. In the photoelectron spectrum of the Si substrate, five peaks were observed at 26, 15, 12, 8, and 4 eV. The shape of the photoelectron spectrum of the Si substrate was similar to that in the previous photoelectron studies of SiO_2 [2]. This indicates that the Si oxide was formed at the surface of the Si substrate. In the previous studies [2], two peaks at 26 and 4 eV were predominantly derived from the O 2s and Si 3p states, respectively, whereas three peaks at 15, 12, and 8 eV were predominantly derived from the O 2p + Si 3s + Si 3p states. Since the peak at 26 eV was observed in the photoelectron spectra of FAS-13, as shown in Fig. 2(a), it is considered that the photoelectrons from both FAS-13 and the Si substrate were detected in this study. Therefore, the five peaks at 26, 15, 12, 8, and 4

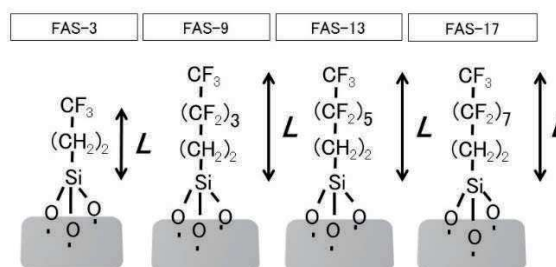


Fig. 1. Schematic diagrams of four types of F-SAMs with different chain lengths.

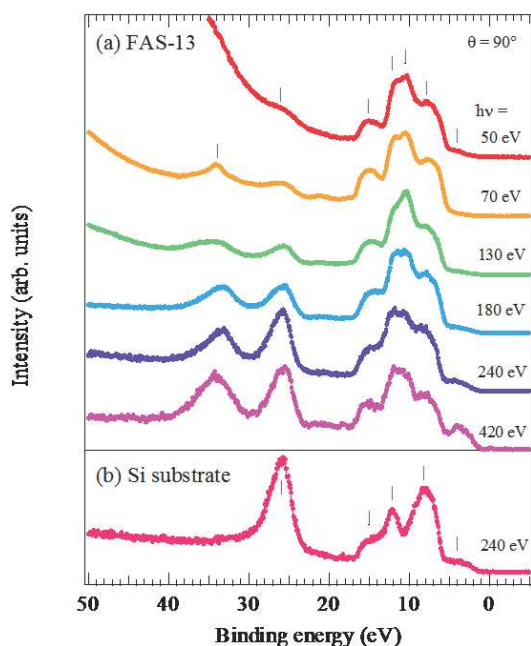


Fig. 2. (a) Photoelectron spectra in the valence band region of FAS-13 as a function of photon energy. (b) A photoelectron spectrum of the valence band region in the Si substrate.

eV observed in the photoelectron spectra of FAS-13 were predominantly assigned to the contribution from the Si substrate. According to Yeh and Lindau [3], the photoionization cross section of the F 2p state at $h\nu = 50$ eV to 300 eV is larger than that of the O 2s, O 2p, Si 3s, and Si 3p states. Therefore, the peak at 10 eV in the photoelectron spectra of FAS-13 is assigned to the F 2p state. With increasing $h\nu$, the photoionization cross section of the F 2s state increased gradually as compared with that of the F 2p state. At $h\nu = 420$ eV, the photoionization cross section of the F 2s state became larger than that of the F 2p state. These indicate that the peak at 34 eV is assigned to the F 2s state.

Figure 3 shows the photoelectron spectra of the valence band region in FAS-3, FAS-9, FAS-13, and FAS-17. Several new peaks were observed between 21 and 14 eV and two peaks at 8 and 7 eV were visible in all F-SAMs. At $h\nu = 50$ eV, the relative photoionization cross section of C 2p to F 2p states becomes larger than that at $h\nu = 130$ eV. Therefore, two peaks at 8 and 7 eV were probably assigned to the C 2p states in addition to the O 2p + Si 3s + Si 3p states. In FAS-3, a sharp peak at 18 eV was clearly observed in addition to the peak at 15 eV, and three small peaks at 21, 17, and 14 eV were visible. In FAS-9, three small peaks at 21, 18, and 15 eV were observed in addition to a sharp peak at 16 eV. With increasing the chain length from FAS-9 to FAS-13 and FAS-17, these

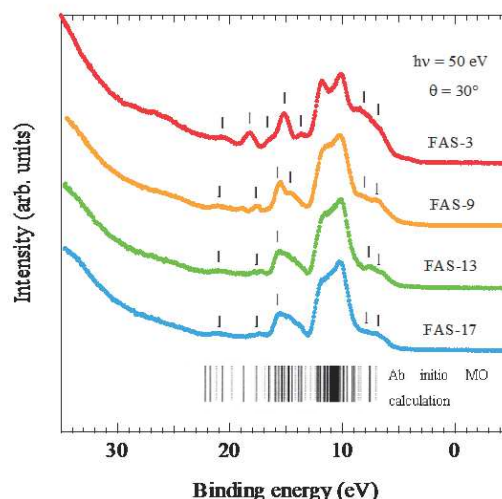


Fig. 3. Photoelectron spectra in the valence band region of FAS-3, FAS-9, FAS-13, and FAS-17. The energy level of the FAS-17 molecule determined by ab initio molecular orbital calculation [4] is plotted at the bottom.

four peaks at 21, 18, 16, and 15 eV became broader. With increasing chain length, the intensity of the peak at 18 eV decreased. From the binding energy position and the intensity, the peak at 18 eV was assigned to the C 2s states of the F-SAMs.

In a previous study [4], Saito et al. calculated the energy level of the FAS-17 molecule by ab initio molecular orbital calculation. In Fig. 3, the energy level of the FAS-17 molecule was compared with the photoelectron spectrum in the valence band region. From the energy level in the calculation, there seems to be a broader peak at around 15 eV and smaller peaks at 7 and 8 eV and between 21 and 18 eV in addition to a sharp peak at 10 eV. On the other hand, the photoelectron spectrum in the valence band region showed a peak at 10 eV, a broader peak at 15 eV, and smaller peaks at 18 and 21 eV. In addition, the width of the valence band was about 15.5 eV in the calculation while that was about 16 eV in the photoelectron spectrum of FAS-17. On the whole, the energy level of the FAS-17 molecule seems to have good correspondence with the photoelectron spectrum in the valence band of FAS-17.

Reference

- [1] Y. Nakai *et al.*, J. Photopolym. Sci. Technol. **23**, 55 (2010).
- [2] S. Sayan *et al.*, Appl. Phys. Lett. **80**, 2135 (2002).
- [3] J. J. Yeh and I. Lindau, At. Data Nucl. Data Tables **32**, 1 (1985).
- [4] N. Saito *et al.*, Surf. Interface Anal. **34**, 601 (2002)

Study on the electronic structure of nitrogen species doped into graphite by nitrogen ion sputtering

Hisao Kiuchi¹, Takahiro Kondo², Junji Nakamura², Hideharu Niwa^{3,4},
Jun Miyawaki^{3,4}, Maki Kawai¹, Masaharu Oshima⁴ and Yoshihisa Harada^{3,4}

¹ Department of Applied Chemistry, University of Tokyo, 7-3-1 Hongo, Bunkyo-ku, Tokyo, Japan

² Faculty of Pure and Applied Sciences, University of Tsukuba, Japan

³ The Institute for Solid State Physics (ISSP), University of Tokyo, Japan

⁴ Synchrotron Radiation Research Organization, University of Tokyo, Japan

Abstract

The electronic structure of nitrogen species incorporated into highly oriented pyrolytic graphite (HOPG), prepared by low energy (200 V) nitrogen ion sputtering and subsequent annealing at 1000 K, were investigated by angle dependent X-ray absorption spectroscopy (XAS). We have developed a program cooperatively controlling a Scienta R3000 analyzer at BL07B and the beamline to measure XAS by the Scienta R3000 as an electron detector. Making use of the surface sensitivity of the Auger electron yield (AEY) mode we have successfully obtained N 1s XAS spectra of low nitrogen doped HOPG with a better S/N and S/B ratios than total yield electron mode. Moreover, it is remarkable that the AEY XAS spectrum of low nitrogen doped N-HOPG was obtained with the S/N ratio comparable to or even better than the partial electron yield XAS spectrum obtained at SPring-8. A highly anisotropic spectrum was obtained at $\theta = 0^\circ$ in N-HOPG (N = 0.8 at.%) by subtracting contributions from the clean HOPG.

Introduction

Recently carbon-based oxygen reduction catalysts have attracted much attention as cathode catalysts alternative to Pt for polymer electrolyte fuel cell [1-3]. These catalysts are modified by light elements (such as nitrogen) and/or transition metals to accelerate oxygen reduction reaction (ORR). The role of the doped light elements and/or the transition metals on the ORR activity has been under debate. In a diverse range of nitrogen-doping methods, a complicated relationship exists between nitrogen doping and ORR activity because many parameters, such as morphology, surface area, and crystallinity, are involved. It is therefore essential to prepare a well-defined reference systems exhibiting not only high crystallinity and surface morphology, but also possessing select nitrogen species. In this study, we have prepared well-defined nitrogen doped carbon materials via low energy (200 V) nitrogen ion sputtering of highly oriented pyrolytic graphite (HOPG). The chemical states of the doped nitrogen, and flatness of the surface were characterized by angle-dependent X-ray absorption spectroscopy (XAS).

Experiments

An HOPG substrate (PGCSTM, Panasonic Inc.) was cleaved in air using adhesive tape, and set in an ultra-high vacuum (UHV) chamber. The substrate was then annealed at 1000 K for 30 min, and sputtered with nitrogen ions at 300 K using an ion gun (OMI-0730, Omegatron Inc.). The acceleration voltage of the ion gun was set to 200 V.

The nitrogen ion dose was estimated from the total ion current divided by the irradiated spot area. The amounts of dosed nitrogen ions were calculated to be 8×10^{13} and 8×10^{14} ions cm^{-2} , respectively, equivalent to 2% and 21% nitrogen ions with respect to the surface carbon atoms. Finally, the samples were annealed at 1000 K for 1 h for surface cleaning. These samples will be referred to as N-HOPG hereafter.

XAS spectra in the total electron yield (TEY), partial electron yield (PEY), and Auger electron yield (AEY) modes were obtained at BL07B in NewSubaru. We have installed a micro channel plate analyzer for the PEY measurement. The AEY spectrum was obtained using a photoelectron analyzer (Scienta R3000). We have developed an original measurement program in order to try surface sensitive XAS by PEY and AEY modes. Anisotropic XAS spectra were obtained by setting the angle θ between the incident X-ray beam and the surface normal to 0° , 45° , and 60° . The samples were annealed at 900 K for 30 min to remove the initially adsorbed gas before XAS measurements were carried out.

Conventional laboratory-based X-ray Photoelectron spectroscopy (XPS) was also performed using a monochromatic Al-K α source (JPS-9010, JEOL) in order to estimate the doped nitrogen content in N-HOPG.

Results and discussion

The total amount of doped nitrogen was estimated to be 0.8 and 2.3 at % from the XPS

result. Figure 1 shows N 1s XAS spectra of N-HOPG (N = 2.3 at.%) at $\theta = 45^\circ$ with different measurement methods (TEY, PEY, and AEY). The spectra were normalized according to the area intensity at π^* region between 396–403 eV. As shown in Fig. 1, the PEY and AEY spectra were successfully obtained. It is noted that the S/N and the S/B ratios of the AEY and PEY XAS spectrum was better than that of TEY.

Three sharp peaks in the π^* region (below 403 eV) are assigned as A: pyridinic N (one nitrogen atom is connected with two carbon atoms), B: cyanide N (a triple bond is formed between a nitrogen and a carbon atom), and C: graphitic N (one nitrogen atom substitutes the carbon site in the graphite plane) [3]. The energy resolution at BL07B was enough to distinguish the electronic structure of each nitrogen moiety in N-HOPG.

Figure 2 shows N 1s XAS spectra of N-HOPG (N = 0.8 at.%) and HOPG at $\theta = 0^\circ$ and 60° with AEY mode. A highly anisotropic spectrum was obtained at $\theta = 0^\circ$ in N-HOPG (N = 0.8 at.%) by subtracting the clean HOPG spectrum from the original one. The similar profile of the PEY XAS spectrum was obtained at BL27SU in SPring-8 for N-HOPG with the similar nitrogen content (N = 0.5 at.%). Considering the lower photon flux of BL07B in NewSubaru than that of BL27SU in SPring-8 it is remarkable that we have successfully obtained the XAS spectrum of low nitrogen doped N-HOPG with a good S/N ratio comparable to or even better than the result at SPring-8. Unlike the reference spectrum, however, only broad AEY XAS profile was obtained at $\theta = 60^\circ$ in N-HOPG. This might be because the present nitrogen sputtering method might have inhomogeneous ion distribution dependent on the sample position and the large beam spot size at BL07B would result in the XAS spectrum of the mixture of these nitrogen components. In order to overcome the problem we should provide a raster scan of the sample during

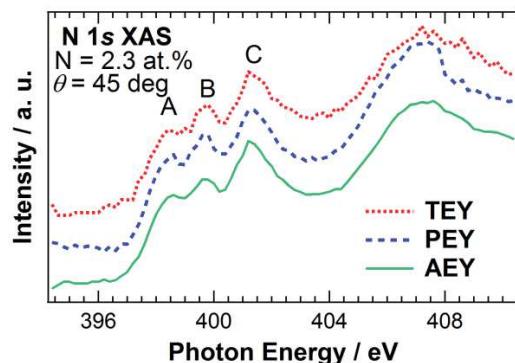


Fig. 1. N 1s XAS spectra of N-HOPG (N = 2.3 at.%). The dotted red, dashed blue, and solid green lines correspond to TEY, PEY, and AEY spectra, respectively.

ion sputtering for more homogeneous nitrogen doping.

We have also tried to study the surface reactivity of N-HOPG using a gas adsorption, however, it was difficult to clean the N-HOPG surface and some oxygen contaminations were present after the annealing at 900 K. We should improve the vacuum and establish the *in situ* sample preparation method.

Acknowledgements

This work was financially supported by the New Energy and Industrial Technology Development Organization (NEDO), Japan. The authors thank Prof. Y. Haruyama for his technical support in the BL07B experiments.

References

- [1] E. Proietti *et al.*, Nat. Commun. **2** (2011) 416.
- [2] K.P. Gong *et al.*, Science **323** (2009) 760.
- [3] H. Niwa *et al.*, J. Power Sources **187** (2009) 93.

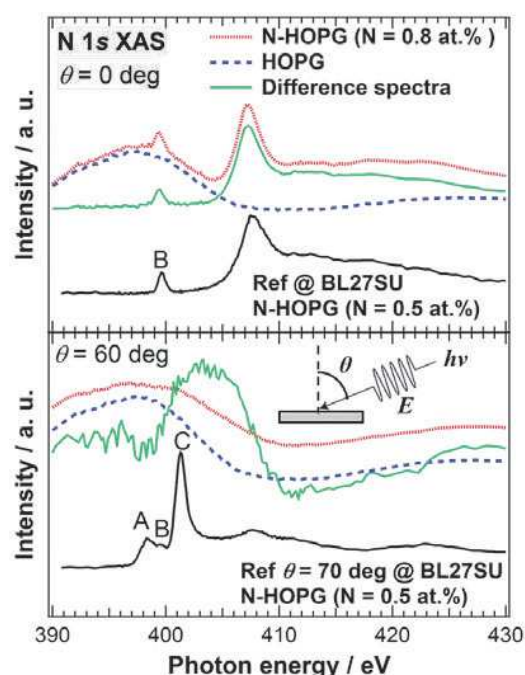


Fig. 2. N 1s XAS spectra of N-HOPG (N = 0.8 at.%). The dotted red, dashed blue, and solid green lines correspond to N-HOPG, HOPG, and difference spectra (“N-HOPG” subtracted by “HOPG”), respectively. The black lines represent the reference N 1s XAS spectra for N-HOPG with the similar nitrogen content (N = 0.5 at.%) obtained at BL27SU in SPring-8.

EUV Resist Chemical Reaction Analysis using SR

Takeo Watanabe¹, Kazuya Emura¹, Daiju Shiono², Yuichi Haruyama¹, Yasuji Muramatsu¹, Katsumi Ohmori¹, Kazufumi Sato², Tetsuo Harada¹, and Hiroo Kinoshita¹

¹University of Hyogo, ⁴Tokyo Ohka Kogyo

Abstract

The chemical reaction in EUV irradiation of the several photoacid generators (PAGs) which employed triphenylsulfonium (TPS) salts as the cation of PAG, is discussed on the basis of the analysis using the SR absorption spectroscopy in the soft x-ray region. The fluorine atoms of the anion PAGs which have the chemical structure of the imidate type such as TPS-Imidate-1, and TPS-Imidate-2 strongly decomposed under EUV exposure. In the case of these PAG type, it is found that in addition to the ionization reaction, the anion decomposition reaction originated by the photo excitation of the photoacid generator might occur under EUV exposures. Thus the sensitivity seemed to be high in comparison to tri-phenylsulfonium perfluorobutanesulfonate (TPS-Nonaflate) under EUV exposure. In the case of tri-phenylsulfonium camphorsulfonate (TPS-Cs), the anion which does not contain fluorine seemed to be very stable under EUV exposure and the sensitivity is lower than that of TPS-Nonaflate.

1. Introduction

The extreme ultraviolet lithography (EUVL)¹⁾ will be used from 16-nm node for the manufacturing semiconductor electronic devices such as memory and MPU devices. And according to the International Technology Roadmap for Semiconductors (ITRS), 8-nm node lithography is required from 2025.²⁾

The top three issues of EUV lithography for high volume manufacturing (HVM) are 1) the achievement of the high power and a long term stable EUV source, 2) the fabrication of the defect free mask and its defect inspection and repair, and 3) the development of the EUV resist which has the high resolution, the high sensitivity, low line width roughness (LWR), and low outgassing and low carbon contamination, simultaneously.

To relax the specification of the EUV power and maintain the high-lithographic throughput, the high sensitive EUV resist is required. The low activation energy chemically amplified³⁻⁵⁾ resist were performed for the high sensitive resist, but the LWR not refined.⁶⁾ The LWR is one of the resist issues to maintain the device electric performance. There are many reports to improved LWR from resist material development. One is the application of compounds of low molecular weight and/or narrow polymer dispersity⁷⁻¹¹⁾ and monomer resist¹²⁻¹⁷⁾ may be one of

the key concepts to resolve this issue due to its reduced molecular size compared with linear polymers against the intended feature print size.

There is a trade-off relationship between resolution, sensitivity, and LWR; so called RLS trade-off.^{18,19)} Now the resolving this trade-off relationship 1X nm node and below becomes very significant and difficult issue.^{20,21)} Thus more fundamental resist studies for 1X nm and below is required to clarify the chemical reaction under EUV exposure.

To increase the sensitivity and decrease the LWR, the acid production yield should increase. Although the acid production yield of the photoacid generator (PAG) of the chemically amplified resist had been studied^{22,23)}, the requirement of the EUV resist was still not satisfied yet. Thus, more effective fundamental work should require to be clarified the chemical reaction under EUV exposure. The photo-ionization (ionization) reaction might be dominant and the secondary electron plays the important role in the chemical reaction under EUV exposure²³⁾. In addition, we had found out that the decomposition reaction was occurred near the large photo absorption atom in the solvent, so called "solvent effect"²⁴⁾. In the case of the PAG chemical reaction analysis in EUV irradiation, not only ionization reaction but also the

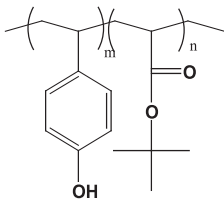
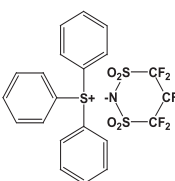
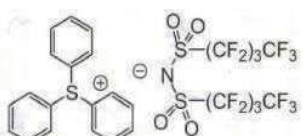
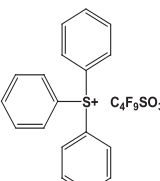
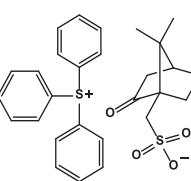
direct excitation in EUV irradiation might be needed to achieve the high sensitive EUV resist. In the previous report, for resists which employed tri-phenylsulfonium cyclo(1,3-perfluoropropanedisulfone) imidate (TPS-Imidate-1) and tri-phenylsulfonium perfluorobutane-sulfonate (TPS-Nonaflate) as PAGs, the peak at the absorbance at 1156 cm^{-1} in the fourier transform infrared (FT-IR) spectra increased after EUV exposure.²⁵⁻²⁹⁾ As a results of the electron orbital calculation using perturbation theory by the software code Gaussion03³⁰⁾, the peak at approximately 1156 cm^{-1} in FT-IR spectra of resist A corresponds to the C-F bonding of the anion of TPS-Imidate-1. However, there was no change in the FT-IR spectra of resist which include TPS-Nonaflate, between before and after EUV exposure. As a result, the outgassing

2.Experimental

2.1. Materials for the Model Resists

The model resists which were employed in this study are shown in Table 1. The resists A, B, C, and D employed poly (hydroxystyrene-co-t-butylacrylate) (PHS-TBA) as the base polymer, and propyleneglycol monomethyletheracetate (PGMEA) as a solvent. The model resists A does not include any photoacid generator. Model resists, A, B, C and D employed TPS-Imidate-1 and TPS-Imidate-2, TPS-Nonafalte, and TPS-Cs as the photoacid generator, respectively. The PAG content#1 and content#2 ratio to the base resin such as PHS-TBA is approximately 2 mol% and 6 mol% of the base polymer for the sensitivity measurement and the SR absorption spectroscopy experiment, respectively. In sensitivity measurement, the PAG

Table 1. Chemical structure and contents of the model resists.

Sample	Resist A	Resist B	Resist C	Resist D
Base polymer	 <p>poly (vinylphenol-co-tert butylacrylate) (PHS-TBA)</p>			
Photoacid generator	<p>TPS-Imidate-1</p> 	<p>TPS-Imidate-2</p> 	<p>TPS-Nonaflate</p> 	<p>TPS-Cs</p> 
(content#1)	(2.04 mol%)	(1.34 mol%)	(2.02 mol%)	(2.09 mol%)
(content#2)	(6.11 mol%)	(4.03 mol%)	(6.06 mol%)	(6.18 mol%)
Solvent	propylene glycol monomethylether acetate (PGMEA)			

measurements and the FT-IR spectra measurements indicated that the EUV-induced reaction of TPS-Imidate-1 occurred more efficiently than that of TPS-Nonaflate. To clarify the difference of the anion decomposition, the analysis using SR spectroscopy is performed. This paper focused on the chemical reaction analysis of the model chemically amplified resists which contains several PAG on the basis of tri-phenylsulfonium by the SR absorption spectroscopic method³²⁾.

content#1 of 2 mol% is a normal value. However, the PAG content for SR absorption spectroscopy experiment should be larger than that for sensitivity measurement, because in SR spectroscopy experiment the signal from the atomic elements of the resist film is too small when the PAG content is 2 mol%.

The resist solution was spin coated on a 4-inches silicon wafer and the prebake was carried out on a hot plate at the temperature of 130°C in the time period of 90 s. The film thickness was measured by

Nanometrics 6100A (NANOmetrics) and the resist film thickness was spin-coated to be 50 nm on a wafer. The EUV exposure to obtain the sensitivity curve in high accuracy, the resist sensitivity evaluation⁸⁾ system which can simulate the EUV exposure spectrum of the six-mirror-imaging optics was installed at the BL3 beamline in NewSUBARU synchrotron radiation facility³¹⁾ was utilized. This EUV spectrum which is same as the practical exposure tool such as ASML NXE3100B can be produced by the seven-time reflection by three-mirror optics.

2-2. SR photo absorption spectroscopy³²⁾

X-ray spectroscopy (XPS) is a beneficial measurement method to analyze the atomic chemical behavior of the material. However, for the absorption spectroscopy measurement of the atomic which is a small content such as the photoacid generator of the EUV resist, the high brilliance light source such as synchrotron radiation (SR) light is beneficial in absorption spectroscopy. Thus, soft x-ray of the SR absorption spectroscopy was employed for the chemical reaction analysis for the EUV resist materials.

The SR absorption spectroscopy measurements were performed at the end station of the BL07B beamline at the NewSUBARU synchrotron radiation facility. The short undulator was employed as a light source of this beamline. This beamline consists of three glancing mirrors such as M_0 , M_1 and M_2 , the monochromator (G), the entrance (S_1) and exit (S_2) slits and the end station exposure and analyzing chambers. The loadlock chamber was adapted to these chambers to exchange the sample. The variable-line-spacing plane gratings (VLSPG) were employed as monochromator. Three density types such as 600, 1200, and 2400 lines/mm were installed in the monochromator vacuum chamber. The photon energy region is from 80 eV and 800 eV in the SR spectroscopy. The exit slit size is 20 $\mu\text{m(H)} \times 20 \mu\text{m(V)}$ and the SR light spot size on a sample is 1 mm(H) \times 1 mm (V). The energy resolution $E/\Delta E$ is approximately 1000. The photon flux of the photon energy of 91.8 eV ($\lambda=13.5 \text{ nm}$) is approximately 3.0×10^{11} photons/s/100mA. The absorption signal was obtained from the ratio of the photocurrent from the

sample to the photocurrent from the gold mesh. The total energy resolution was approximately 0.1 eV. The photocurrent was measured by the electrometer (6514, Keithley).

The photon energy calibration was carried out by measuring the photon absorption spectrum of highly oriented pyrolytic graphite (HPOG). The photon energy at the absorption peak of the carbon π^* -bonding was adjusted at the photon energy of 285.5 eV.

For the absorption measurement of carbon 1s core level, the measured energy region is 280-330 eV and 1200 lines/mm VLSPG was employed with the undulator gap of 48.0 mm. For the absorption measurement of fluorine 1s core level, the measured energy region is 685-735 eV and 2400 lines/mm VLSPG was employed with the undulator gap of 52.0 mm. The electron current generated on the sample is measured in the SR absorption experiment during the SR light exposure.

3. Results and Discussions

3.1 Sensitivity

The sensitivities curves of the resists A, B, C and D under EUV are shown in Fig. 1. The E_0 values which is the exposure dose to clear the resist remained thickness after the development, of resists A, B, C and D are 1.1 mJ/cm^2 , 2.7 mJ/cm^2 , 3.8 mJ/cm^2 , and 6.0 mJ/cm^2 , respectively. The sensitivity differences of resists A, B, C, and D under EUV exposure would be discussed by the analysis of the SR photo absorption spectroscopy in the soft x-ray region.

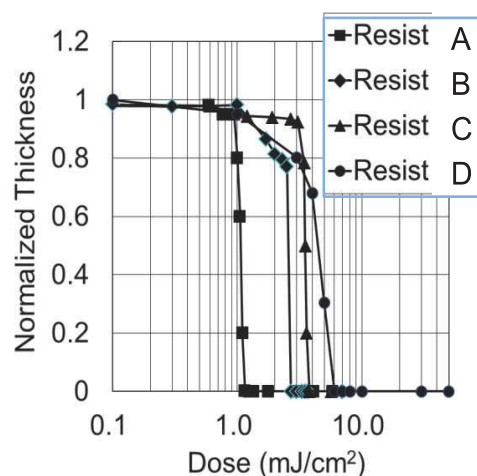


Fig.1 Sensitivity curves under EUV exposure for model resist A, B, C, and D.

3.2 SR absorption spectroscopy

The absorption spectra of carbon 1s core level for resists A, B, C and D were measured as shown in Figs. 2, 3, 4 and 5, respectively. For each sample the measured energy range was from 280 eV to 330 eV. To highlight the peak height changes, the SR absorption spectra were plotted in the energy region from 280 eV to 295 eV. The absorption peak at 285.5 eV is corresponding the π^* -bonding of the benzyl group in the cation of PAG (TPS). From the outgassing results²⁵⁻²⁹, this changes correspond to the cation of PAG such as TPS decomposition occurred by the secondary electron originated by the EUV irradiation as shown in Fig. 6. As the increasing the EUV dose, the absorption spectra of the π^* -bonding became smaller. Furthermore, the absorption peak at 287 eV corresponds to the σ^* -bonding of the protection group of tert-butylacrylate (TBA) of the base polymer. From the outgassing results²⁵⁻²⁹, this changes correspond only to the protecting group decomposition reaction of TBA in base polymer occurred by the secondary electron originated by the EUV irradiation as shown in Fig. 7.

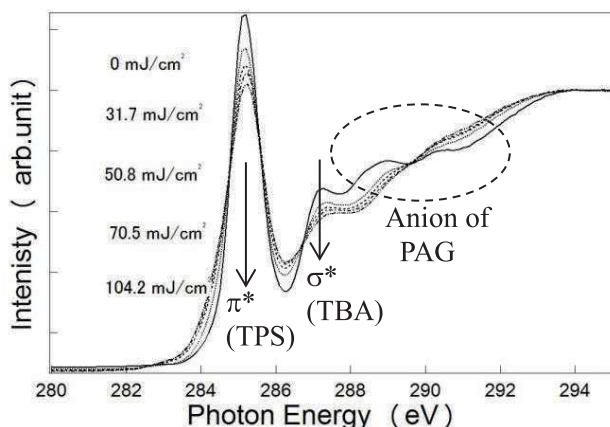


Fig. 2 SR absorption spectra carbon 1s core level in resist A.

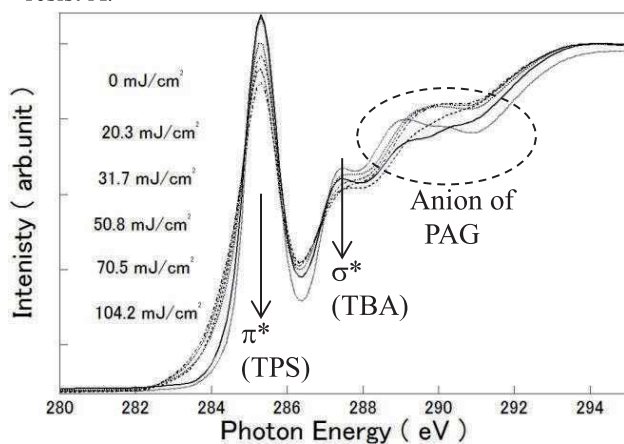


Fig. 3 SR absorption spectra carbon 1s core level in resist B.

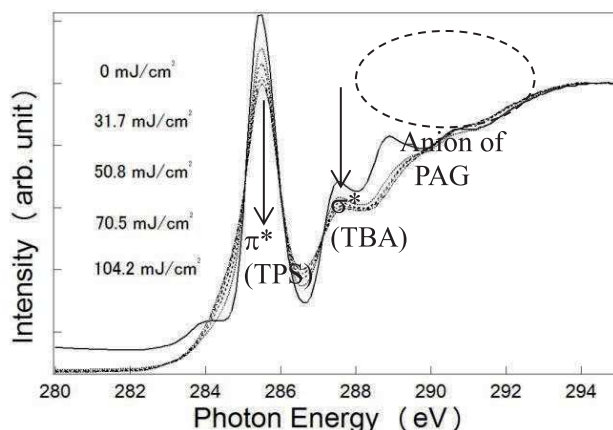


Fig. 4 SR absorption spectra of carbon 1s core level in resist C.

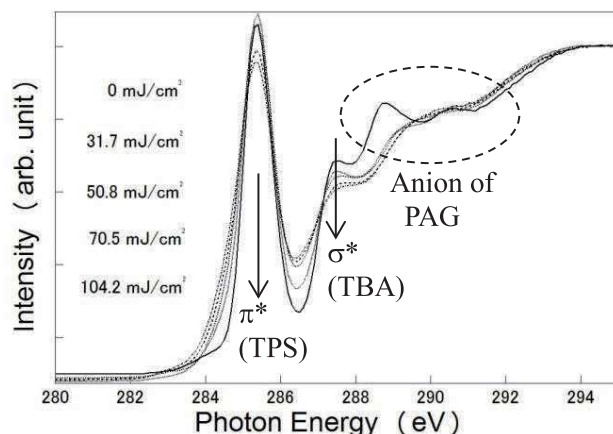


Fig. 5 SR absorption spectra of carbon 1s core level in resist D; (a) 280 eV-330 eV, and (b) 285 eV-295 eV.

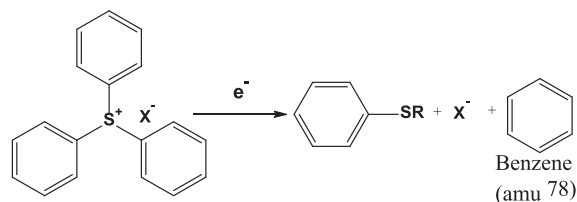


Fig. 6 Decomposition reaction of the triphenylsulfonium employed as the cation of PAG by the secondary electron.

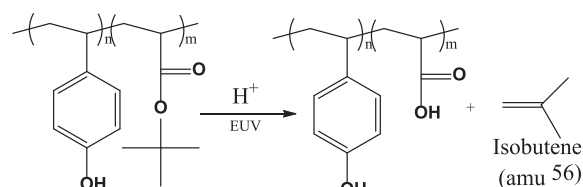


Fig. 7 Decomposition reaction of PHS-TBA.

The absorption spectra of fluorine 1s core level for resists A, B and C were measured by the SR absorption spectroscopic method. Figures 8, 9, and 10 show the EUV exposure dose dependency of the

absorption of fluorine 1s core level in resists A, B, and C, respectively. In comparison of Figs 8, 9, and 10, the fluorine of the anion of the PAG in resists A and B decompose easily rather than that of the anion of PAG in resist C.

As the results, the resist including imidate type in the anion of PAG which is easy to decompose in EUV irradiation has higher sensitivity rather than others. On the other hand, for TPS-Cs, there is not changes in the oxygen 1s core spectra as increasing EUV exposure dose. Thus as the anion of TPS-Cs is very stable, resist including TPS-Cs has lowest sensitivity.

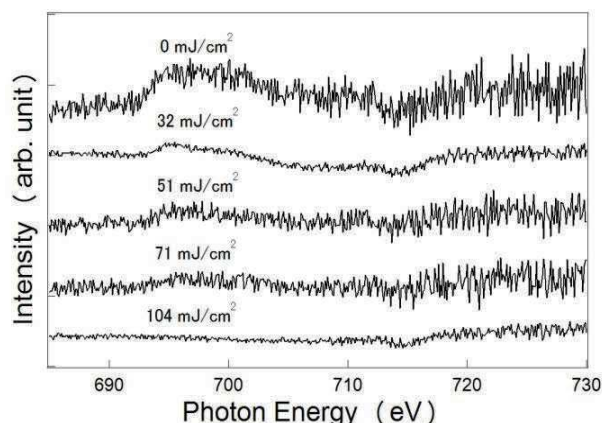


Fig. 8 SR absorption spectra of fluorine 1s core level for resist A.

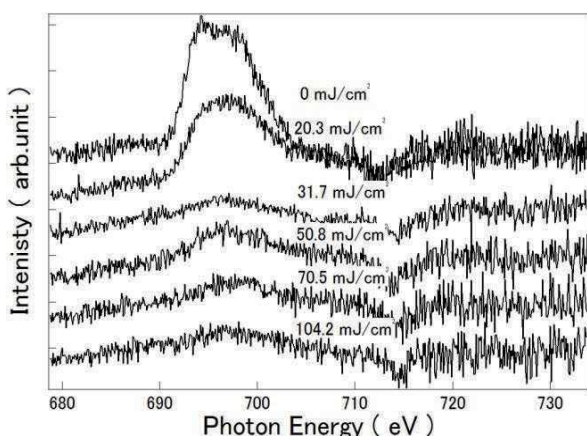


Fig. 9 SR absorption spectra of fluorine 1s core level for resist B.

In addition, to control the line edge roughness, generally shortening the acid diffusion in chemically amplified resist during PEB might be beneficial by increasing the molecular size of the anion of PAG. However, if the decomposition reaction of the anion of PAG in EUV irradiation is occurred strongly, the acid diffusion length might become large. Thus, the simultaneous achievement of the high sensitive and

the shortening LWR, the anion decomposition reaction based on the direct excitation of PAG should be considered and analyzed.

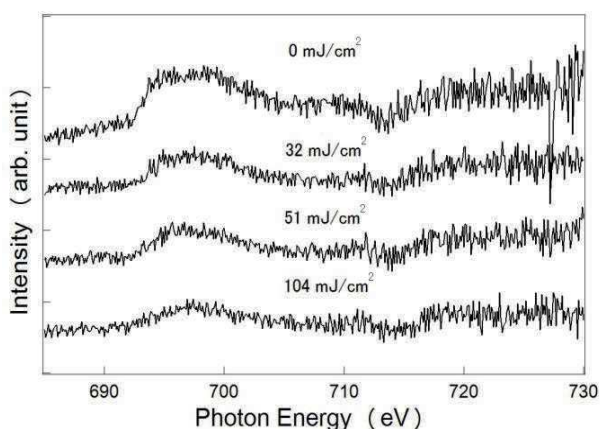


Fig. 10 SR absorption spectra of fluorine 1s core level for resist C.

Figure 11 shows two scheme of the decomposition reaction of the Imidate type PAG reaction under EUV irradiation. In Fig. 11(a), R Ph, and X⁻ indicate the base polymer such as PHS polymer, the benzyl group of the cation of PAG, and the anion of PAG, respectively. In Fig. 10(b), X⁻ is the anion of PAG, and X₁⁻, X₂⁻, and X₃⁻ are decomposition species from the anion of X⁻. which has a negative charge. N₁, N₂, and N₃ are decomposition component which have a neutral charge. The dominant chemical reaction of the EUV light is ionization and the cation of the PAG decomposes by secondary electron as shown in Fig. 11(a).

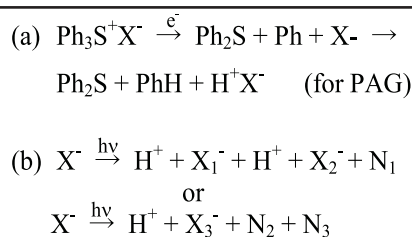


Fig. 11 (a) The decomposition reaction by the secondary electron generated from the ionization reaction and (b) the decomposition reaction of the anion of PAG by the direct excitation reaction under EUV irradiation.

For the decomposition reaction of the anion of PAG, it seems to not occur by the secondary electron. In the case of Imidate of PAG, the anion of PAG decomposes by the direct excitation of PAG as shown in Fig. 11(b). Therefore, the EUV sensitivity of the model resists which contain Imidate as the

anion of PAGs are higher than that contains Nonaflate and Cs as the anion of PAGs.

Therefore, the low sensitivity of the model resist contains TPS-Cs depends on the stable chemical structure of the anion of PAG. Otherwise, the high sensitivity of the model resist contains TPS-Imide-1 and TPS-Imide-2 depend on the decomposition reaction of the anion of PAG.

4. Conclusion

The chemical reaction in EUV irradiation of the several photoacid generators (PAGs) which employed triphenylsulfonium (TPS) salts as the cation of PAG, is discussed on the basis of the analysis using the SR absorption spectroscopy in the soft x-ray region. The fluorine atoms of the anion PAGs which have the chemical structure of the imide type such as TPS-Imide-1, and TPS-Imide-2 strongly decomposed under EUV exposure. In the case of these PAG type, it is found that in addition to the ionization reaction, the anion decomposition reaction originated by the photo excitation of the photoacid generator might occur under EUV exposures. Thus the sensitivity seemed to be high comparison to tri-phenylsulfonium perfluorobutanesulfonate (TPS-Nonaflate) under EUV exposure. In the case of tri-phenylsulfonium camphorsulfonate (TPS-Cs), the anion which does not contain fluorine seemed to be very stable under EUV exposure and the sensitivity is lower than TPS-Nonaflate.

The SR absorption spectroscopy is a powerful analysis method to analyze the decomposition reaction of the anion of PAG. To satisfy the specification of the EUV resist which require for high volume manufacturing, all the chemical reaction should be taken in account, such as the ionization and the direct excitation reactions. Increasing the sensitivity, it might have more space to achieve the low LWR resist.

References

- H. Kinoshita, K. Kurihara, Y. Ishii and Y. Torii, *J. Vac. Sci. & Technol.*, B7 (1989) 1648.
- International Technology Roadmap for Semiconductors 2011 Edition.
- H. Ito, C. G. Willson, and J. M. J. Frechet, *Digest of Tech. Papers 1982 Symp. VLSI Tech.*, (1982) 86.
- H. Ito and C. G. Willson, *Polym. Eng. Sci.*, **23** (1983) 1012.
- H. Ito, G. Breyta, D. Hofer, R. Sooriyakumaran, K. Petrillo, and D. Seeger, *J. Photopolym. Sci. Technol.*, **7** (1994) 433.
- J. W. Thackeray, R. A. Nassar, K. Spear-Alfonso, T. Wallow, B. LaFontaine, *J. Photopolym. Sci. Technol.*, **19** (2006) 525.
- D. C. Tully, A. R. Trimble and J. M. J. Frechet, *Adv. Mater.* **12** (2000) 1118.
- J.B. Kim, H. J. Yun and Y.-G. Kwon, *Chem. Lett.*, **10** (2002), 1064.
- M. Ishida, J. Fujita, T. Ogura, Y. Ochiai, E. Ohshima and J. Momoda: *Jpn. J. Appl. Phys.*, **42** (2003) 3913.
- T. Kadota, M. Yoshiiwa, H. Kageyama, F. Wakaya, K. Gamo and Y. Shiota, *Proc. SPIE*, **4345** (2001) 891.
- J. B. Kim, Y.-G. Kwon, T. Fujigaya, Y. Shibasaki and M. Ueda, *J. Mater. Chem.*, **12** (2002) 53.
- T. Hirayama, D. Shiono, H. Hada and J. Onodera, *J. Photopolym. Sci. Technol.*, **17** (2004) 435.
- H. Hada, T. Hirayama, D. Shiono, J. Onodera, T. Watanabe, S. Y. Lee and H. Kinoshita, *Jpn. J. Appl. Phys.*, **44** (7B) (2005) 5824.
- Daiju Shiono, Hideo Hada, Kazufumi Sato, Yasuyuki Fukushima, Takeo Watanabe, and Hiroo Kinoshita, *J. Photopolym. Sci. Technol.*, **22**, (2009) 737.
- H. Kudo, R. Hayashi, K. Mitani, T. Yokozawa, N. C. Kasuga, and T. Nishikubo, *Angew. Chem. Int. Ed.*, **45**, (2006) 7948.
- H. Seki, S. Kuwabara, H. Kudo and T. Nishikubo, *Chemistry Letters*, **40**, (2011) 464.
- Hiroto Kudo, Nobumitsu Niina, Tomoharu Sato, Hiroaki Oizumi, Toshiro Itani, Takuro Miura, Takeo Watanabe and Hiroo Kinoshita, *J. Photopolymer Sci. Technol.*, **25** (2012) 587.
- T. Watanabe, H. Kinoshita, H. Nii, K. Hamamoto, H. Hada, H. Komano, and S. Irie, *J. Vac. Sci. Technol.*, B19 (2001) 736.
- K. Hamamoto, T. Watanabe, H. Hada, H. Komano and H. Kinoshita, *J. Photopolym. Sci. Technol.*, **15** (2002) 361.
- Yasuyuki Fukushima, Naoki Sakagami, Teruhiko Kimura, Yoshito Kamaji, Takafumi Iguchi, Yuya Yamaguchi, Masaki Tada, Tetsuo Harada, Takeo Watanabe, and Hiroo Kinoshita, *Jpn. J. Appl. Phys.*, **49** (2010) 06GD06-1.
- Takuro Urayama, Takeo Watanabe, Yuya Yamaguchi, Naohiro Matsuda, Yasuyuki Fukushima, Takafumi Iguchi, Tetsuo Harada, and Hiroo Kinoshita, *J. Photopolymer Sci. Technol.*, **23** (2011) 681.
- T. Kozawa, A. Saeki, K. Okamoto and S. Tagawa, 3rd EUVL Symposium 2004.
- T. Kozawa, H. Yamamoto, A. Saeki, and S. Tagawa, *J. Vac. Sci. Technol.*, B **23** (2005) 2716.
- T. Watanabe, K. Hamamoto, H. Kinoshita, H. Hada and H. Komano, *Jpn. J. Appl. Phys.*, **43** (2004) 3713.
- H. Hada, T. Watanabe, H. Kinoshita and H. Komano, *J. Photopolym. Sci. Technol.*, **18** (2005) 475.
- T. Watanabe, H. Hada, S. Y. Lee, H. Kinoshita, K. Hamamoto and H. Komano *Jpn. J. Appl. Phys.*, **44** (2005) 5866.
- T. Watanabe, Y. Haruyama, D. Shiono, K. Emura, T. Urayama, T. Harada, and H. Kinoshita, *J. Photopolymer Sci. Technol.*, **25** (2012) 569.
- T. Watanabe, H. Hada, H. Kinoshita, Y. Tanaka, H. Shiotani, Y. Fukushima and H. Komano: *Proc. SPIE*, **6153** (2006) 615343-1.
- T. Watanabe, H. Hada, Y. Fukushima, H. Shiotani, H. Kinoshita and H. Komano, *Synchrotron*

- Radiation Instrumentation: Ninth International Conference*, AIP **879** (2007) 1470.
30. Gaussian03 electron orbital calculation software is informed in URL:<http://www.gaussian.com/home>.
 31. S. Hashimoto, A. Ando, S. Amano, Y. Haruyama, T. Hattori, K. Kanda, H. Kinoshita, S. Matsui, H. Mekar, S. Miyamoto, T. Mochizuki, M. Niibe, Y. Shoji, Y. Utsumi, T. Watanabe and H. Tsubakino, *Trans. Mater. Res. Soc. Jpn.*, **26** (2001) 783.
 32. T. Watanabe, Y. Haruyama, D. Shiono, K. Emura, T. Urayama, T. Harada, and H. Kinoshita, *J. Photopolymer Sci. Technol.*, **25** (2012) 569.

Compact Soft X-ray Emission Spectrometer at BL-09A in NewSUBARU

Masahito Niibe¹ and Takashi Tokushima^{2,1}
¹LASTI, University of Hyogo, ²RIKEN SPring-8 Center

Abstract

A compact soft X-ray emission spectrometer for the low energy region of 50-600 eV has been designed and constructed for the long undulator beamline BL-09A in the NewSUBARU SR facility. The optical design of the spectrometer is based on a grazing incidence flat-field spectrometer using a valid line-spacing grating. The average groove density of the grating is 2000 L/mm. The distances from the slit to the grating and from the grating to the CCD are 355 mm and 650 mm, respectively. The energy resolution, $E/\Delta E$, was estimated to be greater than 1000 in the energy range of 50-600 eV. Spectra of K-emission X-rays of several light elements, such as B, C, N, and O, from various samples were successfully obtained.

Introduction

With the high brilliance of a soft X-ray radiation source, the study of electronic states by the soft X-ray emission spectroscopy (SXES) method is attracting attention in areas such as lithium ion batteries, fuel cells, compound semiconductors, and photocatalysts. This technique involves a spectroscopy of photons emitted with extra energy as X-rays, which is generated by the transition of electrons in the valence band to the inner shell holes, which are formed by irradiation of the excitation X-rays; the holes are then backfilled in its relaxation process. In addition to a simple X-ray fluorescence emission, spectroscopy also includes an emission process, such as that of resonant inelastic X-ray scattering (RIXS). The technique can provide knowledge about the partial density of states that cannot be obtained by the X-ray photoelectron spectroscopy (XPS) method. Also, the penetration depth of soft X-rays is deeper as compared with the electron beam it is expected to use for the electronic state analysis of the bulk and the interfacial layer.

On the other hand, light elements across Li-F as constituent elements of various functional materials are also important as additive elements. Therefore, in addition to analysis by the absorption method, analysis of the electronic state or chemical bonding state by X-ray emission spectroscopy is expected in a variety of industrial materials in the future. However, the soft X-ray emission efficiency of these light elements is low, and it becomes lower the smaller the atomic number becomes. Therefore, a strong excitation light source is necessary for SXES measurement. The NewSUBARU SR facility is equipped with a long undulator (LU) with a total length of approximately 11 m, and its photon flux density is as high as 1.2×10^{11} photons/sec at the sample position. Therefore, it is suitable as an excitation light source for SXES of the light elements. We

focused on the energy region of 50-600 eV and have developed SXES equipment of high energy resolution at BL-09A in the NewSUBARU.

Design and construction of the spectrometer

The optical design of the spectrometer is based on a grazing incidence flat-field spectrometer using a valid line-spacing (VLS) grating. Because there is a limitation of the spatial space, a HEPA2.5 (High Efficiency Photon energy Analyzer Ver.2.5) spectrometer [1], which had relatively high resolution even in a small size, was adopted for the design of the spectrometer. Because the size of the beam spot in the BL-09A analysis station has values of 0.2 mm vertical \times 0.8 mm horizontal FWHM, it is necessary to use an entrance slit for the expected high energy resolution. The entrance slit was placed 10mm from a sample, whose opening width can be changed 5-300 μm from outside of the vacuum chamber. The HEPA spectrometer uses a varied line-spacing grating on a spherical substrate, and the dispersed light is focused onto the charge-coupled device (CCD) plane. The optimal range for analyzing energy was 50-600 eV. The

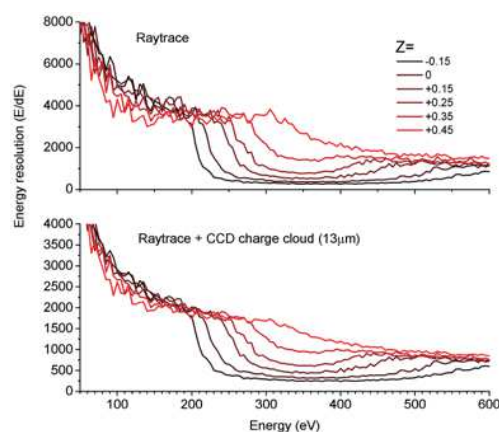


Fig. 1 Ray-trace calculated energy resolution of the spectrometer by changing the height, Z

spectrometer is very compact; the distances between the slit and the grating and between the grating and the CCD center are 355 mm and 650 mm, respectively.

The estimated energy resolution by ray-tracing simulation is shown in Fig. 1. In this calculation, a fine adjustment of the spectrometer height, Z , is supposed according to the range of the photon energy measured. Taking into account the contribution of the electron cloud on CCD, the energy resolution, $E/\Delta E$, was estimated to be greater than 1000 in the energy range of 50-600 eV. Furthermore, the energy resolution is a few thousands in the energy region smaller than 200 eV.

Performance test

The spectrometer was constructed at the endstation of beamline BL-09A in March 2014. Figure 2 gives an overview of the spectrometer.

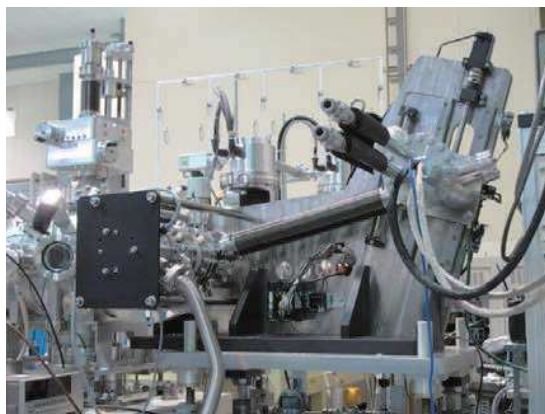


Fig. 2 Soft X-ray emission spectrometer constructed at BL-09A at the NewSUBARU SR facility

Adjustment of the spectrometer was started in Apr. 2014, and it is now in operation. B-K, C-K, N-K, Ti-L, and O-K emissions of various samples were successfully measured with high energy resolution. Figure 3 shows an example of a CCD image of N-K emission light from an Si_3N_4 thin film. Horizontally polarized soft X-rays with excitation energy well above the N1s ionization threshold were irradiated on the sample at a 45 degree angle of incidence. The typical exposure time for one spectrum was 20-30 min without trident mirror optics [2]. The sharp upper line in Fig. 3(a) reflects elastic scattering of the excitation X-rays. The broad lower line in Fig. 3(a) reflects the fluorescent X-rays from the Si_3N_4 sample. The images of line spectra are almost straight. The deviation from a line due to aberrations is corrected by polynomial approximation calculation.

The reconstructed spectrum of N-K emission light from the Si_3N_4 thin film is shown in Fig. 3(b).

The sharp peak at 420 eV is the elastic scattering of excitation X-rays. The broad peaks of approximately 390 eV in Fig. 3(b) are the fluorescent X-rays from the Si_3N_4 sample. The shape of the fluorescence peaks is in good agreement with that previously reported. The total energy resolution, including the beamline monochromator resolution, now was estimated to

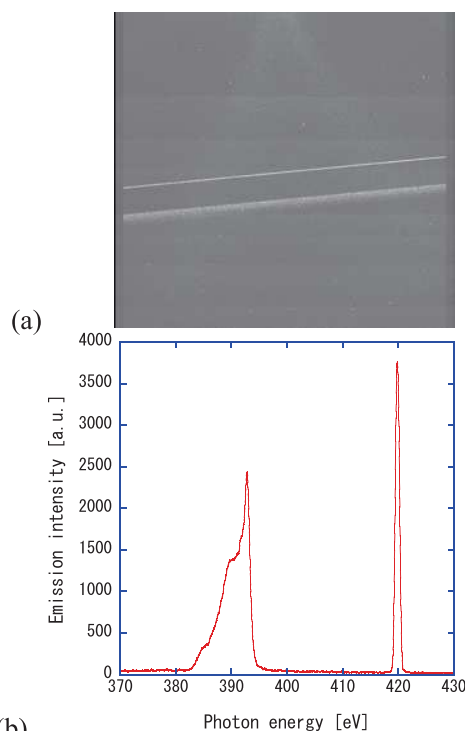


Fig. 3 (a) CCD image of N-K emission light from an Si_3N_4 thin film and (b) reconstructed spectrum

be $E/\Delta E \sim 700$ and ~ 1000 at approximately 400 eV and 300 eV, respectively.

Conclusion

A compact SXE spectrometer for the low energy region of 50-600 eV was constructed for the long undulator beamline BL-09A at the NewSUBARU SR facility.

The energy resolution, $E/\Delta E$, was estimated to be greater than 1000 for $E = 50-600$ eV.

Emission spectra in the energy range of $E = 150-600$ eV were successfully measured for various samples composed of light elements B, C, N, and O.

Acknowledgment

This work was performed under the auspices of MEXT under the contract subject "Project for Creation of Research Platforms and Sharing of Advanced Research Infrastructure."

References

- [1] T. Tokushima *et al.*, Rev. Sci. Instrum. **77**, 063107 (2004).
- [2] T. Tokushima *et al.*, Rev. Sci. Instrum. **82**, 073108 (2011).

Surface analysis of AlGa_N treated by CF₄ and Ar plasma etching

Shodai Hirai¹, Masahito Niibe¹, Retsuo Kawakami², Tatsuo Shirahama², Yoshitaka Nakano³, and Takashi Mukai⁴

¹University of Hyogo, ²Tokushima University, ³Chubu University, ⁴Nichia Corporation.

Abstract

In order to understand the details of the surface damage to the AlGa_N film by plasma etching, we etched it with CF₄ and Ar plasmas. The composition ratios, Al/N and Ga/N obtained by X-ray photoelectron spectroscopy (XPS) of the AlGa_N surface etched by Ar plasma increased more significantly than those of CF₄ plasma. The peak shape of near-edge X-ray absorption fine structure (NEXAFS) spectra in the N-K absorption edge was broadened by CF₄ plasma etching with increased processing time. In the case of Ar, it was more significantly broadened than that etched by CF₄ plasma. From the above results, the changes in the crystalline structure of AlGa_N are considered to be caused by the synergistic effect of UV light irradiation from plasma and ion bombardment to the sample surface. We found that the change in the surface composition, the disordering of the crystalline structure occurred on a shallow region from the surface, and those did not occur on a deeper region of the sample.

Introduction

AlGa_N/Ga_N heterostructures have been studied as a high electron mobility transistor (HEMT) operable at high frequency, high power and high temperature [1]. In this structure, the two-dimensional electron gas (2DEG) with a high carrier concentration and high mobility is induced to an AlGa_N/Ga_N interface [2]. However, there are several problems for the application of the AlGa_N/Ga_N HEMT. The AlGa_N/Ga_N HEMT is essentially a normally-on operation by the 2DEG, and the drain current flows even if the gate voltage is 0 V. However, in view of the fail-safe in the power devices, normally-off operation is desired as the drain current does not flow when the gate voltage is 0 V [3]. Power saving is also expected if it is possible for the AlGa_N/Ga_N HEMT to have a normally-off operation [4].

Recently, it has been reported that the device became normally-off by treating the AlGa_N film with CF₄ plasma [4]. However, the mechanisms and the related surface damage were not yet known. Previously, we investigated the effect of etching on the n-Ga_N surface by Ar plasma [5]. As a result, we reported that surface roughening occurs clearly in n-Ga_N by the synergistic effect of UV light irradiation from the plasma and ion bombardment on the sample surface [5]. However, we have not yet fully investigated it in relation to the AlGa_N sample. Therefore, AlGa_N films were etched with

CF₄ and Ar plasmas, and the treated surfaces were analyzed by various methods. Although we have reported a part of the study, such as surface shape variation, elsewhere [6], a microscopic understanding of the etching damage is insufficient. In this study, the changes in surface composition and crystalline structure of AlGa_N etched by CF₄ and Ar plasmas were mainly analyzed using XPS and NEXAFS methods. We discuss a difference between the etching damage by the CF₄ and Ar plasmas.

Experimental Methods

The sample was a 100-nm-thick AlGa_N (Al_{0.24}Ga_{0.76}N) film grown on a Ga_N surface by metal-organic chemical vapor deposition (MOCVD). Plasma etching was carried out using a capacitively coupled plasma (CCP) with a radio frequency (13.56 MHz) of 200 V. CF₄ and Ar were used as the plasma source gases. The gas pressure of the plasma was varied between 10 and 100 mTorr. The time of the plasma etching was varied from 5 to 100 min [5]. The spectrum of ultraviolet (UV) light emitted from the plasmas was measured using a visible-ultraviolet spectrometer (Ocean Optics, USB4000).

The sample surface compositions were determined using XPS (Shimadzu, ESCA-1000). The peak area intensities of Al2p, Ga3d, N1s and F1s were calculated using the Shirley method from

the measured XPS spectra. The composition ratio was calculated as the Al/N and Ga/N ratios of the as-grown sample equal one. We also determined the F/N ratio with using the relative sensitivity coefficient of N1s to F1s to be 0.42 [7].

The change in the atomic bonding state of the sample surface was evaluated by X-ray absorption spectroscopy (XAS). We measured the NEXAFS spectrum of the N-K absorption edge (388–432 eV). The NEXAFS measurement was carried out at the analyzing station of beamline BL-09A at the NewSUBARU synchrotron radiation facility at the University of Hyogo. The angle of incidence of soft X-rays was 90° from the surface. The measurements of total electron yield (TEY) and total fluorescent yield (TFY) methods were performed at the same position for the same sample. The TEY method can obtain information on a shallow region of less than about 5 nm from the sample surface because of the short escape length of photogenerated electrons. On the other hand, the TFY method can obtain information on a deeper region (bulk) of the sample, more than 100 nm, because X-ray fluorescence comes from a deeper place in the sample compared to electrons. In the TFY method, we measured the amount of fluorescence with 40 nm Al-coated photodiode in order to cut off visible light emission [8].

Results

Figure 1 shows the spectrum of the UV light emitted from (a) CF₄ and (b) Ar plasma during the etching. As shown in Fig. 1(a), the intensity of the UV light emitted from the CF₄ plasma is very weak, and the peak of the spectra was not clearly observed at the gas pressure between 10 and 100 mTorr. In contrast, in the case of Ar as shown in

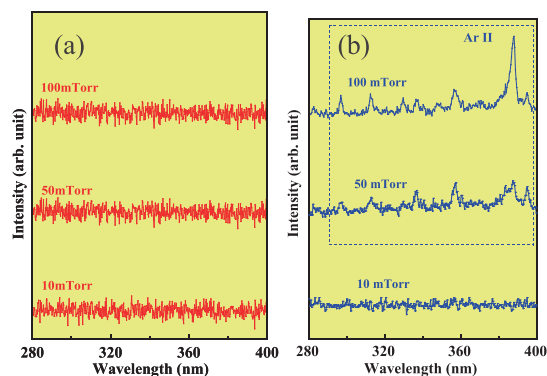


Fig. 1. Spectra of the light emitted from (a) CF₄ and (b) Ar plasmas during etching.

Fig. 1(b), the peak was not observed at the gas pressure of 10 mTorr, but it was observed at the gas pressure of 50 and 100 mTorr [9]. This indicates that the intensity of the UV light emitted from the CF₄ plasma was much weaker than that of the Ar plasma.

The etch depth of the etched AlGaIn surface with a processing time of 100 min was about 60 nm regardless of the change in the gas species and gas pressure [6]. The SEM images of the AlGaIn surfaces etched by the CF₄ plasma of each gas pressure were as smooth as the as-grown surface; pronounced surface roughening did not occur. On the other hand, in the case of Ar, the surface roughening occurred at a gas pressure of 50 mTorr, and pit-like defects were generated on the surface at a gas pressure of 100 mTorr (not shown here).

Figure 2 shows the processing time dependence of the composition ratio of the surface etched by CF₄ and Ar plasmas at a gas pressure of 100 mTorr. Figure 2(a) shows the Al/N and Ga/N ratios, and Fig. 2(b) shows the F/N ratio. As shown in Fig. 2(a), the Al/N and Ga/N ratios of the surface etched by CF₄ plasma increased to about 1.3 times with a processing time of 5 min. However, after that, the ratios did not increase with increased processing time. On the other hand, the values for Ar plasma increased to about 2.3 times with increased processing time. With regard to the CF₄ and Ar gases, these values also changed similarly when etching at a gas pressure of 10 and

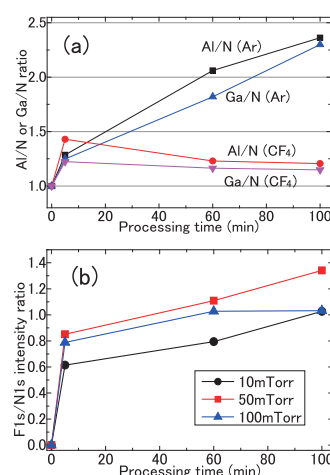


Fig. 2. Processing time dependence of the composition ratio of the surface etched by CF₄ and Ar plasmas at a gas pressure of 100 mTorr; (a) denotes the composition ratios Al/N and Ga/N, and (b) denotes the F/N ratio.

50 mTorr (not shown here). These results indicate that Ar plasma selectively etches N atoms from the AlGa_N surface. As shown in Fig. 2(b), the F/N ratio increased to about 1.3 with increased processing time.

Figure 3 shows the N-K NEXAFS spectra obtained by the TEY method of the AlGa_N surface etched at a gas pressure of 100 mTorr. Figure 3(a) shows the spectra etched by CF₄ plasma, and Fig. 3(b) shows the spectra etched by Ar plasma. As shown in Fig. 3(a), the peak shape of the sample surface etched by CF₄ plasma was broadened with increased processing time. This indicates that the crystalline structure of the AlGa_N surface was distorted. As shown in Fig. 3(b), the peak shape of Ar plasma was broadened more markedly than that of CF₄ plasma. This indicates that the crystalline structure etched by Ar plasma was more distorted than that of CF₄ plasma.

In TFY method, the peak shape of the sample bulk etched by both CF₄ and Ar plasmas was almost the same as that of the as-grown sample with increased processing time (not shown here). This indicates that the crystalline structure of the AlGa_N surface was undistorted in the deep region from the sample surface.

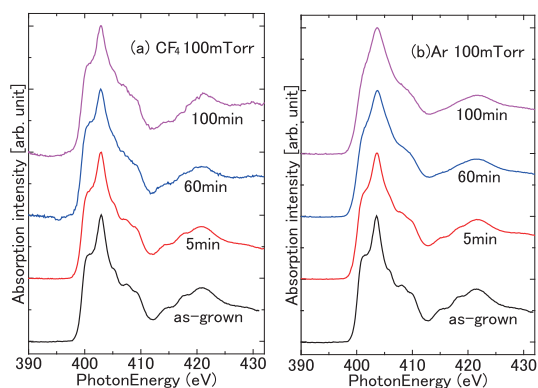


Fig. 3. N-K NEXAFS spectrum of the AlGa_N surface etched by (a) CF₄ and (b) Ar plasmas at a gas pressure of 100 mTorr, obtained by the TEY method at a soft X-ray incidence angle of 90° from the surface.

Discussion

By the measurements of XPS and NEXAFS, we found that the change in the surface composition and the disordering of the crystalline structure, which was not obtained by SEM observation, also occurred in CF₄ plasma etching. The surface composition and crystalline structure of the AlGa_N

etched by Ar plasma have changed more significantly than in the case of CF₄ plasma etching. Previously, we reported that the n-GaN surface roughness induced by He plasma etching was increased by UV light irradiation to n-GaN using a black light [10]. This should be because the bond between Ga-N atoms is weakened by UV irradiation. Therefore, in the same manner, Ar plasma should be etched selectively on the N atoms from the AlGa_N surface because the bond between the Ga-N and Al-N atoms was weakened by UV light irradiation from the Ar plasma. On the other hand, the main species of CF₄ plasma should be CF₃⁺ ions and F radicals [9]. In the AlGa_N surface etched by CF₄ plasma even for a short time, the formation of non-volatile fluorine compounds of Al(OH)_xF_y and GaF_x was suggested [6]. Suppression of the selective etching of N should be due to the formation of those fluorine compounds protecting the AlGa_N surface.

References

- [1] T. Katsuno, T. Manaka, T. Ishikawa, H. Ueda, T. Uesugi, and M. Iwamoto, *Appl. Phys. Lett.* **104**, 252112 (2014).
- [2] O. Ambacher et al., *J. Apply. Phys.* **85**, 3222 (1999).
- [3] H. Kambayashi, Y. Satoh, S. Ootomo, T. Kokawa, T. Nomura, S. Kato, and T. P. Chow, *Solid-State Electronics* **54**, 660–664 (2010).
- [4] Y. Cai, Y. Zhou, K. M. Lau, and K. J. Chen, *IEEE Trans Electron Devices* **53**, 2207–2215 (2006).
- [5] R. Kawakami, T. Inaoka, S. Minamoto, and Y. Kikuhara, *Thin Solid Films* **516**, 3478 (2008).
- [6] R. Kawakami, M. Niibe, Y. Nakano, T. Shirahama, S. Hirai, and T. Mukai, *Proc. International Symp. Dry Process (DPS2014)* P69–70 (2014).
- [7] C. D. Wagner, L. E. Davis, M. V. Zeller, J. A. Taylor, R. M. Raymond, and L. H. Gale, *Surf. Interface Anal* **3**, 211 (1981).
- [8] T. Kotaka, M. Niibe, and T. Mitamura, *Adv. X-ray Chem. Analysis, Jap.* **43**, 175–180 (2012).
- [9] R. Kawakami and T. Inaoka, *Vacuum* **83**, 490 (2008).
- [10] R. Kawakami, M. Niibe, Y. Nakano, T. Shirahama, K. Aoki, K. Oba, M. Takabatake, and T. Mukai, *Thin Solid Films* **81**, 570 (2014).

TEY-XAFS measurement for insulating sample

Takumi Yonemura¹, Junji Iihara¹, Shigeaki Uemura¹, Koji Yamaguchi¹, Masahito Niibe²
¹Sumitomo Electric Industries, Ltd., ²University of Hyogo

Abstract

XAFS measurement by total electron yield (TEY-XAFS) method is very useful for surface chemical state analysis. The biggest problem is how to suppress the charge-up. We have succeeded to obtain a TEY-XAFS spectrum of the insulating sample (BN) with depositing a gold stripe electrode.

Introduction

We can obtain surface-sensitive information by XAFS measurement with the total electron yield (TEY) mode. However, one of the biggest problems is the charge-up for the insulating plate sample.

The charge-up is a common problem with ordinary methods, such as scanning electron microscopy, auger electron spectroscopy and X-ray photoelectron spectroscopy. We applied some methods to suppress the charge-up of ordinary methods for TEY-XAFS measurement.

Experiments

The XAFS measurement was carried out at BL-09A [1] in the NewSUBARU SR facility. The incident X-ray photoemission current was obtained with an Au mesh electrode using an electrometer (Keithley 6514), and the sample current was obtained with another electrometer (Keithley 6517A).

We used hexagonal BN (h-BN) plate as the insulating sample. We tried some charge-up suppressing methods, such as (a) Os coating, (b) Pd-Pt coating, (c) metal mesh placement on it, and (d) a gold stripe electrode deposition. As a reference sample, we prepared h-BN powder on In sheet as sample (e), which is free for charge-up.

For the sample (d), the relation between the position of incident X-rays and the shape of XAFS was studied. The stripe electrode was 500 μm in width and 70 nm in thickness. We set the longer side of the X-ray beam and the stripe electrode to be parallel. Boron *K*-edge XAFS spectra and the sample current profile were obtained by each 40 μm interval to come across the stripe electrode. The X-ray energy was set to 225 eV, which was above the boron *K*-edge, in measurement of the sample current across the stripe coating.

Results

The TEY-XAFS results are shown in Fig.1. The efficient sample current was not obtained in Fig.1 (a) to (c). However, we found that the strip electrode coating method effectively suppressed

the charge-up in the TEY-XAFS measurement as shown in Fig. 1 (d).

In the Os or Pd-Pt coating method, these layers prevented the excited electrons from being emitted out from the sample's surface, and the sample current decreased. In the metal mesh placement method, the contact between the metal mesh and the sample surface was insufficient because they are not perfectly flat, therefore, charge-up occurred. As a result, TEY-XAFS spectra could not be obtained. On the other hand, the TEY-XAFS spectrum could be obtained for the powder sample because there was not the barricade like metal layer and the charge-up was suppressed because the electrical conduction region existed in the very neighborhood for the powder.

As a result, to obtain the TEY-XAFS spectrum, a bare region must exist on the insulating sample part and the electrical conduction region that is close to the sample part. Then, stripe electrode coating would be a suitable method because the sample has an electron emission region, which is close and in contact with the electrical conduction

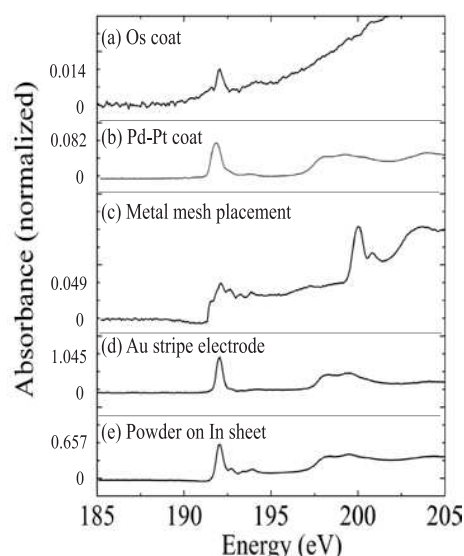


Fig.1 TEY-XAFS spectrum obtained with several charge-up suppression methods.

region. Therefore, the TEY-XAFS spectrum could be obtained as shown in Fig.1 (d).

Figure 2 shows the sample current of the h-BN plate with an Au stripe electrode on each X-ray position and the obtained XAFS spectrum. The regions in which the sample current was strong and stable correspond to those of the electrode positions. The width of the Au stripe electrode estimated from the sample current profile was approximately 470 μm , and which corresponds well to the designed width of the electrode, 500 μm . Figures 2 (I)-(V) shows boron *K*-edge TEY-XAFS spectra obtained at positions (I)-(V) in fig. 2, indicated by the red circles. TEY-XAFS spectra obtained at position (I) and (II) were good because the sample current was large and the noise current was relatively small. The TEY-XAFS spectrum

obtained at position (III) was rather poor because the sample current was half as much as those at position (I) and (II). TEY-XAFS spectra obtained at positions (IV) and (V) were bad because the sample currents were very small and the noise currents were relatively strong. In short, TEY-XAFS spectra were sufficiently obtained when the incident X-ray positions were at positions (I) and (II), which positions were nearer the stripe electrode.

References

[1] M. Niibe, M. Mukai, S. Miyamoto, Y. Shoji, S. Hashimoto, A. Ando, T. Tanaka, M. Miyai, and H. Kitamura, Synchrotron Radiation Instrumentation, AIP Conf. Proc. **705**, 576-579 (2004).

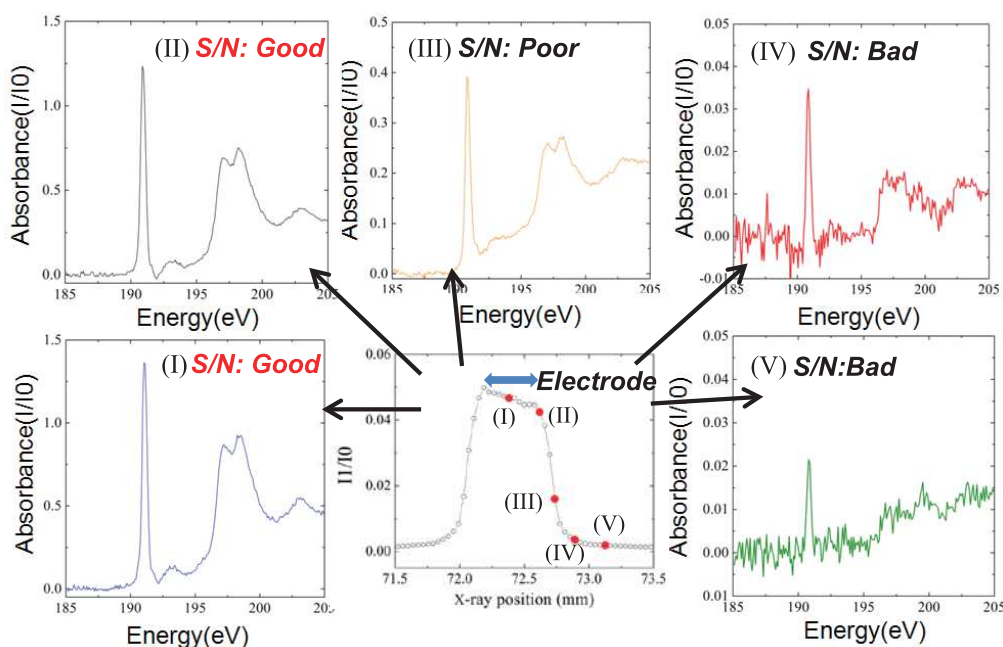


Fig.2 Sample current dependence to the X-ray positions and XAFS spectrum

Characterization of Small Phase Defects Using a Micro Coherent Extreme Ultraviolet Scatterometry Microscope

Tetsuo Harada¹, Yusuke Tanaka¹, Tsuyoshi Amano², Hiroo Kinoshita¹, Takeo Watanabe¹

1. LASTI, University of Hyogo

2. EUVL Infrastructure Development Center (EIDEC)

Abstract

To evaluate defects on extreme ultraviolet (EUV) masks at the blank state of manufacturing, we developed a micro coherent EUV scatterometry microscope (micro-CSM). The illumination source is coherent EUV light with a 230-nm focus diameter on the defect using a Fresnel zoneplate. This system directly observes the reflection and scattering intensities, which are strongly related to the printability of a defect. The scattering distributions of the 30-nm-wide defects were anisotropic due to interference with speckle from multilayer scattering. Thus, micro-CSM demonstrates that scattering distribution depends on the defect position in the multilayer.

Introduction

Extreme-ultraviolet (EUV), which is a next-generation lithographic technology based on light with a 13.5-nm wavelength, offers a significantly improved resolution compared to current systems, which have a wavelength limit of 193 nm. However, EUV poses a number of challenges. One of the most critical is the production of a defect-free mask. Because a mask, which consists of a glass substrate, a multilayer reflective coating, and absorber patterns, serves as the master pattern to fabricate semiconductor devices, mask defects result in device failure. Buried substrate defects (pits and bumps) and particles cause destructive interference and black spots on the photoresist because the multilayer reflects EUV light under the so-called Bragg conditions. For example, a shallow structure with a 1-nm depth and 100-nm width on the surface of a mask substrate can cause a 53°-reflection phase shift locally at the 13.5-nm EUV wavelength. And this localized phase structure causes destructive interference. Consequently, this buried structure is printable. Or, this structure changes line width of printed pattern.

We have developed micro coherent EUV scatterometry microscope (micro-CSM) to evaluate small phase defects.[1-2] Our micro-CSM is a very simple microscope based on coherent diffraction imaging (CDI). The sample phase defect is exposed by focused coherent EUV light, and the diffracted light is recorded using a CCD camera. Our group reported that the CDI system at EUV wavelength can achieve phase image of defects and pattern structures.[3-7] At previous work, it was performed that the phase defect size detection limits were approximately 25 nm in width and 1.4 nm in depth. An actual phase defect with a width of 90 nm and a height of 2.2 nm was also detected. The diffraction image was related to both the defect volume and the defect shape. The

defect position was also inspected via mapping image measurements composed of step-and-repeat observations.

EUV-phase distribution of phase defects on the mask is basic information necessary to predict defect printability because the distribution is used for defect compensation. In this paper, a micro-CSM is used to characterize small programmed phase defects with same design to characterize each defect. The evaluation includes analysis of the defect signal intensities and the multilayer scattering effect.

Experiments and Results

Figure 1 schematically depicts the micro-CSM system. The coherent EUV illumination was focused on the mask by a Fresnel zoneplate (FZP). The diameter of the on-axis FZP was approximately 300 μm , but the focusing layout of the FZP was off-axis in order to employ the reflection signal. A window allowed the reflected EUV light to be accepted. The designed focal length was approximately 750 μm . Half of the FZP region was patterned on the membrane, and the effective numerical aperture (NA) of the FZP was about 0.08. The angle of incidence of the main focused EUV ray was approximately 6.8°, which was similar to the angle of the EUV scanner of 6.0°. The expected focus size with the NA of 0.08 is 100 nm. The estimated focused size was about 230 nm, which was larger than the design. A CCD camera recorded diffraction due to defects.

The micro-CSM system was located on beamline 10 of the NewSUBARU synchrotron radiation facility. The diffraction signal from a defect was recorded using a back-illuminated CCD camera (Roper Scientific MTE-2048B). The CCD chip was parallel to the mask at a distance of approximately 50 mm. The NA of the micro-CSM system was approximately 0.27. The acceptance angle of the main ray was $\pm 16^\circ$, and the estimated

spatial resolution at half pitch was 30 nm.

Figures 2(a) and (b) show the micro-CSM images for the program defects with widths of 60 nm and 30 nm, respectively. These defects with 30-nm-wide are different from that of AFM results. The exposure times are 2 s and 5 s for 60-nm- and 30-nm-wide defect, respectively. The intensity denotes a linear scale where the images are shown as the differences from the no-defect position. Figure 3 shows the reflection and scattering intensities of each defect shown in Figs. 2(a) and (b). The horizontal axis indicates the reflection intensity integrated in the FZP pupil (R_n) and normalized by that of a no-defect position (R_0). The integrated region is less than 0.08 of the NA. The vertical axis indicates the integrated scattering intensity (S_n), which is also normalized by R_0 . The integrated region is the NA that ranges from 0.08 to 0.16. Each defect was observed via a step-and-repeat measurement. We estimated these reflection (R_n/R_0) and scattering intensities (S_n/R_0) as the defect signal (Fig. 3). Repeatability of the scattering signals (S_n/R_0) is approximately 5%. The signal intensity is sensitive to the focus, illumination position and illumination intensity. The bottleneck of the repeatability is precision of the illumination position. The illumination intensity has Gaussian distribution, and the defect should be illuminated on the illumination center. Smaller step distance is needed to achieve higher repeatability.

At the result of the 60-nm-wide defects in Fig. 3, the reflection intensities (R_n/R_0) at the defect positions are 4–6% lower than that at the no-defect position. The scattering intensities (S_n/R_0) are 2–3% of the reflection intensity, which are related to the reflection intensity (R_n/R_0). The dotted line in Fig. 3 is the fitting result of both designs with linearization, demonstrating that the reflection and scattering intensities are linearly related. The defect signals of the 60-nm-wide and 30-nm-wide result are well fitted. In addition, the signal variations in the same defect design indicated the variation of the effective defect size, which is equivalent to the EUV printability of the defect. The standard deviations of the scattering signals (S_n/R_0) from the average in the same defect design are 9% and 15% (1σ) for 60-nm- and 30-nm-wide defects, respectively. The deviation of 30-nm-wide defect is larger than that of 60-nm-wide defect. However, a large defect with a 60-nm width also has a larger deviation of 9%. It is noted that the small difference in the defect shape on the substrate causes large differences in the EUV defect signal with both 30-nm-wide and 60-nm-wide defects. The micro-CSM system directly observes the reflection and scattering intensities that are

strongly related to printability.

The diffraction distributions from a 30-nm-wide programmed defect are anisotropic. For example, the diffraction signal of #14 is localized to the upper right region. We assume this anisotropic distribution is due to speckle from the multilayer. To analyze the origin of the anisotropic distribution, we observed the several no-defect positions. A 50-s exposure time was used to record the weak multilayer scattering. Figures 4(a) and (b) show the observation results on a 30-nm-wide defect and a no-defect position, respectively, where the images are the differences from the diffraction image at another no-defect position. The center ring in Fig 4(a) shows residual edge in the subtraction process. The constructive and destructive interference conditions are shown in the Fig. 4. At the no-defect positions, the diffraction images have different anisotropic distributions, but have the same structure sizes of the anisotropic distributions. The structure size of interference conditions was about 100 – 200 nm, because the scale bar shown in Fig. 4 indicate $4\ \mu\text{m}^{-1}$ (250 nm). This structure size was very larger than the defect shape of 30-nm width. Thus, the diffraction signal in Fig. 4(b) shows speckle from roughness of the Mo/Si multilayer. The speckle structure is same as the anisotropic distribution of 30-nm wide defect. Therefore the anisotropic distribution is not due to the defect shape, but due to the interference with speckle from the multilayer scattering. Scattering from the multilayer depends on the mask position. Therefore, the speckle structure is depends on the position. At the 30-nm-wide defect, speckle structure will change the integrated reflection and scattering intensities. For example, the diffraction signal in Fig. 4(a) is localized to the upper left and lower right regions. At the EUV exposure tool, the captured scattering intensity by the optics would depends on the multilayer position under the coherent illumination condition. The defect position on the mask is important because the interference condition and the anisotropic scattering distribution can alter the defect printability. The anisotropic scattering distribution would be a part of reason why a small defect in the 30-nm-wide design causes a larger deviation in the defect signal.

We developed micro-CSM system with FZP focusing optics, which is a simple microscope based on CDI method, to evaluate defects on EUV masks. This system directly observes reflection and scattering intensities that are strongly related to printability. Observations of programmed phase defects with design depths of 1 nm and widths of 60 nm indicate that the reflection and scattering intensities denote the variation in defect size. Additionally, the scattering distributions of the

30-nm-wide defects were anisotropic due to interference with speckle from multilayer scattering. And the speckle structure depends on the mask position. These results demonstrate the high capability of this micro-CSM system for small phase defect characterization.

Acknowledgments

This work is re-contracted research from the EUVL Infrastructure Development Center (EIDEC). EIDEC programs are supported by the New Energy and Industrial Technology Development Organization (NEDO).

References

- [1] T. Harada, M. Nakasuji, A. Tokimasa, T. Watanabe, Y. Usui, and H. Kinoshita: Jpn. J. Appl. Phys. 51 (2012) 06FB08.
- [2] T. Harada, Y. Tanaka, T. Watanabe, H. Kinoshita, Y. Usui, and T. Amano: J. Vac. Sci. Technol. B 31 (2013) 06F605.
- [3] T. Harada, J. Kishimoto, T. Watanabe, H. Kinoshita, and D. G. Lee: J. Vac. Sci. Technol. B 27 (2009) 3203.
- [4] T. Harada, M. Nakasuji, T. Kimura, T. Watanabe, H. Kinoshita, and Y. Nagata: J. Vac. Sci. Technol. B 29 (2011) 06F503.
- [5] M. Nakasuji, A. Tokimasa, T. Harada, Y. Nagata, T. Watanabe, K. Midorikawa, and H. Kinoshita: Jpn. J. Appl. Phys. 51 (2012) 06FB09.
- [6] T. Harada, M. Nakasuji, T. Kimura, Y. Nagata, T. Watanabe, and H. Kinoshita: Proc. SPIE 8081 (2011) 80810K.
- [7] T. Harada, M. Nakasuji, Y. Nagata, T. Watanabe, H. Kinoshita: Proc. SPIE 8701 (2013) 870119.

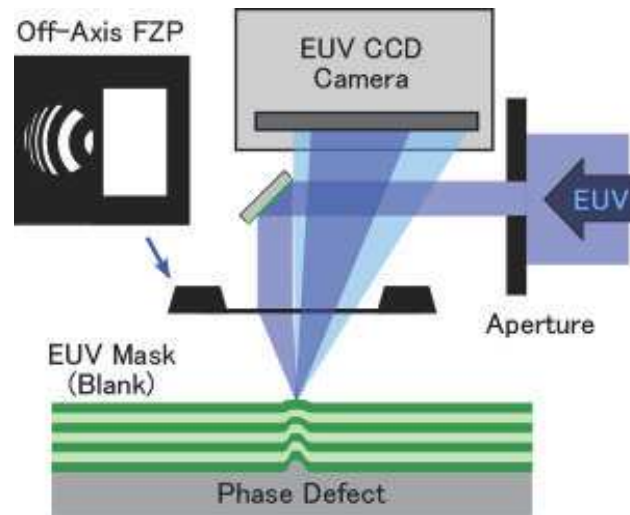


Fig. 1. Schematic diagram of the micro-CSM system. EUV illumination light is focused by the off-axis FZP. Diffraction from the defects is recorded directly by the CCD camera.

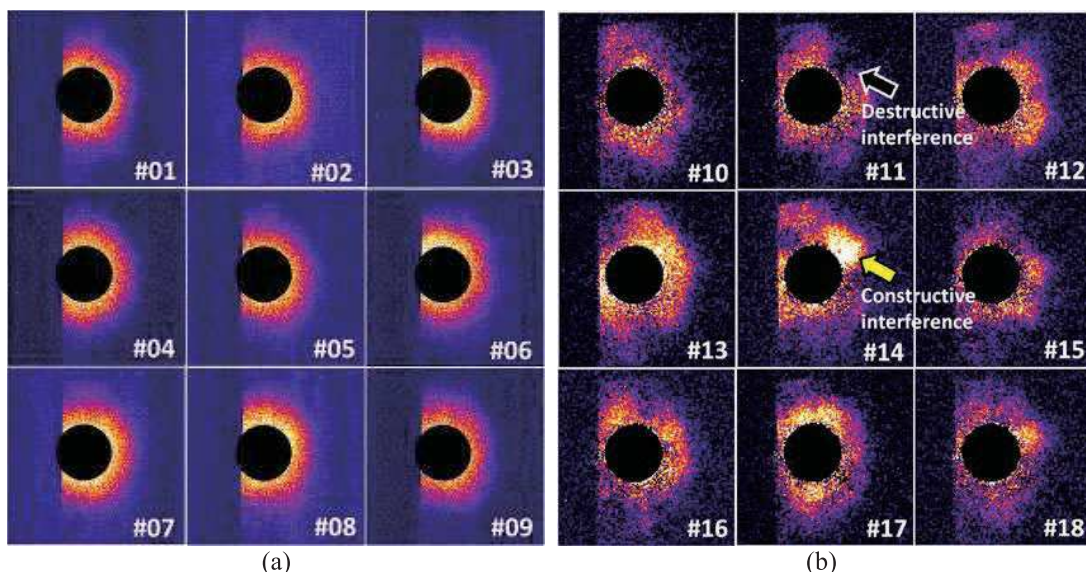


Fig. 2 Micro-CSM images of the nine program defects with (a) a 60-nm width and (b) a 30-nm width.

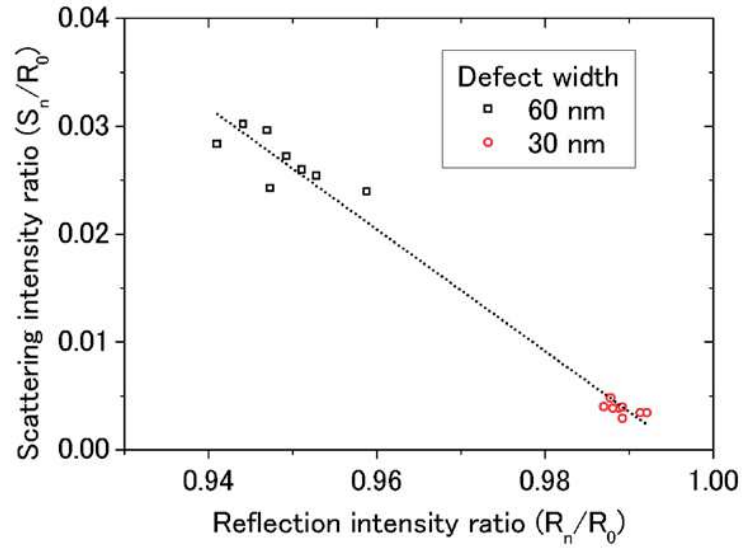


Fig. 3. Plot of reflection and scattering intensities of each defect shown in Figs. 5 and 6. Defect signals have a linear relationship.

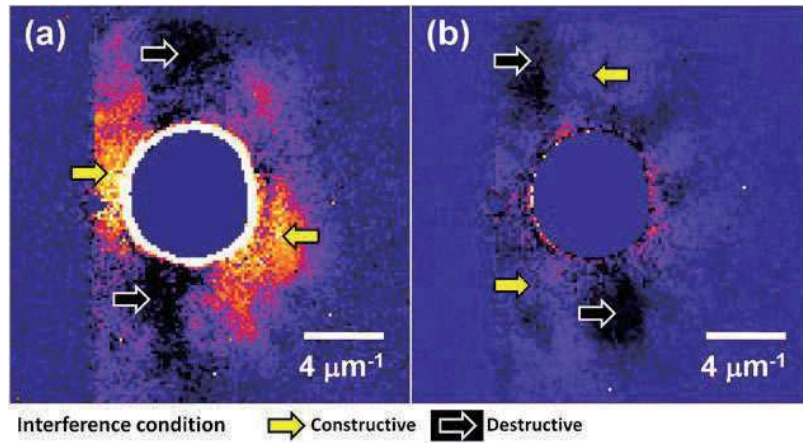


Fig. 4. Micro-CSM images with a long exposure time (50 s). Observation points are on (a) a 30-nm-wide defect and (b) no-defect position. The anisotropic scattering distributions are very similar due to multilayer scattering.

Surface-enhanced Raman Spectroscopy using a coffee-ring silver nanostructure

R. Hara, T. Fukuoka, R. Takahashi, Y. Utsumi and A. Yamaguchi
Laboratory of Advanced Science and Technology for Industry,
University of Hyogo 3-1-2 Koto, Kamigori, Hyogo 678-1205, JAPAN

II

Abstract

We have demonstrated a highly sensitive surface enhanced Raman scattering (SERS) sensing of 4,4'-bipyridine (4bpy) fabricated from the self-assembly of coffee-ring-type three dimensional silver nanostructure (Ag3D). A mixed solution of silver nanoparticles and polystyrene latex beads was deposited onto the glass substrate and spontaneously formed into the Ag3D. The mechanism of the formation of the Ag3D can be explained by the competition among a radial flow, a Marangoni recirculating flow, DLVO interactions and sedimentation. Typical spectra of 4bpy were observed within 1 min of dropping 4 bpy. By optimizing the Ag3D preparation conditions, we could observe the characteristic SERS spectrum of 1nM 4bpy solution. After the chloride activation of the Ag3D, we found that Ag crystal growth occurred by high-resolved scanning electron microscopy. This result is attributable to the re-crystallization due to the oxidative etching process. The enhancement of SERS spectra after the chloride activation could also be induced by the local surface enhanced plasmon resonance shift due to the enlargement of Ag nanoparticles within the Ag3D. Thus, our SERS sensor using Ag3D also presents it is advantageous as it is stable with the passage of time. [RSC Advances **5**, 1378-1384 (2014).]

Introduction

Recently, the development of microfluidic devices for various applications, including point-of-care medical diagnostics and environmental and food analyses, has been actively pursued.¹⁻³ An easily operable analytical method for detecting and identifying small amounts of analyte in microfluidic devices is required. Fluorescence method and absorption spectrometry, which are commonly used to analyze chemical species—including small organic molecules, inorganic ions, proteins and even whole organisms such as bacteria and viruses—are not suitable to meet this requirement; this is because these analytical techniques do not provide a sufficient optical path length in the microchannel. Therefore, a novel detection technique is needed to replace the conventional methods.

Surface-enhanced Raman scattering (SERS) has been attracting attention as a highly sensitive analysis technique;⁴⁻⁸ it uses Raman spectroscopy and localized surface plasmon resonance (LSPR). A noble metal nanostructure using gold or silver is essential to achieve strong LSPR. Gold nanoparticles (NPs) have often been used to fabricate these nanostructures, because gold NPs do not relatively react with other substances and are easy to use. Therefore, well-established methods for preparing stable colloidal solutions of gold NPs in both polar and nonpolar solvents have been developed. However, because of the higher electrical conductivity of silver, it has a better SERS activity than gold.⁹⁻¹⁷ Furthermore, silver

has a higher reactivity with other substances. Therefore, three-dimensional silver nanostructures, such as porous and nanoshell, are considered suitable for SERS measurements of various compounds.^{16, 17} The Ag nanostructures can be applied in biotechnology, such as in the analysis of proteins. However, fabrication of the Ag nanostructures is difficult because of the high reactivity of the surface of Ag NPs.

In this study, we achieved the fabrication of a novel sterically bulky three-dimensional Ag nanostructure (Ag3D) by optimizing the preparation conditions. We described the mechanism of Ag3D formation considering the competition among four contributions: a radial flow driven by evaporation at the wetting line, a Marangoni recirculating flow driven by surface tension gradients, the transport of particles toward the substrate driven by Derjaguin, Landau, Verwey and Overbeek (DLVO) interactions and sedimentation (gravitation) force. We succeeded in observing chloride activation, which was aided with the two- to three-fold increase in the intensity of the Raman spectrum on addition of NaCl solution to Ag3D. Our experimental observation could be explained by the re-crystallization induced by the oxidative etching process.

Experiments and Results

Ag3D was prepared using convective self-assembly¹⁸⁻²², namely the coffee-ring effect. Polystyrene beads (PS) of diameter 600 nm were

concentrated by centrifugation and washed to yield a 10 % w/v suspension. Aqueous suspensions of Ag colloidal nanoparticles (AgNPs) of diameter 40 nm were synthesized using a standard citrate reduction protocol, Lee-Meisel method.²³

A silicone sheet with f6 mm though hole was put onto an ultraviolet-cleaned glass slide was made. 5 μ L of the mixed solution of AgNPs and PS was dropped into the well and dried at 75% relative humidity for about a day. A PS colloidal crystal was fabricated by convective self-assembly, where AgNPs were simultaneously accumulated in the PS gaps, as shown in Fig. 1(a). The physical and chemical mechanism of forming structure can be explained by competition among three flow patterns: a radial flow driven by evaporation at the wetting line, a Maragoni recirculating flow driven by surface tension gradients, and transport of particles toward the substrate driven by DLVO interactions and sedimentation force.

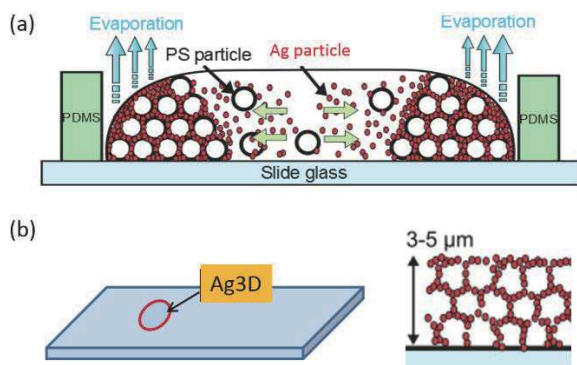


Figure 1 (a) Fabrication of Ag3D using convective self-assembly. (b) Schematic of cross-section of Ag3D after drying and soaking in dichloromethane.

Figure 2 (a) shows the optical micrograph of the prepared Ag3D structure. We confirmed that the fabricated outward form was similar to the coffee-ring structure. Figure 2(b) shows a scanning electron microscope (SEM) image of the circumferential location of the coffee-ring. The Ag3D structure width was ~ 20 μ m in the radial direction. As shown in Figure 2(b), there are many pores along the wall of the coffee-ring. A magnified SEM image revealed the existence of a unique honeycomb-like structure in Ag3D, which was fabricated at the edge of the coffee-ring. The relatively periodically-patterned porous layers pile up high. The frames are consisting of the silver nanoparticles and sustaining the pores after removing the PS particles as shown in Figure 2(b). The high-resolution SEM image shown in Figure 2(b) reveals that the AgNPs are not monodisperse and the size dispersion is expected to in the range from about 30 to 100 nm. Although the diameter of

the PS was 600 nm, the average diameter of the pores observed in the uppermost layer—made by removing the PS particles—was 499 ± 70 nm (average and standard deviation were evaluated from 117 pores). This is attributable to shrinking of the porous structure in order to maintain the overall stability of the Ag3D structure.¹⁸⁻²¹ As a result, there are a lot of nano-scale gaps between AgNPs in the Ag3D structure. The nano-scale gaps within higher order nano-scale architecture of the Ag3D could offer the SERS-active hot spots. The higher order architecture is in good agreement with the cartoon illustrated in Figure 1(b). The laser for Raman spectroscopy could be focused easily because of the sufficient width and sterically bulky of the Ag3D.

We demonstrated *in situ* SERS measurement of 4,4'-Bipyridine (4bpy) as the Raman active molecule using the prepared Ag3D. A cover glass was used to prevent the 4bpy solution from drying and to maintain its concentration. The Ag3D was placed in the Raman spectrometer (RAM-100S, Lambda Vision Inc.), and a 1 s irradiation of

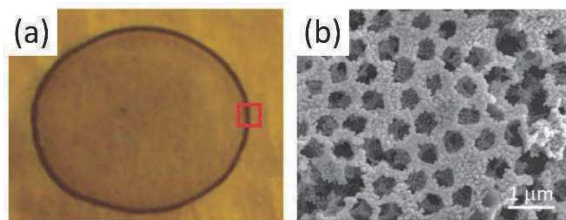


Figure 2 (a) Optical micrograph of Ag3D fabricated using the coffee-ring effect. The outermost shell corresponds to the coffee-ring. (b) Highly magnified SEM image of Ag3D in the red square area of (a).

wavelength 785 nm (laser power, 50 mW) laser focused on the Ag3D. As shown in Fig. 3, we observed the characteristic enhanced Raman spectrum of 4bpy (1000 cm^{-1} , 1250 cm^{-1} , 1580 cm^{-1}) within 1 min of dropping 4bpy. The SERS spectrum was observed only in the part of Ag3D; no spectrum was observed in the part without Ag3D.

To enhance the SERS spectra obtained using the Ag3D, chloride activation,^{11,12} which enhanced the Raman intensity of 4bpy by a factor of two to three, was performed as follows. After 35 μ L of 4bpy aqueous solution was dropped into a well on the Ag3D, 2 μ L of NaCl (50 mM) was added to the Ag3D. SERS spectra of 100 μ M 4bpy aqueous solution were easily observed by adding an aqueous solution of sodium chloride. Characteristic enhanced Raman peaks attributed to 4bpy (located at 1000 , 1250 and 1580 cm^{-1}) were observed. Figure 3(a) shows the SERS spectra of 4bpy before and after chloride activation. The blue and brown

solid lines correspond to the SERS spectra of 100 μM 4bpy before and after chloride activation, respectively. The black dotted line represents the SERS spectrum of the blank. As evident from Fig. 3, chloride activation enabled us to increase the intensity of the SERS spectra.

To understand the mechanism of chloride activation, we compared the SEM images of Ag3D before and after adding the NaCl solution. As a result, we found that Ag crystal growth occurred after the application of NaCl solution as shown in Fig. 3(b). This result indicates that the recrystallization was also induced in the Ag3D. This re-crystallization is attributable to the oxidative etching process investigated by Wiley *et al.*²⁴ According to Wiley *et al.*²⁴, the defects inherent in twinned nuclei of silver led to their selective etching and dissolution by chloride and oxygen from air, leaving the single-crystals to grow. Therefore, by the same token in the experimental results by Pucek *et al.*^{25, 26}, the addition of the concentrated solution of chloride ions induced a rapid-crystallization process towards larger silver crystals providing an enhancement of SERS signals with excitation in 785 nm wavelength region in our experiment.

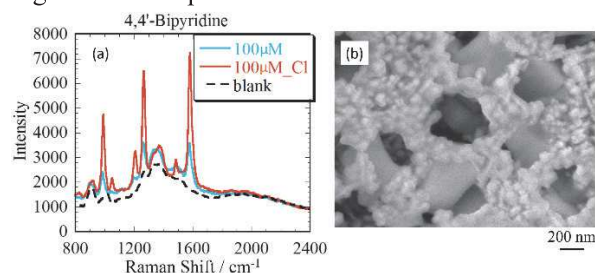


Figure 3(a) SERS spectra of 4bpy with and without the aqueous solution of sodium chloride. The concentration of 4bpy is 100 μM . (b) Highly magnified SEM images of Ag3D after adding the aqueous solution of sodium chloride, respectively.

Conclusion

We fabricated a novel sterically bulky three-dimensional silver nanostructure and demonstrated SERS measurements. The essence of Ag3D formation process can be explained by the competition among four contributions: a radial flow, a Marangoni recirculating flow, the transport of particles toward the substrate driven by DLVO interactions and sedimentation force. The Ag3D easily enabled detection of 1 nM 4bpy through the SERS spectrum. The observed Raman spectra in the Ag3D were enhanced about 10^5 times compared with the case without Ag3D. Thus, highly sensitive SERS measurements was achieved using Ag3D. Using chloride activation, the possibility of further development for SERS measurements using Ag3D was demonstrated. We

found that the enhancement of SERS spectra could also be induced by the LSPR shift due to the re-crystallization of Ag within the Ag3D. Finally, we proved by SERS measurements that Ag3D is advantageous as it is stable with the passage of time.

References

- [1] D. Mark, S. Haeberle, G. Roth, F. von Stetten R. Zengerle, *Chem. Soc. Rev.* 2010, **39**, 1153.
- [2] P. Yager, T. Edwards, E. Fu, K. Helton, K. Nelson, M. R. Tam, B. H. Weigl, *Nature*, 2006, **442**, 412.
- [3] M. Miro, E. H. Hansen, *Anal. Chim. Acta.*, 2007, **600**, 46.
- [4] C. L. Haynes, A. D. McFarland, R. P. Van Duyne, *Anal. Chem.*, 2005, **77**, 338 A.
- [5] M. G. Albrecht, J. A. Creighton, *J. Am. Chem. Soc.*, 1977, **99**, 5215.
- [6] D. L. Jeanmaire, R. P. Van Duyne, *J. Electroanal. Chem.*, 1977, **84**, 1.
- [7] F. Ni, R. Sheng, T. M. Cotton, *Anal. Chem.*, 1990, **62**, 1958.
- [8] S. M. Nie, S. R. Emory, *Science*, 1997, **275**, 1102.
- [9] K. Kneipp, Y. Wang, H. Kneipp, L. T. Perelman, I. Itzkan, R. Dasari, M. S. Feld, *Phys. Rev. Lett.*, 1997, **78**, 1667.
- [10] P. Hildebrandt, M. Stockburger, *J. Phys. Chem.*, 1984, **88**, 5935.
- [11] W. E. Doering, S. Nie, *J. Phys. Chem. B*, 2002, **106**, 311.
- [12] S. Habuchi, M. Cotlet, R. Gronheid, G. Dirix, J. Michiels, J. Vanderleyden, F. C. De Schryver, J. Hofkens, *J. Am. Chem. Soc.* 2003, **125**, 8446.
- [13] S. L. Kleinman, E. Ringe. N. Valley, K. L. Wustholz, E. Phillips, K. A. Scheidt, G. C. Schatz, R. P. Van Duyne, *J. Am. Chem. Soc.*, 2011, **133**, 4115.
- [14] M. P. Cecchini, V. A. Turek, J. Paget, A. A. Kornyshev, J. B. Edel, *Nat. Mater.* 2013, **12**, 165.
- [15] L. Su, W. Jia, D. P. Manuzzi, L. Zhang, X. Li, Z. Gu, Y. Lei, *RSC Adv.* 2012, **2**, 1439.
- [16] S. A-. Jradi, S. Jradi, J. Plain, P. -M. Adam, J. -L. Bijeon, P. Royer, R. Bachelot, *RSC Adv.* **2**, 2012, 7837.
- [17] J. B. Jackson, S. L. Westcott, L. R. Hirsh, J. L. West, N. J. Halas, *Appl. Phys. Lett.* 2003, **82**, 257.
- [18] D. M. Kuncicky, B. G. Prevo and O. D. Velve, *J. Mater. Chem.*, 2006, **16**, 1207.
- [19] Y. Mori, N. Shinohara, and T. Fukuoka, in International Workshop on Nanomechanical Cantilever Sensors 2008 (Mainz, Germany, 19 May 2008).
- [20] R. Takahashi, T. Fukuoka, Y. Utsumi, A. Yamaguchi, *Jpn. J. Appl. Phys.*, 2013, **52**, 06GK12.

- [21] T. Fukuoka, D. Fukuoka, Y. Mori, and Y. Utsumi, *IEEJ Trans. EIS.*, 2010, **130**, 1806; T. Fukuoka *et al.*, to be published.
- [22] R. Bhardwaj, X. Fang, P. Somasundaran, D. Attinger *Langmuir*, 2010, **26**, 7833.
- [23] P. C. Lee and D. Meisel, *J. Phys. Chem.*, 1982, **86**, 3391.
- [24] B. Wiley, T. Herricks, Y. Sun and Y. Xia, *Nano Lett.*, 2004, **4**, 1733.
- [25] R. Prucek, A. Panáček, A. Fargašová, V. Ranc, V. Mašek, L. Kvítek and R. Zbořil, *CrystEngComm.*, 2011, **13**, 2242.
- [26] R. Prucek, A. Panáček, J. Soukupová, R. Novotny and L. Kvítek, *J. Mater. Chem.*, 2011, **21**, 6416.

Fabrication and Evaluation of Dihedral Corner Reflector Array fabricated by X-ray lithography

T. Yamane¹, S. Maekawa², Y. Utsumi¹, I. Okada³ and A. Yamaguchi¹

¹Laboratory of Advanced Science and Technology for Industry, University of Hyogo, JAPAN

²Parity Innovations co ltd., JAPAN

³Synchrotron Radiation Research Center, Nagoya University, JAPAN

Abstract

We propose a new imaging optics called Dihedral Corner Reflector Array (DCRA) which is designed to make the floating image. DCRA consists of numerous micro-mirrors placed perpendicular to the surface of substrate. The micro-mirror array is implemented by the inner walls of minute square holes or the side of minute square pillar. We can choose two types of the structure. The primordial is based on two reflections by a pair of adjacent mutually perpendicular mirrors, *i.e.*, a dihedral corner reflector. Although the principal of operation is based on reflection by mirrors, the device is also transmissive and deflects light. Primordial of DCRA is not so complicated, However, it is too difficult to fabricate the DCRA by usual machining because of high aspect ratio micromachining and high mirror accuracy. Therefore, in this manuscript, we fabricated the device by deep X-ray lithography due to synchrotron radiation. The characteristics of the fabricated DCRA are evaluated by the optical transmission and reflection measurements.

Introduction

Displays which can display three-dimensional (3D) image have been attracting much attention as a device or method to directly appeal to eye. The development of these devices and systems has been actively pursued. [1] An easily operable device or system for floating 3D or 2D images is required for achieving medical imaging, mechanical computer-aided design, and military visualization. One of the earliest and simplest system for achieving the two-view 3D images is the color anaglyph in which a user views a color print or display encoding left and right views in two different color channels with a pair of colored filter glasses. There are many important approaches to 3D display.

Here, we consider another approach to realize 3D or floating image. There are some basic imaging optical systems that can form a real image, such as convex lens, a concave mirror, and diffraction optics (a Fresnel lens). [1] For example, there are systems that are based on the lens array of the Graded Index Lens (GRIN) [2], Roof Mirror Lens Array (RMLA) [3], and the stacking of various micro-lens arrays [4, 5]. These systems with the lens have an optical axis and a specific focal length. Moving an object closer to the optics, the real image forms farther from it and is magnified. In contrast, there are several imaging optical systems which can form 3D-images without distortion. One of the systems is a plane mirror. However, the plane mirror can only form virtual images.

In this manuscript, we propose a new imaging

optics forming a real mirror image with the use of micro-mirrors. We called this imaging optics dihedral corner reflector array (DCRA). There are

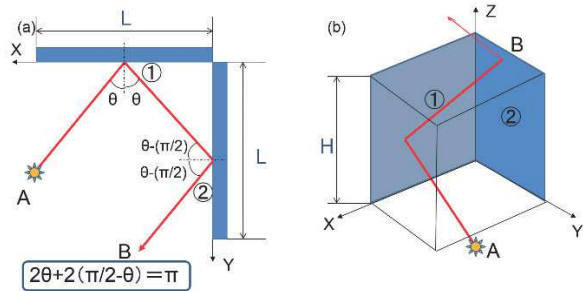


Figure 1 Optical ray trajectories shown in (a) overhead view and (b) projective space for transmission type dihedral corner reflector (DCR).

transmission and reflection type DCRA systems. Here, we fabricated the former type DCRA using deep X-ray lithography due to synchrotron Radiation. We evaluated the optical characteristics of manufactured DCRA and demonstrated the floating image.

Primordial of DCRA

DCRA is composed of arrays of dihedral corner reflector (DCR). Figure 1 describes the optical ray trajectories shown in (a) overhead view and projective space for transmission type DCR. The reflection mode of DCR is limited because incident light is reflected twice when passing through the DCR. In the case of two-dimension structure, an

incident light from a light source “A” is reflected in the direction “B” parallel to the light source “A” as shown in Fig. 1(a). Next, let us consider that the incident light from “A” into a dihedral corner reflector reflects two times at the mirrors and deflects toward the point “B” in 3D structure as shown in Fig. 1(b). In the transmission type DCR, the refractive body of DCR refracts the ray trajectory at positions of incidence and output. Then, if the micro-mirrors are extremely small, the incident light passes through the substrate plane toward the symmetric point for the light source. When we prepare many DCRs on the substrate, all the light from a light source is converged onto the reflection-symmetric point of the source. As a result, the array of numerous dihedral corner reflectors, namely DCRA, can realize the floating image.

Design of DCRA

Here, we postulate that the transmittance of DCRA is the percentage of incident light through the reflection-symmetric point. The transmittance is given by

$$\text{Transmittance} = I \times R^2 \times T, \quad (1)$$

where I is the ideal transmittance, R is reflectance of micro-mirror, and T is the losses, which is defined as the attenuation of intensity of the incident light after passing through the DCRA.

Reflectance R of micro-mirrors is the most important factor in imaging by DCRA. In this study, we expect that it is as close as possible to 100%. However, in the actual device, the micro-mirrors placed perpendicular to the surface of substrate. So, no one can be polished after manufactured because of the micro-scale perpendicularly precipitous pillar structure array. Accordingly, reflectance of micro-mirrors is determined during the creation of the DCRA.

The perpendicularity of DCR reflector plays the most important role in the resolution of the floating imaging, and it causes the distortion of the image. The dependence of the perpendicularity of the wall of DCRA have been able to be estimated by the optical simulation. In the simulation, we calculate that the optical ray trace through position of light reflected by a line of plane mirrors from point light. Then, we can choose the value of the number of the plane mirrors, the distance of point light to the head mirror and the taper of mirrors. If the planes of mirrors in the DCRA are exactly perpendicular, all the reflected light by each mirrors pass through the same position of the head mirror. The floating image produced by the DCRA can be estimated to be distorted up to 10 μm when the plane mirrors

have less than 1/60 degree taper.

Imaging resolution is dependent on the dimension of the DCR. The higher resolution image can be obtained, the smaller DCRs within the DCRA have to be fabricated. However, the image produced by the DCRA costing of smaller DCRs will darken because the diffractive component of the light increases.

Therefore, deep micro-fabrication process with high precision should be required for manufacturing the DCRA. The deep X-ray lithography using synchrotron radiation is one of clues to achieve the DCRA which can produce the floating imaging with high quality and adequately brightness.

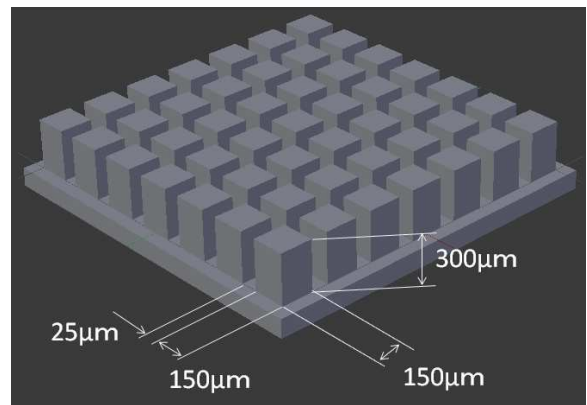


Figure 2. Schematic of fabricated DCRA.

Table.1 Dimension of DCRA

position	dimension
Pillar dimension[μm]	150
Pillar height [μm]	300
Pitch[μm]	25
Ideal transmittance[%]	100
Aperture ratio[%]	64.9
Perpendicularity[deg]	90
Roughness[nm]	10

Fabrication of DCRA using deep x-ray lithography

Polishing the micro-mirrors is easy if they are parallel to the device surface. However, because to micro-mirrors are perpendicular to the device surface in the DCRA, it is impossible to polish them in pre- or post- processes. The micro-fabrication of high precision is required for the fabrication of DCRA. In this manuscript, we fabricated the pillar patterned DCRA made of Poly-methyl methacrylate (PMMA) by using synchrotron radiation. The fabrication process using the synchrotron radiation enables us to fabricate the

DCRA structure within the limit of accuracy of about 1 nm.[2] Figure 2 shows schematic of dimensions of our DCRA device. The dimension of fabricated DCRA are summarized in Table 1. Here, the pillar dimension means the dimension of DCR.

The incident light through inside of pillars made by PMMA in pillar patterned DCRA. Considering the PMMA refractive index, we design the aspect ratio (height/width) of our device is two in order to achieve that the theoretical value of light transmittance of our device is expected to be 100%. The aperture ratio, namely the portion of the opening, is determined by the pitch between the reflectors. We estimate the effective fraction transmitted of our device is 64.9% considering the contribution of the aperture ratio. Expressed in another way, the brightness of the floating image is expected to be 64.9% with the respect to that of an object. The dimension and desired values of DCRA are summarized in Table.1.

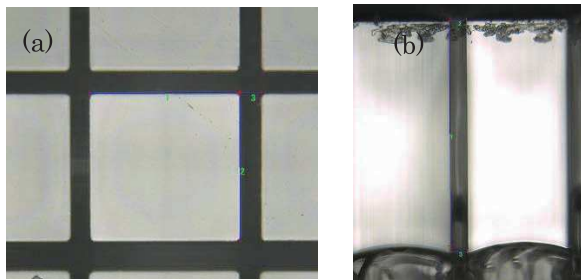


Figure 3. Optical microscope image of pillars for (a) top view and (b) cross-sectional view.

Table 2. dimension of manufactured DCRA

Pillar dimension [μm]	150.92
Pitch [μm]	151.42
Pillar height [μm]	25.87
Perpendicularity[minute]	326.78
	5.8

Results and discussion

Up to now, the criteria and evaluation method for the properties such as the resolution and brightness of the image produced by the DCRA have not yet been established. In this study, we evaluate the characteristics of the fabricated DCRA by measuring the dimension, the perpendicularity of the reflector, fractional transmitted and reflection. The attenuation of brightness and reflection ratio are measured by transmission-reflection ratio measuring instrument.

First, we checked the dimension of the fabricated DCRA. Figure 3 shows an image of micro-pillars by optical microscope, and the dimensions of each section are summarized in Table 2. These values

are in almost good agreement with our designed dimensions. However, the perpendicularity of pillars have about 6 minute taper, it seems that cause the distortion at $65 \mu\text{m}$ for the distance of light source to the device. This distortion is



Figure 4. Floating image formed by the DCRA fabricated by X-ray lithography process using synchrotron radiation facility BL-2 at NEWSUBARU.

expected to be serious about the observation of floating image made by DCRA.

The attenuation of brightness has been evaluated by the transmission-reflection ratio measuring instrument. Accordingly to the measurement result [6], the real transmittance is calculated 5.4% by Equation (1). This result is expected to be imaged a dark floating image using our fabricated DCRA.

In addition, the reflection ratio is evaluated by using same measuring instrument. We found the reflection mode of the fabricated DCRA is in good agreement with our desired behavior. However, the broad reflection peak appeared because the reflection light is spread by the diffuse reflection, stained PMMA and distortion from the taper structure. Therefore, we will have to improve the measuring method for reflection ratio in future.

We demonstrate the formation of floating image using the fabricated DCRA. As shown in Fig. 4, we can produce the floating image indeed, although the dark image is formed.

Summary

We proposed novel imaging optics with micro-dihedral corner reflector arrays called DCRA in this paper, which can form a reflection-symmetric image as a real image in the air. We can form a floating image by using the DCRA fabricated by synchrotron radiation.

Our main work to improve imaging in the future is to increase transmittance and establish the quantitative measure method of resolution and

reflection ratio.

References

- [1] N. S. Holliman, N. A. Dodgson, G. E. Favalora and L. Pockett, IEEE Trans. Broadcast. **57**, 362 (2011).
- [1] S.Maekawa. “Transmissive Optical Imagin Device with micromirror Array” The international society for Optical Engineering, Vol. **6392**, 63920E-1, (2006).
- [2] H.Kita, I.Kitano, T.Uchida, and M.Furukawa, “Light-focusing glass fibers and rods,” Journal of the American Ceramic Society **54**, pp. 321-326, (1971).
- [3] M.Kawazu and T.Inokuchi, “Imaging Device using a roof micro lens array,” Applied Optics **24**(24), pp.4300-4306, (1985).
- [4] R.Volkel, H.Herzig, P.Nussbaum, and R.Dandliker, “Microlens array imaging system for photolithography,” Optical Engineering **35**(11), pp.3323-3330, (1996).
- [5] M.Ishikawa, “A proposal to create the impression of a miniature garden, and the development of a glasses-free small 3d display”, Pioneer R&D **12**(3), pp.47-58, (2003). [In Japanese]
- [6] A. Yamaguchi, S. Maekawa, T. Yamane, I. Okada and Y. Utsumi, submitting.

Surface Acoustic Wave Feeder with Triangular Guide Walls for Micro Powder

Tsunemasa Saiki^{a,b}, Yuya Matsui^b, Masahiro Takeo^b, Kazusuke Maenaka^b,
Akinobu Yamaguchi^b, and Yuichi Utsumi^b

^a Hyogo Prefectural Institute of Technology, ^b University of Hyogo

Abstract

We propose a novel surface acoustic wave (SAW) feeder with a unique powder transport path that consists of two triangular guide walls on a piezoelectric substrate. In the experiment, by the guide walls, the micro powder was gradually collected during transport to the downstream side of the SAW until the powder particles arrived at the substrate edge one after the other, and gradually fell down through the narrow part between the guide walls. This demonstrates that arranging the guide walls in the SAW feeder can improve the supply accuracy of tiny amounts of micro powder.

Introduction

Recently in the electronics industry, physical operations such as the transportation and separation of micro metal powders are required. However, it is difficult to handle powders with accuracy because they can behave not only as a solid but also as a liquid or gas. Therefore, in many industrial plants, powder must be handled using conventional experimental rules. This conventional approach makes it impossible to transport a tiny amount (from several hundred μg to several mg) of dry powder having a diameter of several dozen micrometers or less if a general-purpose conveyor or blower that has been miniaturized is used. An ultrasonic wave device could be used to transport tiny amounts of micro powder [1], but since such a device consists of piezoelectric multilayers, its manufacturing process is complicated. We have therefore focused on a surface acoustic wave (SAW) device with a simple structure and easy fabrication and have been studying powder transportation actuators that have multi-functionality [2]. In this paper, we propose a novel SAW feeder with a unique powder transport path and discuss its performance.

Fabricated SAW feeder

The proposed SAW feeder consists of one interdigital transducer (IDT) and two triangular guide walls (Fig. 1). The IDT has 20 electrode pairs, a pitch size of $400\text{ }\mu\text{m}$, and an aperture width of 5 mm , while the guide wall, located at an inclination angle of 5° against the central axis of the IDT, has a length of 35 mm and a minimum $300\text{-}\mu\text{m}$ interval between walls. The IDT and the guide walls are made of a $1\text{-}\mu\text{m}$ Al layer and were simultaneously fabricated on a piezoelectric wafer (127.8-degree y-rotated x-propagating LiNbO_3) by one photolithography process at a time. Incidentally, because the height of the guide wall, i.e., the thickness of the Al layer, was one-tenth of the

powder particle size, which was approximately $10\text{ }\mu\text{m}$, it was difficult for the powder to climb on the guide wall. Moreover, in the case of the thickness, the SAW cannot appear on the surface of the Al layer. Therefore, even if the powder could climb on the guide wall, it would not be able to be transported. The proposed SAW feeder does not require anything like a micro funnel in order to amass powder on the guide walls that possess these features, so we do not need to consider problems unique to the micro funnel such as rat-holing and arching.

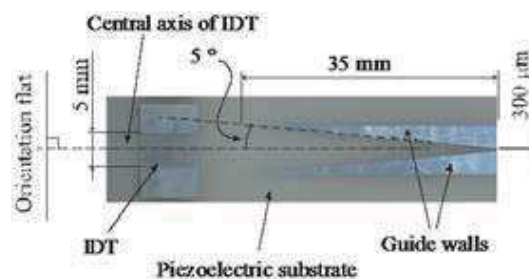


Fig. 1 Fabricated SAW feeder for micro powders.

Experiment

Our experimental setup for transporting powders by the SAW feeder is shown in Fig. 2. In the experiment, a function generator created 1-kHz burst waveforms consisting of 2000 cycles of 31.6-MHz sine waves and an amplifier boosted the burst waveform voltage. When the boosted voltage was applied to the IDT of the SAW feeder, a SAW was generated. Here, the electric power applied to the IDT was 630 mW. The SAW propagated on the surface of a piezoelectric substrate and arrived at the 30-mg deposit of copper powder that was located 10 mm from the IDT. The powder was then transported to the opposite side of the IDT by the SAW and collected by the guide walls. Finally, the powder arrived at the edge of the substrate and fell

7 mm down to the top plate of an electronic scale. The powder transportation was recorded with a high-definition video camera and the powder weight on the top plate was measured by the electronic scale.

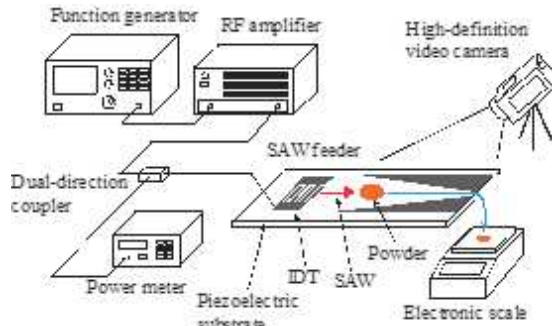
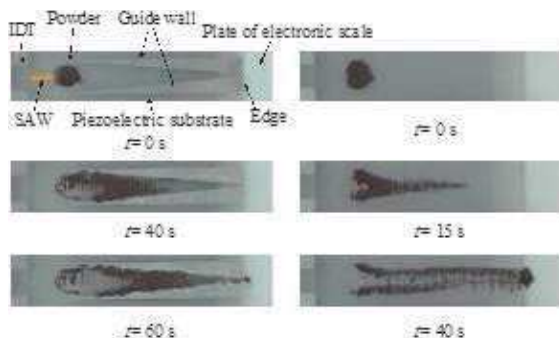


Fig. 2 Experimental setup for transporting powders by SAW feeder.

Results

Powder transportation using the SAW feeders with and without guide walls is shown in Fig. 3 (a) and (b), respectively, where t represents the elapsed time after applying the electric power to the IDT. When the SAW feeder with the guide walls was used, the powder was gradually collected during transport to the opposite side of the IDT until the powder particles arrived at the substrate edge one after the other and fell down through the narrow part between the guide walls. In contrast, when the SAW feeder without the guide walls was used, the powder was transported in the same direction and then fell down through a wide part whose distance was about the same size as the IDT's aperture. These results demonstrate that, by arranging the guide walls, powder can be accurately poured down a target point.



(a) With guide walls (b) Without guide walls
Fig. 3 Powder transportations by SAW feeders.

Temporal changes to the weight of the powder supplied by the SAW feeders are shown in Fig. 4. The weight of the powder supplied by the SAW feeder with guide walls increased gradually with elapsed time while that without guide walls in-

creased rapidly. This demonstrates that arranging the guide walls in the SAW feeder can improve the supply accuracy of tiny amounts of micro powder.

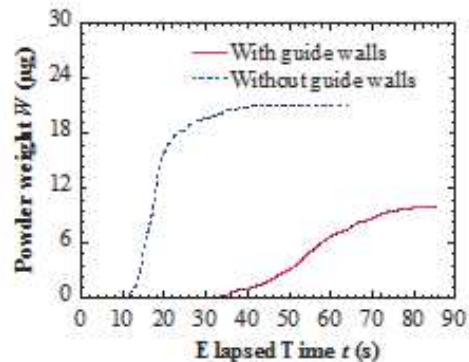


Fig. 4 Temporal changes of supplied powder weights

References

- [1] M. Mracek and J. Wallaschek, "A System for Powder Transport Based on Piezoelectrically Excited Ultrasonic Progressive Waves", *Mertericals Chemistry and Physics*, 90, 378–380 (2005).
- [2] T. Saiki, Y. Arisue, K. Kuramoto, H. Shizuka, M. Takeo, K. Maenaka, and Y. Utsumi, "Direction Control of Powder Transport on Solid Substrate by Drive Frequency of Surface Acoustic Wave Actuator", *Proc. of 38th International Conference on Micro and Nano Engineering (MNE2012)*, P270-022 (2012).

Recent Activity on the Development of Centrifugal Microfluidic Diagnostic Systems using Simple Principles and Equipment

Yoshiaki Ukita¹, and Yuichi Utsumi²

¹Department of Interdisciplinary Research, Graduate School of University of Yamanashi

²Laboratory of Advanced Science and Technology for Industry (LASTI), University of Hyogo

Abstract

As the attempt to realize simple microfluidic bio-analytical system we are aiming to develop 'mini-centrifuge driven microfluidic device'. In this report we show the development of the centrifugal force-driven microfluidic device that can be driven on mini-centrifuge instrument. The device is fabricated by conventional soft lithography and integrated on a compact disk (CD) substrate. The device is successfully driven on a minicentrifuge and the liquid controlling that necessary to implement bio-assay such as enzyme-linked immunosorbent assay (ELISA) is demonstrated. The device is applied to the detection of avidin-biotin interaction assay and it is proofed that the developed device has practical performance that comparable with conventional manual assay.

Introduction

Bio-maker testing from small volume of blood is required to realize next generations' health-care technologies. Microfluidic technologies, which realize extremely miniaturized and automated chemical processing, is promising to realize not only high throughput analysis but also revolutionize health care in house. On the other hand, that has been a issue for microfluidic system depends on the costly and bulky controlling system consist of syringe pump and valve unit, which makes the commercialization and wide spread of microfluidic technologies. [1, 2]

Centrifugal microfluidics is one of the simplest principles among existing controlling principle of microfluidics. [3-13] In this method a microchannel is integrated on the rotational device and pumping pressure is generated by centrifugal force by rotating the device. Because of the use of motor, a device possibly driven on a existing centrifuge equipment that available in many laboratory, therefore reduction of the cost for the development and price of the product can be realized. Various sequential flow controlling principles are proposed such that using capillary microvalve and rotational speed controlling [5], wax valving and laser irradiation [6], capillary action and rotational speed programming [8]. While various controlling principles are developed however all of these examples requires the complex programming of rotational speed.

Therefore the centrifuge instrument capable to sequentially change the rotational speed along the assay protocol. On the other hand the authors are paying attention to a mini-centrifuge instrument as device driver. The mini-centrifuge is compact and more affordable than other high-end centrifuge instruments and more widely available in

laboratory. By developing centrifuge instrument that adoptable to the mini-centrifuge, the commercialization of microfluidic devices can more easily be realized. On the other hand, mini-centrifuge is typically capable just rotate the rotor at constant speed, lack of programmability of rotational speed, therefore the existing controlling principles are not applicable. Therefore the authors are aiming to develop a novel controlling principle of centrifugal microfluidics that adoptable to mini-centrifuge.

Experiments and Results

Microfluidic structures are fabricated by using conventional soft-lithography method and the fabricated groove-shaped poly-dimethylsiloxane (PDMS) microchannel is closed by bonding the chip with flat PDMS film to obtain microfluidic chip. The bonded PDMS microfluidic chip is integrated on a compact disk (CD) substrate. Fig.1 shows the microfluidic device that mounted on a mini-centrifuge instrument, and the device can be driven by the use of the compact and affordable (500 USD) equipment. The microchip is consist of

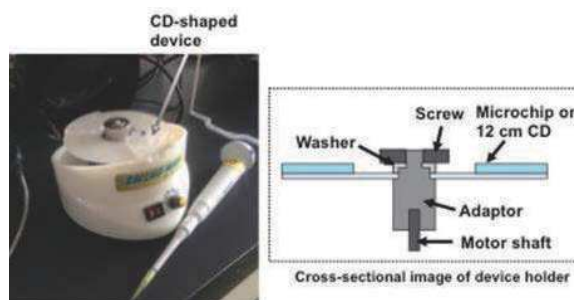


Fig.1 Centrifugal microfluidic device attached with mini-centrifuge instrument. (Reprinted from ref. 13 with permission by Sensors and Materials)

reaction chamber, reagent stock reservoirs waste reservoir, and microchannel (100 μm in diameter) network connecting each reservoirs and chamber for bio-assay. In case of centrifugal pumping, fluid located on the rotating system continuously experiences centrifugal force toward the periphery of the disk-shaped device. Therefore to hold the liquid in reaction chamber for incubation of bio-reaction for the assay, the siphon-shaped microchannel is integrated at the down stream of the reaction chamber. To draining the held liquid, additional liquid (such as washing solution) is added to the reaction chamber. This operation let the volume of liquid in reaction chamber exceeds the limit of liquid volume that can held in the reaction chamber and start draining of the liquid from the reaction chamber via siphon shaped microchannel.

Fig. 2 shows the observed flow behavior that demonstrated on an experimental set up shown in Fig. 1. The liquid is injected into the reaction

chamber and holding of the liquid in the chamber and draining is successfully repeated by repeating injection from reagent stock chamber. This operation demonstrates the flow control that required to realize bio-assay such as enzyme-linked immuno sorbent assay (ELISA). We applied the developed device for the demonstration of bioassay system for the detection of avidin using avidin-biotin interaction. For the assay the surface of reaction chamber is coated by biotin conjugated bovine serum albumin and the assay protocol is carried out.

Fig. 3 shows the calibration curve of the avidin that compares the conventional manual assay and developed device. It proofs that both system has reasonable response to the increasing avidin concentration and the developed device has comparable sensitivity with conventional manual assay. Therefore it is realized that the device having practical performance of bioassay is successfully developed.

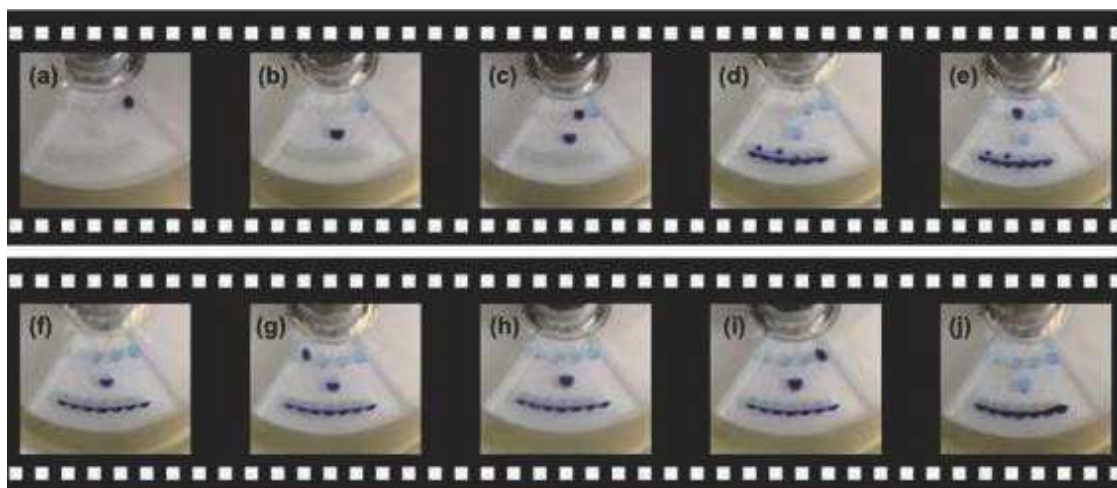


Fig. 2 Observed flow behavior driven by mini-centrifuge. (Reprinted from ref. 13 with permission by Sensors and Materials)

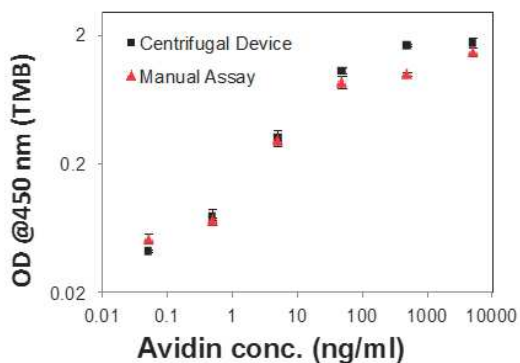


Fig. 3 Result of bio-analytical assay of avidin. (Reprinted from ref. 13 with permission by Sensors and Materials)

References

- [1] D. Mark, S. Haeberle, G. Roth, F. Stetten and R. Zengerle: *Chem. Soc. Rev.* **39** (2010) 1153.
- [2] D. Mark, F. Stettina and R. Zengerle: *Lab Chip* **12** (2012) 2464.
- [3] D. C. Duffy, H. L. Gillis, J. Lin, N. F. Sheppard, Jr. and G. J. Kellogg: *Anal. Chem.* **71** (1999) 4669.
- [4] R. Gorkin, J. Park, J. Siegrist, M. Amasia, B. S. Lee, J.-M. Park, J. Kim, H. Kim, M. Madou and Y.-K. Cho: *Lab Chip* **10** (2010) 1758.
- [5] S. Lay, S. Wang, J. Luo, L. J. Lee, S. T. Yang and M. J. Madou: *Anal. Chem.* **76** (2004) 1832.
- [6] B. S. Lee, J.-N. Lee, J.-M. Park, J.-G. Lee, S. Kim, Y.-K. Cho and C. Ko: *Lab Chip* **9** (2009) 1548.
- [7] Y. Ukita, S. Kondo, T. Azeta, M. Ishizawa, C.

- Kataoka, M. Takeo and Y. Utsumi: Sens. Actuators, B **166–167** (2012) 898.
- [8] J. Siegrist, R. Gorkin, L. Clime, E. Roy, R. Peytavi, H. Kido, M. Bergeron, T. Veres and M. Madou: Microfluid. Nanofluid. **9** (2010) 55.
- [9] T. Kawai, N. Naruishi, H. Nagai, Y. Tanaka, Y. Hagihara and Y. Yoshida: Anal. Chem. **85** (2013) 6587.
- [10] Y. Ukita and Y. Takamura: Microfluid. Nanofluid. **15** (2013) 829.
- [11] D. C. Duffy, J. C. McDonald, O. J. A. Schueller and G. M. Whitesides: Anal. Chem. **70** (1998) 4974.
- [12] Y. Ukita and Y. Takamura: Microfluid. Nanofluid. (2014) DOI 10.1007/s10404-014-1426-7.
- [13] Y. Ukita, Y. Utsumi, and Y. Takamura: Sensors and Materials **27** (2015) 391-402

Fabrication of X-ray Refractive Lens using Deep X-ray Lithography Technique

V. P. Dhamgaye¹, G. S. Lodha¹, Y. Utsumi², and A. Yamaguchi²

¹Indus Synchrotrons Utilisation Division, Raja Ramanna Centre for Advanced Technology, Indore, INDIA

²Laboratory of Advanced Science and Technology for Industry, University of Hyogo, JAPAN

Abstract

X-ray refractive lenses have been fabricated using Soft and Deep X-ray lithography (SDXRL) beamline on Indus-2. An array of x-ray lenses consist of few lenses to few tens of lenses in single line, are used for microfocussing of x-rays beam. The x-ray lenses fabricated using single step x-ray lithography process which will give one dimensional focussing elements. The two dimensional focusing can be obtained by using two different x-ray lenses array chips oriented in vertical and horizontal dispersion geometries. The produced x-ray lenses have parabolic profile in comparison to cylindrical profile which gives spherical aberration. The parabolic profile with acute vertical angles and sidewall surface roughness < 10 nm is difficult to fabricate by usual machining process. Various x-ray lenses from 1-50 numbers are produced in standalone PMMA sheets using deep x-ray lithography process. X-ray mask of required precision dimensions is manufactured in house using combined process of UV lithography and Au electrodeposition. X-ray mask contains ~ 15 µm thick gold absorbing patterned layer on polyimide supporting membrane. The fabricated x-ray lenses are characterized by demonstrating microfocussing of x-rays from Indus-2 synchrotron radiation source.

Introduction

Two decades back, refractive optics for microfocussing x-rays was considered impractical, as refractive index in x-ray region is slightly less than unity and absorption is high for high Z elements [1,2]. Advancing micro fabrication technologies have made a path easier for development of refractive and diffractive x-ray optical elements. The first design for the fabrication of x-ray refractive lens was proposed by Tomie [3] in low Z elements; pointing out the advantages of such optics compared with available reflecting and diffracting x-ray optics. To compensate a weak refraction from materials, many lenses were stacked together and later called as compound refractive lenses (CRL). The first CRL for hard x-rays were fabricated and tested by Snigirev *et.al.* [4]. Microfocus x-ray beams, of few microns or submicrons sizes are required at many synchrotron radiation facilities to perform scientific experiments, like micro-diffraction, micro-fluorescence and micro-EXAFS. Various types of materials such as silicon, Nickel, Beryllium Aluminum, SU-8 and PMMA are used for CRLs fabrication using different techniques. Deep X-ray lithography (DXRL) has provided the means for precision micro fabrication of x-ray optical lens with high aspect ratio and good vertical sidewalls with low roughness [5]. In this article, we report the design and development of parabolic CRL using DXRL technique.

CRL design

All materials in the x-ray region have very small refractive index decrement and strong absorption. The refractive index ($n = 1 - \delta + i\beta$) is slightly less than unity in x-ray region. The refractive index decrement ($\sim 10^{-6}$) describes the strength of refraction with respect to vacuum. The imaginary part ($\sim 10^{-8}$) is related to the absorption of x-rays in the medium. Owing to small refraction effects in the medium at x-ray wavelengths, the converging power of the lens is very small. The focal length of single refractive lens is given by $f_1 = (R/2\delta)$ where R is radius of curvature of lens at the apex. Fig. 1 describes the schematic of single parabolic lens profile in (a) 2D and (b) 3D view. For PMMA, at 10 keV, $\delta = 2.5 \times 10^{-6}$ and if we consider $R = 500 \mu\text{m}$, the focal length for a single lens will be $\sim 100 \text{ m}$. This focal length is impractical for

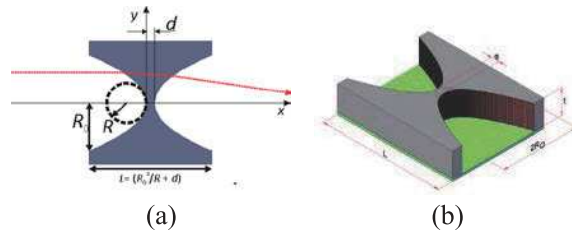


Fig. 1: Single parabolic lens consisting of bi-concave lens (a) 2-D view (b) 3-D view, where R is the radius of curvature at the apex and $2R_0$ defines the geometrical aperture. The thickness of the lens at the apex is d and total length of the single lens is given by $(R_0^2/R + d)$ and lithographically developed depth t .

performing experiments using x-ray beamlines.

Focal length can be reduced by increasing the number of individual lenses (N) which will give N times shorter focal length ($f = f_1 / N$) and are referred as CRL.

With higher number of lenses, the focusing power of the lens increases due to $2N$ refraction but effective transmission decreases due to absorption in the lens material, thus necessitating a high brightness x-ray source (not a lab based generator source). The CRL is designed taking into account the optical response of the lens material in the desired energy region and lens profile. For reduction in spherical aberration, a parabolic profile is chosen over cylindrical profile. However, these lenses suffer the chromatic aberration. X-ray sensitive photoresist, poly methyl metha acrylate (PMMA) is composed of low Z elements, specially containing carbon atoms. We have designed the CRL for Indus-2 bending magnet source, using formalism given by Lengeler *et.al.* [6]. X-ray lenses with $N = 1-50$, $R = 200 \mu\text{m}$, $2R_0 = 400 \mu\text{m}$ and $d = 20 \mu\text{m}$ are planned to fabricate in PMMA material.

Fabrication of CRL using DXRL

X-ray Mask

DXRL technique requires precision quality 1X x-ray mask. Any errors in the x-ray mask will easily duplicate in the required micro structures. A $300 \mu\text{m}$ thick, 100 mm diameter brass wafer was used as seed substrate to create x-ray mask containing CRL profiles. The UV mask containing CRL patterns was used to create pattern on brass wafer using UV lithography. Thin film ($0.5 \mu\text{m}$) of Ni followed by thick film ($15 \mu\text{m}$) of Au was electro-deposited in the resist cavity to create absorber pattern. A polyimide solution was then spin coated on an inverse lens-shaped gold absorber on brass substrate. A stainless steel ring was bonded to support stand alone polyimide film and brass wafer was etched out. This process is also described in detail using processing steps by Dhamgaye *et.al.*[7].

X-ray Exposure

The details of the beamline used for DXRL is described elsewhere [8]. Two X-ray mirrors are set to grazing incidence angles to tune beam energy spectrum in the range of 5-12 keV and beam size of 12 mm (V) and 80 mm (H). These beamline settings were used to expose $500-1000 \mu\text{m}$ PMMA sheets. During the exposure the dose rate was controlled to within 4 kJ/cm^3 at the bottom and 20 kJ/cm^3 at the top. SEM image of fabricated CRL

in PMMA is shown in figure 2 (a).

Microfocussing characterization of CRL

Microfocussing characterization of fabricated PMMA x-ray lenses was carried out at BL-16, Indus 2.. Fabricated PMMA plane parabolic CRLs with total lenses equal to 50 were characterised. The lenses were mounted in vertical dispersion geometry on five degree of freedom alignment/movement stages. The distance between the source to lens was 20 m and lens to detector distance was 1 m . The x-ray energy from double crystal monochromator was tuned and best focus spot size for $\sim 10 \text{ keV}$ was obtained. X-ray CCD camera was used to record line focus images. The incident beam size on CRL was $300 \times 400 \mu\text{m}^2$ which was focused by CRL to $300 \times 20 \mu\text{m}^2$. Fig. 2(b) shows the focused line image recorded on x-ray CCD camera. The calculated spot size was $13.5 \mu\text{m}$ for Indus-2 source for this characterization setup and measured value is found to be $20 \mu\text{m}$. The focused spot size of is greater than expected at 10 keV . This is perhaps due to the difference in bulk density of PMMA and the density of PMMA sheets. The error in the spot size may also be attributed due to lens profile error which is within $1-2 \mu\text{m}$ from ideal profile.

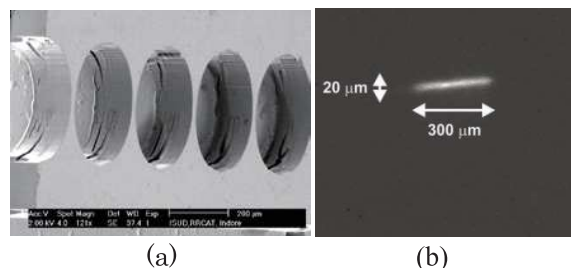


Fig. 2: (a) SEM micrograph of PMMA X-ray lenses fabricated at Indus-2 BL-7 beamline(b)

Summary

X-ray refractive lenses are fabricated in PMMA using deep x-ray lithography technique. They have been characterized using synchrotron x-rays and microfocussing results have been obtained.

Further this lenses can be fabricated by reducing the radius of curvature down to $1-5 \mu\text{m}$ and strict fabrication tolerance in parabolic profile which may require the use of electron beam lithography for fabrication of precision x-ray mask.

References

- [1] S. Suehiro, H. Miyaji, and H. Hayashi, Nature **352**, 385 (1991).
- [2] A. G. Michette Nature **353**, 510 (1991).
- [3] T. Tomie, Japanese Patent 2 526 409 (1994).

- [4] A. Snigirev, V. Kohn, I. Snigireva and B. Lengeler, *Nature* **384**, 49–51(1996).
- [5] R. K. Kupka, F. Bouamrane, M. Roulliay and S. Megtret, *SPIE* **3680**, 508 (1999).
- [6] B. Lengeler, J. Tummler, A. Snigirev, I. Snigireva, and C. Raven, *Journal of Applied Physics* **84**, 5855 (1998).
- [7] V. P. Dhamgaye, M. K. Tiwari, K. J. S. Sawhney and G. S. Lodha, *Pramana J. Phys.* **83(1)**, 119–129 (2014).
- [8] V. P. Dhamgaye, G. S. Lodha, B. Gowri Sankar and C. Kant, *J. Synch. Rad.* **21**, 259-263 (2014).

List of publications

(1) Papers

1. **"Development of Terahertz Radiation Sources using Compact Linear Accelerator LEENA"**
Satoshi Hashimoto, Sayaka Chin, Karin Kobayashi, Kenji Kawata, Dazhi Li, Sho Amano, Shuji Miyamoto
IEEJ Trans. Electronic, Information and Systems Vol.134, No.4, pp495-501 (2014)
2. **"Energy Calibration of the NewSUBARU Storage Ring for Laser Compton-Scattering Gamma Rays and Applications"**
H.Utsunomiya, T.Shima, K.Takahisa, D. M. Filipescu, O. Tesileanu, I. Gheorghe, H.-T. Nyhus, T. Renstrøm, Y.-W. Lui, Y. Kitagawa, S. Amano, S. Miyamoto
IEEE Transactions on Nuclear Science, Volume 61, No 3, pp.1252-1258 (2014).
3. **"Cherenkov radiation oscillator without reflectors"**
D. Li, Y. Wang, M. Hangyo, Y. Wei, Z. Yang, and S. Miyamoto
Appl. Phys. Lett., vol.100, 194102 (2014).
4. **"放射光軟 X 線照射による Si 系非晶質半導体膜の結晶化に光子エネルギーが与える影響"**
松尾直人, 部家 彰, 天野 壮, 宮本 修治, 神田 一浩, 望月 孝晏
日本真空学会誌, 57 巻, 6 号, pp.227-232 (2014).
5. **"Shielding design of laser electron photon beamlines at SPring-8"**
Yoshihiro Asano, Shuji Miyamoto and LEPS-II Collaboration
Progress in Nuclear Science and Technology, vol.4, pp.252-256 (2014).
6. **"Neutron angular distribution in (γ ,n) reactions with linearly polarized γ -ray beam generated by laser Compton scattering"**
K.Horikawa, S.Miyamoto, T.Mochizuki, S.Amano, D.Li, K.Imsakaki, Y.Izawa, K.Ogata, S.Chiba, T.Hayakawa
Physics Letters B, 737, pp.109-113 (2014).
7. **"Photoneutron cross sections for samarium isotopes: Toward a unified understanding of (γ , n) and (n, γ) reactions in the rare earth region"**
D. M. Filipescu, I. Gheorghe, H. Utsunomiya, S. Goriely, T. Renstrøm, H.-T. Nyhus, O. Tesileanu, T. Glodariu, T. Shima, K. Takahisa, S. Miyamoto, Y.-W. Lui, S. Hilaire, S. Pe'ru, M. Martini, and A. J. Koning
Physical Review C, Vol. 90, Iss. 6, 064616 (2014).
8. **"Photoneutron cross sections for neodymium isotopes: Toward a unified understanding of (γ , n) and (n, γ) reactions in the rare earth region"**
H.-T. Nyhus, T. Renstrøm, H. Utsunomiya, S. Goriely, D. M. Filipescu, I. Gheorghe, O. Tesileanu, T. Glodariu, T. Shima, K. Takahisa, S. Miyamoto, Y.-W. Lui, S. Hilaire, S. Pe'ru, M. Martini, L. Siess, and A. J. Koning
Physical Review C, Vol. 91, Iss. 1, 015808 (2015).
9. **"Laser plasma cryogenic target on translating substrate for generation of continuously repetitive EUV and soft X-ray pulses"**
S.Amano,
Rev.Sci.Instrum., Vol.85 , 063104 (2014).

10. **“Microprocessing using soft X-ray from laser produced Xe plasma ”**
S.Amano, T.Inoue, S.Miyamoto
IEEJ Trans. on Electro. Info. and Sys., Vol.**134**, 489 (2014).
11. **”Damage Characteristics of n-GaN Thin Film Surfaces Etched by Ultraviolet Light-Assisted Helium Plasmas”**
R. Kawakami, M. Niibe, Y. Nakano, T. Shirahama, K. Aoki, K. Oba, M. Takabatake, T. Mukai:
Thin Solid Films, **570**, 81-86, (2014).
12. **“Optical and electrical investigation of Ar⁺-irradiated GaN”**
M-G. Chen, K. Nakamura, Y-Q. Qiu, D. Ogawa, R. Kawakami, M. Niibe, and Y. Nakano:
Appl. Phys. Express, **7**, 111003, (2014).
13. **”Structure dependence of corrosion resistance of amorphous carbon films against nitric acid”**
A. Takarada, T. Suzuki, K. Kanda, M. Niibe, M. Nakano, N. Ohtake, H. Akasaka:
Diamond and Related Materials, **51**, 49-54 (2015).
14. **“Hyperthermal atomic oxygen beam irradiation effect on the Ti-containing DLC film”**
K.Kanda, K.Fukuda, K.Kidena, R.Imai, M.Niibe, S.Fujimoto, K.Yokota, M.Tagawa
Diamond and Related Materials, Vol. **41**, Pages 49-52 (2014).
15. **“Soft X-ray irradiation effect on the surface and material properties of highly hydrogenated diamond-like carbon thin films”**
Ryo Imai, Akihiro Fujimoto, Makoto Okada, Shinji Matsui, Takahiro Yokogawa, Eri Miura, Tohru Yamasaki, Tsuneo Suzuki, Kazuhiro Kanda
Diamond and Related Materials, Vol. **44**, Pages 8-10 (2014).
16. **“Sulfur accumulation in Melanodermis during development by upbuilding pedogenesis since 14-15 cal. ka”**
Toko Tanikawa, Yohey Hashimoto, Noriko Yamaguchi, Yoshiaki Ito, Sei Fukushima, Kazuhiro Kanda, Masaharu Uemura, Takayuki Hasegawa, Masamichi Takahashi, Shuichiro Yoshinaga,
Geoderma **232–234**, 609-618 (2014).
17. **“Tailored design of boron-doped diamond electrodes for various electrochemical applications with boron-doping level and sp²-bonded carbon impurities”**
Yutaro Suzuki, Tsuneo Suzuki, Kazuhiro Kanda, Naoto Ohtake, Hiroki Akasaka
Phys. Status Solidi A **211**, No. 12, 2709-2717 (2014).
18. **“Molecular orientation of a photoreactive liquid crystalline polymer induced by thermal nanoimprinting and graphoepitaxy”,**
M. Okada, R. Hosoda, M. Kondo, Y. Haruyama, T. Sasaki, H. Ono, N. Kawatsuki, and S. Matsui
Microelectronic Engineering, **123**, pp. 159-162 (2014).
19. **“Localized Abrasion Resistance Test for Antisticking Layer by Atomic Force Microscopy”,**
M. Okada, Y. Haruyama, and S. Matsui
Journal of Photopolymer Science and Technology, **27**, pp.103-106 (2014).
20. **“Effect of Fluorosurfactant contained in Resin for Anti-sticking Layer Free UV Nanoimprinting”,**
T. Oyama, M. Okada, S. Iyoshi, Y. Haruyama, T. Yamashita, and S. Matsui
Journal of Photopolymer Science and Technology, **27**, pp.117-120 (2014).

21. **“Chemical Patterns Fabricated by Nanoimprinting for Block Copolymer Directed Self-Assembly”**,
H. Wakaba, M. Okada, S. Iyoshi, Y. Haruyama and S. Matsui
Journal of Photopolymer Science and Technology, **27**, pp.99-102 (2014).
22. **“Release Property of HSQ Replica Mold Fabricated by Room Temperature Nanoimprinting with PDMS soft mold”**,
N. Sugano, M. Okada, Y. Haruyama, and S. Matsui
Journal of Photopolymer Science and Technology, **27**, pp.81-84 (2014).
23. **”Evaluation of fluorosurfactant distribution in ultrathin UV nanoimprint resin by X-ray photoelectron spectroscopy”**,
T. Oyama, M. Okada, S. Iyoshi, Y. Haruyama, and S. Matsui
Japanese Journal of Applied Physics, **53**, 06JK06 (2014).
24. **“Evaluation of Young’s modulus of imprinted hydrogen silsesquioxane pillar after residual layer removal by reactive ion etching,**
Y. Kang, Y. Haruyama, S. Matsui
Microsystem Technologies”, **20**, 1899-1903 (2014).
25. **“Fabrication of gold nanoparticle pattern using imprinted hydrogen silsesquioxane pattern for surface-enhanced Ramanscattering”**,
Y. Kang, T. Fukuoka, R. Takahashi, Y. Utsumi, Y. Haruyama, and S. Matsui
Microsystem Technologies, **20**, 1993-2000 (2014).
26. **“Evaluation of Fluorinated Self-assembled Monolayer by Using Photoelectron and Near Edge X-ray Absorption Fine Structure Spectroscopies”**,
Y. Haruyama, M. Okada, Y. Nakai, T. Ishida, and S. Matsui
IEEE Transactions on Electronics, Information and Systems, **134**, 468-472 (2014).
27. **“EUV Resist Chemical Analysis by Soft X-ray Absorption Spectroscopy for High Sensitivity Achievement”**,
K. Emura, T. Watanabe, M. Yamaguchi, H. Tanino, T. Fukui, D. Shiono, Y. Haruyama, Y. Muramatsu, K. Ohmori, K. Sato, T. Harada, H. Kinoshita
Journal of Photopolymer Science and Technology, **27**, 631-638 (2014).
28. **“Comparison of the Photoinduced Orientation Structure in the Bulk and at the Near-Surface of a Photoalignable Liquid Crystalline Polymer Film”**,
N. Kawatsuki, Y. Taniguchi, M. Kondo, Y. Haruyama, S. Matsui
Macromolecules **48**, 2203–2210 (2015).
29. **“Synchrotron radiation absorption spectroscopy to enhance photoresists”**
Takeo Watanabe, Kazuya Emura, Daiju Shiono, Yuichi Haruyama, Yasuji Muramatsu, Katsumi Ohmori, Kazufumi Sato, Tetsuo Harada, and Hiroo Kinoshita
SPIE Newsroom, DOI: 10.1117/2.1201403.005299 (2014).

30. **“Demonstrating 30-nm spatial resolution of three-multilayer-mirror objective for extreme ultraviolet microscopy: Imaging test by observing lithography mask”**
Mitsunori Toyoda, Kenjiro Yamasoe, Akifumi Tokimasa, Kentaro Uchida, Tetsuo Harada, Tsuneo Terasawa, Tsuyoshi Amano, Mihiro Yanagihara, and Hiroo Kinoshita
Appl. Phys. Express **7**, 102502 (2014).
31. **“Characterization of small phase defects using a micro-coherent extreme ultraviolet scatterometry microscope”**
Yusuke Tanaka, Tetsuo Harada, Tsuyoshi Amano, Youichi Usui, Takeo Watanabe, and Hiroo Kinoshita
Jpn. J. Appl. Phys. **53**, 06JC03 (2014).
32. **“Multilayer reflectometry and quantitative analysis of higher order diffraction impurities of grating monochromator”**
Tadashi Hatano, Tetsuo Harada
J. Electron. Spectrosc. Relat. Phenom. **195**, 156-158 (2014).
33. **“Development of EUV mask inspection system using high-order harmonic generation with a femtosecond laser”**
Hiroo Kinoshita, Tetsuo Harada, Yutaka Nagata, Takeo Watanabe and Katsumi Midorikawa
Jpn. J. Appl. Phys. **53**, 086701 (2014).
34. **“Study of Acid Diffusion Behaviors of PAG by Using Top Coat Method for EUVL”**
Atsushi Sekiguchi, Takeo Watanabe, and Hiroo Kinoshita
J. Photopolym. Sci. Technol. **27** pp. 623- 629 (2014).
35. **“EUV Resist Chemical Analysis by Soft X-ray Absorption Spectroscopy for High Sensitivity Achievement”**
Kazuya Emura, Takeo Watanabe, Masato Yamaguchi, Hirohito Tanino, Tsubasa Fukui, Daiju Shiono, Yuichi Haruyama, Yasuji Muramatsu, Katsumi Ohmori, Kazufumi Sato, Tetsuo Harada, and Hiroo Kinoshita
J. Photopolym. Sci. Technol. **27**, 631-638 (2014).
36. **“Cellular Automaton-based Nanoelectronic Hardware”**
Takeo Watanabe, Tejiro Isokawa, and Nobuyuki Matsui
6th IEEE International Nanoelectronics Conference, pp. 1-3. (2014).
37. **“Observation of phase defect on extreme ultraviolet mask using an extreme ultraviolet microscope”**
Tsuyoshi Amano, Tsuneo Terasawa, Hidehiro Watanabe, Mitsunori Toyoda, Tetsuo Harada, Takeo Watanabe, and Hiroo Kinoshita
J. Micro/Nanolith. MEMS MOEMS **13**, 023012 (2014).
38. **“At-wavelength observation of phase defect using focused lensless microscope”**
T. Harada, Y. Tanaka, T. Amano, Y. Usui, T. Watanabe, H. Kinoshita
SPIE Proc. **9048**, 90483F (2014).
39. **“At wavelength observation of phase defect embedded in EUV mask using microscope technique”**
T. Terasawa, T. Amano, T. Yamane, H. Watanabe, M. Toyoda, T. Harada, T. Watanabe, H. Kinoshita
SPIE Proc. **9048**, 904825 (2014).

40. **“Observation of phase defect on extreme ultraviolet mask using an extreme ultraviolet microscope”**
T. Amano, T. Terasawa, H. Watanabe, M. Toyoda, T. Harada, T. Watanabe, H. Kinoshita
SPIE Proc. **9048**, 904827 (2014).
41. **“Contribution of EUV resist components to the non-cleanable contaminations”**
E. Shiobara, T. Takahashi, N. Sugie, Y. Kikuchi, I. Takagi, K. Katayama, H. Tanaka, S. Inoue, T. Watanabe, T. Harada, H. Kinoshita
SPIE Proc. **9048**, 904819 (2014).
42. **“Correlation study on resist outgassing between EUV and e-beam irradiation”**
Y. Kikuchi, K. Katayama, I. Takagi, N. Sugie, T. Takahashi, E. Shiobara, H. Tanaka, S. Inoue, T. Watanabe, T. Harada, H. Kinoshita
SPIE Proc. **9048**, 90482W (2014).
43. **“ニュースバル多目的ビームライン BL10 における軟X線吸収分析（3）；液体有機化合物とエンジンオイルの状態分析”**
植村智之、村松康司、南部啓太、原田哲男、木下博雄
X線分析の進歩第 **45** 集, 269 (2014). (in Japanese)
44. **“半導体デバイスの X 線照射耐性に関する迅速評価方法の開発”**
工藤統吾, 小林和生, 小野峻, 寺西信一, 渡邊健夫, 木下博雄, 沖原将生, 初井宇記
応用物理学会分科会シリコンテクノロジー 170 半導体デバイスに対する放射線照射効果,
pp.24-29 (2014). (in Japanese)
45. **“Fabrication of gold nanoparticle pattern using imprinted hydrogen silsesquioxane pattern for surface-enhanced Raman scattering”**,
Yuji Kang, Takao Fukuoka, Ryo Takahashi, Yuichi Utsumi, Yuichi Haruyama, and Shinji Matsui,
Microsystem Technologies, **20**, 1993-2000 (2014).
46. **“Broadband noise spectroscopy of a nano-scale magnetic wire”**,
Akinobu Yamaguchi, K. Motoi, H. Miyajima and Yuichi Utsumi,
Journal of Magnetism and Magnetic Materials **364**, 34-38 (2014).
47. **“High-Efficiency Mixing Chip with Liquid flow Actuators Operated by Surface Acoustic Waves”**,
Tsunemasa Saiki and Yuichi Utsumi,
Electronics and Communications in Japan, **97**, 1, 54-61 (2014).
48. **“Powder Transport by Surface Acoustic Wave Actuator using Bragg Reflection”**, Tsunemasa Saiki,
Yuya Matsui, Yasuto Arisue, Yuichi Utsumi and Akinobu Yamaguchi, IEEJ Transactions on Electronics,
Information and Systems, Vol. **134**(No. 12) pp. 1934-1935 (2014).
49. **“Surface-enhanced Raman spectroscopy using a coffee-ring-type three-dimensional silver nanostructure”**, Ryohei Hara, Takao Fukuoka, Ryo Takahashi, Yuichi Utsumi and Akinobu Yamaguchi,
RSC Advances, **5**, 1378-1384 (2014).

50. **“Measurement of Reduced Elastic Modulus of Organic Semiconductor Materials for Flexible Organic Light Emitting Diode”**,
T. Kobayashi, H. Ikeda, Y. Utsumi, H. Kanematsu, T. Masuda and M. Yamamoto, ,
Journal of the Japanese Society for Experimental Mechanics, **14**, s189-s193 (2014).
51. **“Improvement in the Ductility of Organic Semiconductor Materials Used in a Flexible Organic Light Emitting Diode”**,
T. Kobayashi, T. Yokoyama, Y. Utsumi, H. Kanematsu, T. Masuda and M. Yamamoto, Journal of the
Japanese Society for Experimental Mechanics, **14**, s194-s199 (2014).
52. **“Design and Prototyping of a Fuel Cell Controlling Equipment for Small Hybrid Driving Airship System”**, T. Kobayashi , M. Fukushima, H. Kanematsu, Y. Utsumi, and Y. Shimamoto,
Advanced Materials Research, **933**, 444-449 (2014).
53. **“Coupled oscillations of vortex cores confined in a ferromagnetic elliptical disk”**,
H. Hata, M. Goto, A. Yamaguchi, T. Sato, Y. Nakatani and Y. Nozaki,
Physical Review B **90**, 104418-1-14 (2014).

(2) **International meetings**

1. **"Production of Positrons via Pair Creation from LCS Gamma-rays and Application to Defect Study in Bulk Materials"**
F. Hori, K. Ishii, T. Ishiyama, A.o Iwase, S. Miyamoto, and M. Terasawa
Proc. 2nd Japan-China Joint Workshop on Positron Science, JJAP Conf. Proc. 2, 011301 (2014).
2. **"Laser Compton Scattering Gamma-Ray Beam Source at NewSUBARU Storage Ring"**
S.Miyamoto, S.Amano, S.Hashimoto, N.Sakai and A.Koizumi, T.Hayakawa, T.Shizuma, H.Utsunomiya, T.Yamagata, H.Akimune, T.Shima, D.Li, Y.Asano, H.Ohkuma
Proceedings of the International Symposium "Nuclear Physics and Gamm-Ray Sources for Nuclear Security and Nonproliferation", Ricotta, Tokai-mura, Japan, 28-30 Jan. 2014, Ed. T. Hayakawa, M. Senzaki, P. Bolton, R. Hajima, M. Seya, M. Fujiwara, World Scientific Publishing, Singapore, pp.143-150 (2014) ISBN 978-981-4635-44-8.
3. **"Medium Modification of α Cluster Size in 6Li "**
T.Yamagata, H.Akimune, S.Nakayama, T.Shima and S.Miyamoto
Ibid., pp.171-176. (2014) ISBN 978-981-4635-44-8.
4. **"Photodisintegration Reaction with Linear Polarized γ -Ray Beam"**
T.Hayakawa, S.Miyamoto, K.Horikawa, S.Amano, T.mochizuki, K.Imasaki, D.Li, Y.Izawa, K.Ogata, S.Chiba
Ibid., pp.301-307. (2014) ISBN 978-981-4635-44-8.
5. **"HARPO: a TPC concept for γ -ray polarimetry with high angular resolution in the MeV-GeV range"**
S. Wang, D. Bernard, P. Bruel, M. Frotin, Y. Geerebaert, B. Giebels, P. Gros, D. Horan, M. Louzir, P. Poilleux, I. Semeniouk, S. Anvar, D. Atti'e, P. Colas, A. Delbart, P. Sizun, D. G'otz, S. Amano, T. Kotaka, S. Hashimoto, Y. Minamiyama, A. Takemoto, S. Miyamoto, M. Yamaguchi, S. Dat'e, H. Ohkuma
7th Symposium on Large TPCs for Low-Energy Rare Event Detection, Paris, 15-17 December 2014.
6. **"Generation Behavior of Deep-Level Defects in Ar^{++} -Irradiated GaN"**
Yoshitaka Nakano, Miao-Gen Chen, Daisuke Ogawa, Keiji Nakamura, Retsuo Kawakami, Masahito Niibe:
7th International Symposium on Advanced Plasma Science and Its Applications for Nitrides and Nanomaterials (ISPlasma2015) 26-31, March 2015, Nagoya, Japan.
7. **"Etching damage analysis of n-GaN crystals etched with N_2 -plasma using soft X-ray absorption spectroscopy"**
Masahito Niibe, Takuya Kotaka, Retsuo Kawakami, Yoshitaka Nakano and Takashi Mukai:
36th International Symposium on Dry Process (DSP2014), Nov. 27-28 (2014) Yokohama, Japan.
8. **"Morphological and Compositional Changes in AlGaN Surfaces etched by RF Capacitively Coupled Carbon Tetrafluoride and Argon Plasmas"**
R. Kawakami, M. Niibe, Y. Nakano, T. Shirahama, S. Hirai and T. Mukai:
36th International Symposium on Dry Process (DSP2014), Nov. 27-28 (2014) Yokohama, Japan.
9. **"Spectral Recovery of Etching Damage of TiO_2 thin film Observed in XAS Spectra"**
Keiji Sano, Masahito Niibe, Retsuo Kawakami, Yoshitaka Nakano:
7th International Symposium on Surface Science (ISSS-7), Nov. 2-6 (2014) Matsue, Japan.

10. **"Surface analysis of AlGaN treated by Ar and CF₄ plasma etching"**
Shodai Hirai, Masahito Niibe, Retsuo Kawakami, Yoshitaka Nakano:
7th International Symposium on Surface Science (ISSS-7), Nov. 2-6 (2014) Matsue, Japan.
11. **"Damage Characteristics of n-GaN Crystal Etched with N₂ Plasma by Soft X-ray Absorption Spectroscopy"**
Masahito Niibe, Takuya Kotaka, Retsuo Kawakami, Yoshitaka Nakano and Takashi Mukai:
7th International Symposium on Surface Science (ISSS-7), Nov. 2-6 (2014) Matsue, Japan.
12. **"Surface Modification on Horizontally Aligned Multi-walled Carbon Nanotube Films by Ar Ion Irradiation"**
R.Tamura, A.Tsukagoshi, S.Honda, M.Niibe, M.Terasawa, R.Hirase, H.Yoshioka, H.Izumi, K.Niwase, E.Taguchi, K.-Y.Lee, and M.Oura:
The 15th IUMRS-International Conference in Asia (IUMRS-ICA 2014), Fukuoka, Japan, August 24-30, 2014.
13. **"Atomic Oxygen Beam Irradiation Effect on the Si-doped DLC Film"**
Kengo Kiden, Minami Endo, Ryo Imai, Masahito Niibe, Kumiko Yokota, Masahito Tagawa, Kazuhiro Kanda
The 15 th IUMRS-International Conference in Asia 2014/8/24-30 Fukuoka Univ.
14. **"Isotopic influence on amorphous carbon films"**
Yutaro Suzuki, Tsuneo Suzuki, Kazuhiro Kanda, Naoto Ohtake, Hiroki Akasaka
The 15 th IUMRS-International Conference in Asia 2014/8/24-30 Fukuoka Univ.
15. **"Molecular orientation of imprinted nm-order pattern of photo-cross-linkable liquid crystalline polymer"**,
M. Okada, R. Hosoda, M. Kondo, Y. Haruyama, T. Sasaki, H. Ono, N. Kawatsuki, and S. Matsui
58th International Conference on electron, ion, photon beam technology and fabrication(EIPBN2014), Washington, D.C. USA, 2014/5/28
16. **"Surface evaluation of HSQ with PDMS additive after room temperature nanoimprinting using hard and soft molds"**,
N. Sugano, M. Okada, Y. Haruyama, and S. Matsui,
58th International Conference on electron, ion, photon beam technology and fabrication(EIPBN2014), Washington, D.C. USA, 2014/5/28
17. **"Localized Abrasion Resistance Test for Antisticking Layer by Atomic Force Microscopy"**,
M. Okada, Y. Haruyama, and S. Matsui,
31st International Conference of Photopolymer Science and Technology, Chiba, Japan, 2014/7/10
18. **"Effect of Fluorosurfactant contained in Resin for Anti-sticking Layer Free UV Nanoimprinting"**,
T. Oyama, M. Okada, S. Iyoshi, Y. Haruyama, T. Yamashita, and S. Matsui,
31st International Conference of Photopolymer Science and Technology(ICPST-31), Chiba, Japan, 2014/7/10
19. **"Chemical Patterns Fabricated by Nanoimprinting for Block Copolymer Directed Self-Assembly"**,
H. Wakaba, M. Okada, S. Iyoshi, Y. Haruyama, and S. Matsui,

- 31st International Conference of Photopolymer Science and Technology(ICPST-31), Chiba, Japan, 2014/7/10
20. **"Release Property of HSQ Replica Mold Fabricated by Room Temperature Nanoimprinting with PDMS soft mold"**,
N. Sugano, M. Okada, Y. Haruyama and S. Matsui,
31st International Conference of Photopolymer Science and Technology(ICPST-31), Chiba, Japan, 2014/7/10
 21. **"EUV Resist Chemical Reaction Analysis by Soft X-ray Absorption Spectroscopy for High Sensitivity"**,
K. Emura, T. Watanabe, D. Shiono, M. Yamaguchi, H. Tanino, T. Fukui, Y. Haruyama, Y. Muramatsu, K. Ohmori, K. Sato, T. Harada, H. Kinoshita,
31st International Conference of Photopolymer Science and Technology(ICPST-31), Chiba, Japan, 2014/7/11
 22. **"Material dependency of liquid crystalline polymer's molecular orientation by nanoimprint-graphoepitaxy"**,
M. Okada, R. Hosoda, M. Kondo, Y. Haruyama, T. Sasaki, H. Ono, N. Kawatsuki, and S. Matsui,
40th International Conference on Micro and Nano Engineering (MNE2014), Lausanne, Switzerland, 2014/9/24
 23. **"Evaluation of molecular orientation in liquid crystalline polymer structure fabricated by nanoimprinting"**,
M. Okada, R. Hosoda, M. Kondo, Y. Haruyama, T. Sasaki, H. Ono, N. Kawatsuki, and S. Matsui,
13th International Conference on Nanoimprint and Nanoprint Technology (NNT2014), Kyoto, Japan, 2014/10/23
 24. **"Study on Deterioration Mechanism of Antisticking Layer in Repeated UV Nanoimprint"**,
S. Iyoshi, M. Okada, Y. Haruyama, M. Nakagawa, H. Hiroshima, and S. Matsui,
13th International Conference on Nanoimprint and Nanoprint Technology (NNT2014), Kyoto, Japan, 2014/10/23
 25. **"Consideration of Resin Peeling In UV Nanoimprint Without Antisticking Layer"**,
T. Oyama, T. Yamashita, M. Okada, S. Iyoshi, Y. Haruyama, and S. Matsui,
13th International Conference on Nanoimprint and Nanoprint Technology (NNT2014), Kyoto, Japan, 2014/10/23
 26. **"Reversal Room-Temperature Nanoimprinting for 3D HSQ Structure"**,
N. Sugano, M. Okada, Y. Haruyama, and S. Matsui,
13th International Conference on Nanoimprint and Nanoprint Technology (NNT2014), Kyoto, Japan, 2014/10/23
 27. **"Chemical Guide Pattern Fabricated by Thermal Nanoimprinting for Alignment of PS-b-PMMA Microdomains"**,
H. Wakaba, M. Okada, S. Iyoshi, Y. Haruyama, and S. Matsui,
13th International Conference on Nanoimprint and Nanoprint Technology (NNT2014), Kyoto, Japan, 2014/10/23

28. **"Photoelectron Spectroscopy Study of the Fluorinated Antisticking Layers for Nanoimprint Lithography"**,
Y. Haruyama, M. Okada, Y. Nakai, T. Ishida, and S. Matsui,
3th International Conference on Nanoimprint and Nanoprint Technology (NNT2014), Kyoto, Japan, 2014/10/23
29. **"Chemical Guide Pattern Fabricated by Thermal Nanoimprinting Using One Terminal Functionalized PS and PS-r-PMMA Polymers"**,
H. Wakaba, S. Iyoshi, M. Okada, Y. Haruyama, and S. Matsui,
27th International Microprocesses and Nanotechnology Conference (MNC2014), Fukuoka, Japan, 2014/11/7
30. **"3D HSQ Structure Fabrication by Reversal RT-Nanoimprint Using PDMS Mold"**,
N. Sugano, M. Okada, Y. Haruyama, and S. Matsui,
27th International Microprocesses and Nanotechnology Conference(MNC2014), Fukuoka, Japan, 2014/11/7
31. **"Evaluation of the Fluorinated Antisticking Layer by Using Photoemission and NEXAFS Spectroscopies"**,
Y. Haruyama, M. Okada, Y. Nakai, T. Ishida, S. Matsui,
7th International Microprocesses and Nanotechnology Conference(MNC2014), Fukuoka, Japan, 2014/11/7
32. **"Evaluation of the Photoinduced Orientation Behavior of Photoreactive Liquid Crystalline Polymer Film in Bulk and at the Near-Surface"**,
Y. Taniguchi, Y. Inada, M. Kondo, Y. Haruyama, S. Matsui, N. Kawatsuki,
2nd Asian Conference on Liquid Crystals, Busan, Korea, 2015/1/20
33. **"Development of Micro Coherent EUV Scatterometry Microscope for Phase Defect Observation"**
Tetsuo Harada, Yusuke Tanaka, Tsuyoshi Amano, Youichi Usui, Takeo Watanabe, Hiroo Kinoshita
Photomask Japan 2014, Yokohama, Japan, 2014/4/15
34. **"Characterization of Small Phase Defect on EUV Mask Using Micro Coherent EUV Scatterometry Microscope"**
Tetsuo Harada, Yusuke Tanaka, Takahiro Fujino, Takeo Watanabe, Hiroo Kinoshita, Youich Usui, Tsuyoshi Amano
THE 58th INTERNATIONAL CONFERENCE on ELECTRON, ION, and PHOTON BEAM TECHNOLOGY & NANOFABRICATION (EIPBN2014), Washington DC. USA, 2014/5/30."
35. **"Study of Acid Diffusion Behaves Form PAG by Using Top Coat Method for EUVL"**
Jun Sekiguchi, Takeo Watanabe, and Hiroo Kinoshita
The 31st International Conference of Photopolymer Science and Technology Chiba, Japan, 2014/7/8-11.
36. **"EUV Resist Chemical Reaction Analysis by Soft X-ray Absorption Spectroscopy for High Sensitivity Achievement"**
Kazuya Emura, Takeo Watanabe, Daiju Shiono, Masato Yamaguchi, Hirohito Tanino, TsubasaFukui, Yuichi Haruyama, Yasuji Muramatsu, Katsumi Ohmori, Kazufumi Sato, Tetsuo Harada,and Hiroo Kinoshita
The 31st International Conference of Photopolymer Science and Technology Chiba, Japan,

2014/7/8-11.

37. **“Cellular Automaton-based Nanoelectronic Hardware” (Invited Talk)**
Ferdinand Peper, Takeo Watanabe, Teijiro Isokawa, and Nobuyuki Matsui,
6th IEEE International Nanoelectronics Conference 2014, Conference Hall, Hokkaido University,
Sapporo, Hokkaido, 2014/7/28-31.
38. **“Imaging Result of Small Phase Defects Using Micro Coherent EUV Scatterometry Microscope”**
T. Harada, Y. Tanaka, T. Watanabe, T. Amano and H. Kinoshita
26th Microprocesses and Nanotechnology Conference, Fukuoka, Japan. 2014/11/4-7.
39. **“EUV Mask Observation Result Using Coherent EUV Scatterometry Microscope with High-Harmonic-Generation EUV Source”**
Takahiro Fujino, Yusuke Tanaka, Tetsuo Harada, Yutaka Nagata, Takeo Watanabe, Hiroo Kinoshita
Photomask Japan 2014, Yokohama, Japan, 2014/4/15.
40. **“Development of EUV Reflectometer in NewSUBARU”**
Masaki Kuki, Tetsuo Harada, Takeo Watanabe, Hiroo Kinoshita
Photomask Japan 2014, Yokohama, Japan, 2014/4/15.
41. **“Chemical Reaction Analysis of EUV CA Resist for High Sensitivity and Low LWR by Soft X-ray Absorption Spectroscopy”**
Takeo Watanabe, Kazuya Emura, Masato Yamaguchi, Hirohito Tanino, Tsubasa Fukui, Daiju Shiono,
Yuichi Haruyama, Yasuji Muramatsu, Katsumi Ohmori, Kazufumi Sato, Tetsuo Harada, and Hiroo
Kinoshita
EUV lithography symposium 2014, Washington D.C., USA, 2014/10/27.
42. **“Development of a Large Reflectometer for Large EUV Optical Elements”**
Tetsuo Harada, Hiraku Hashimoto, Harutaka Iguchi, Youhei Takahashi, Takeo Watanabe, and Hiroo
Kinoshita
EUV lithography symposium 2014, Washington D.C., USA, 2014/10/27.
43. **“EUV Mask Observation Result Using Coherent EUV Scatterometry Microscope with High-Harmonic-Generation EUV Source”**
Tetsuo Harada, Takahiro Fujino, Yusuke Tanaka, Yutaka Nagata, Takeo Watanabe, and Hiroo
Kinoshita
EUV lithography symposium 2014, Washington D.C., USA, 2014/10/27.
44. **“Pattern Defect Observation Result Using Coherent EUV Scatterometry Microscope with High-Harmonic-Generation EUV Source”**
T. Fujino, Y. Tanaka, T. Harada, Y. Nagata, T. Watanabe and H. Kinoshita
26th Microprocesses and Nanotechnology Conference, Fukuoka, Japan, 2014/11/4-7.
45. **“Study of Dill's B parameter measurement of EUV resist”**
Atsushi Sekiguchi, Yoko Matsumoto, Tetsuo Harada, Takeo Watanabe, and Hiroo Kinoshita
SPIE advanced lithography 2015, San Jose, USA, 2015/2/24.

46. **“High-Performance Feeder Driven by Surface Acoustic Wave for Micro Powders”**, T. Saiki, Y. Matsui, A. Yamaguchi, M. Takeo, K. Maenaka, and Y. Utsumi,
Proc. of 40th International Conference on Micro and Nano Engineering (MNE2014), P2-12-Tu, p.71,
September 22-26 (2014), Lausanne, Switzerland
47. **“Study on the sensitivity of Surface Enhanced Raman spectroscopy using three-dimensional Silver and Gold Nanostructure”**,
R. Hara, R. Takahashi, T. Fukuoka, A. Yamaguchi, Y. Utsumi, ,
27th International Microprocesses and Nanotechnology Conference (MNC2014), No. 7P-11-51,
November 4-7 (2014), Fukuoka, Japan

(3) Academic Degrees

1. Master of Engineering

Ryo Imai (University of Hyogo)

“Study on surface modification of DLC films by irradiation of soft X-ray”

Kengo Kidena (University of Hyogo)

他元素添加水素化 DLC 膜の原子状酸素照射効果

“Effect of irradiation of atomic oxygen against DLC films containing hetero-atom”

Yusuke Tanaka (University of Hyogo),

“集光型コヒーレントスキャトロメトリ一顕微鏡による位相欠陥観察法の研究”

Kazuya Emura (University of Hyogo),

“EUV レジストの反応解析および干渉露光装置の高度化の研究”

Takeshi Kunisada (University of Hyogo)

“Study of full-protocol chemical unit operation for bio-marker detection using 3D Lab-on-a-CD”

Kazuhisa Kuroda (University of Hyogo)

“Studies of mixing structure for 3D Lab-on-a-CD and higher order nanostructure for surface enhanced Raman scattering”

Ryo Sasaki (University of Hyogo)

“Investigation of Micro wave induced chemical reaction”

Ryohei Hara (University of Hyogo)

“Highly sensitive detection of molecular analyte using nano/micro Lab-on-a-chip”

Yuya Matsui (University of Hyogo)

“High frequency dependence on powder transportation property using SAW “

Tomohisa Yamane (University of Hyogo)

“Development of DCRA using synchrotron radiation fabrication”

Yoshihiro Yamamoto (University of Hyogo)

“Study of magnetization dynamics induced by surface acoustic wave injection”

2. Master of Science,

Takahiro Oyama, (University of Hyogo)

“光硬化性ナノインプリント樹脂におけるフッ素系表面活性剤の表面偏析に関する研究”

Hitomi Wakaba, (University of Hyogo)

“ナノインプリントと自己組織化技術の融合プロセスに関する研究”

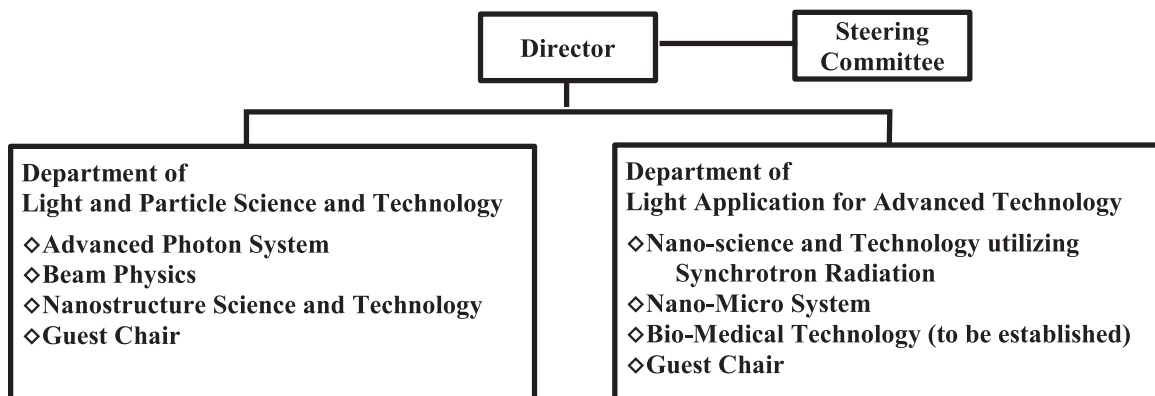
3. Doctor of Engineering,

Tetsunori Murachi (Intel K.K.),

“Applied technology development related to multi-layer structure for EUV Optics - for space satellite mounting and semiconductor device manufacturing “

The Organization of Laboratory of Advanced Science and Technology for Industry University of Hyogo

The organization



Staff (FY 2014)

Research and faculty staff

MIYAMOTO Shuji, Professor, Director
 KINOSHITA Hiroo, Professor
 MATSUI Shinji, Professor
 KANDA Kazuhiro, Professor
 UTSUMI Yuichi, Professor
 NIIBE Masahito, Associate Professor
 SHOJI Yoshihiko, Associate Professor
 WATANABE Takeo, Associate Professor
 HARUYAMA Yuichi, Associate Professor
 YAMAGUTI Akinobu, Associate Professor
 AMANO Sho, Research Associate
 HASHIMOTO Satoshi, Research Associate
 HARADA Tetsuo, Research Associate
 OKADA Makoto, Research Associate

Specially appointed staff

MOCHIZUKI Takayasu, Professor
 KUDOU Hiroto, Associate Professor
 NAGATA Yutaka, Assistant Professor
 IYOSHI Syuzou, Resercher

Guest staff

OHKUMA Haruo, Professor
 ASANO Yoshihiro, Professor

Administrative staff

HAMAGAMI Akiyuki, General Manager
 KOBORI Kazuyuki, Manager
 SONOHARA Kazuhiko, Chief
 KAMIYA Miki, CAST
 KANATANI Naoko, NewSUBARU
 YAMAMOTO Keiko, CAST
 YOKOYAMA Yuka, CAST
 YANO Ayumi, CAST
 FUJIMAKI Hisae, CAST
 YAMADA Miki, CAST
 YAMAMOTO Mako, NewSUBARU
 KUSUMOTO Kumi, CAST
 MORIGUCHI Miyuki, Harima Forum of
 Science and Technology for 21st Century

Liaison staff

ANDO Ainosuke, NewSUBARU
 FUKADA Noboru, NewSUBARU
 UMESAKI Masanori, NewSUBARU
 ISHIKAWA Kazuko, NewSUBARU
 MINAMIYAMA Yasuto, NewSUBARU
 KOTAKA Takuya, NewSUBARU

Contact address

Advanced Research Building

3-1-2 Kouto, Kamigori-cho, Ako-gun, Hyogo, 678-1205 JAPAN.
 T:+81-791-58-0249 F:+81-791-58-0242

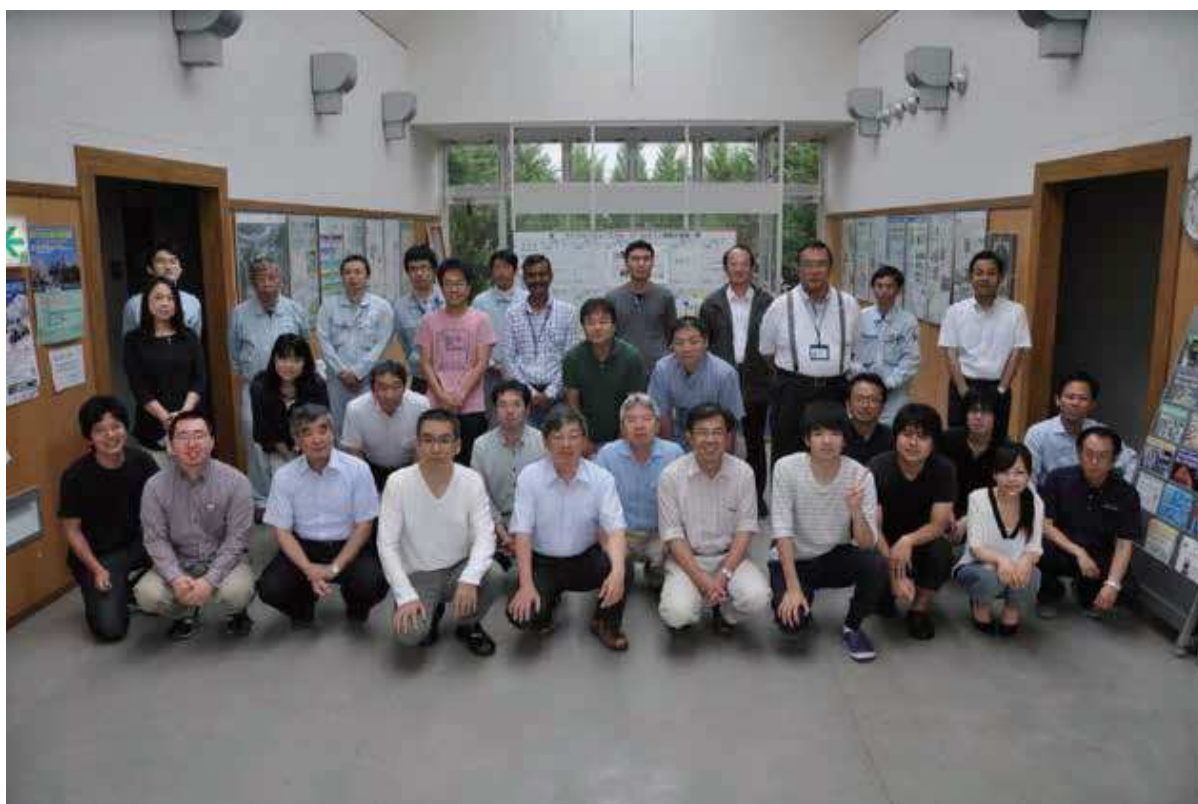
NewSUBARU Synchrotron Radiation Facility

1-1-2 Kouto, Kamigori-cho, Ako-gun, Hyogo, 678-1205 JAPAN.
 T:+81-791-58-2503 F:+81-791-58-2504

Web URL <http://www.lasti.u-hyogo.ac.jp/>, <http://www.lasti.u-hyogo.ac.jp/NS/>

e-Mail lasti@lasti.u-hyogo.ac.jp

Access <http://www.lasti.u-hyogo.ac.jp/NS-en/access/>



NewSUBARU放射光施設 玄関ホールにて



